Georgia State University
ScholarWorks @ Georgia State University

Physics and Astronomy Dissertations | Department of Physics and Astronomy

Winter 12-2011

The Evolution of Dwarf-Irregular Galaxy NGC 1569: A Kinematic Study of the Stars and Gas

Megan C. Johnson
Georgia State University

Follow this and additional works at: https://scholarworks.gsu.edu/phy_astr_diss

 Part of the Astrophysics and Astronomy Commons, and the Physics Commons

Recommended Citation
Johnson, Megan C., "The Evolution of Dwarf-Irregular Galaxy NGC 1569: A Kinematic Study of the Stars and Gas." Dissertation, Georgia State University, 2011.
https://scholarworks.gsu.edu/phy_astr_diss/50

This Dissertation is brought to you for free and open access by the Department of Physics and Astronomy at ScholarWorks @ Georgia State University. It has been accepted for inclusion in Physics and Astronomy Dissertations by an authorized administrator of ScholarWorks @ Georgia State University. For more information, please contact scholarworks@gsu.edu.

THE EVOLUTION OF DWARF IRREGULAR GALAXY NGC 1569: A KINEMATIC STUDY OF THE STARS AND GAS

by

MEGAN C. JOHNSON

Under the Direction of H. Richard Miller and Deidre Hunter

ABSTRACT

The evolution and formation of dwarf galaxies has great importance to our knowledge of cosmological history from the Big Bang through the present day structure we observe in our local universe. Dwarf galaxies are believed to be the "building blocks" of larger galaxies, which implies that interactions and mergers of these small systems must have occurred frequently in the early universe. There is a population of starburst dwarf irregular (dIm) galaxies that seem to have characteristics indicative of interactions or mergers. One of these dIm galaxies is the nearby post-starburst NGC 1569. This dissertation project explores the stellar and gas kinematics of NGC 1569 as well as examines a deep neutral Hydrogen (HI) map made using the Robert C. Byrd Green Bank Telescope (GBT). From these observations, this dissertation analyzes the evolution of NGC 1569 by understanding the three-dimensional shape of this dIm system for the first time. The structure of dIm galaxies is an important

fundamental, physical property necessary to understand the evolution and formation of these common systems. However, the intrinsic shape of dIm galaxies remains controversial. Projected minor-to-major axis ratios provide insufficient data to determine the shapes of dIm galaxies. Fortunately, there is another method by which accurate structures can be measured. The stellar velocity dispersion, coupled with the maximum rotational velocity derived from HI observations, gives a measure of how kinematically hot a system is, and, therefore, indicates its structure. In this dissertation, we present the stellar kinematics, including the stellar velocity dispersion, of NGC 1569 obtained using the Kitt Peak National Observatory (KPNO) Mayall 4-m+Echelle spectrograph. These data are combined with an in depth analysis of high resolution HI data and a discussion of the nature of this starburst dwarf system. The dissertation concludes with a deep HI map of NGC 1569 and three of its nearest neighbors in the IC 342 galaxy group. Extended HI structures are observed in this map and are likely associated with NGC 1569. However, distinguishing if these structures are from an interaction or a merger is not possible and hydrodynamic simulations are needed. These simulations are for future work.

INDEX WORDS: NGC 1569, Dwarf irregular galaxies, Starburst dwarf galaxies

THE EVOLUTION OF DWARF IRREGULAR GALAXY NGC 1569: A KINEMATIC STUDY OF THE STARS AND GAS

by

MEGAN C. JOHNSON

A Dissertation Submitted in Partial Fulfillment of Requirements for the Degree of

Doctor of Philosophy

in the College of Arts and Sciences

Georgia State University

2011

Copyright by
Megan C. Johnson
2011

THE EVOLUTION OF DWARF IRREGULAR GALAXY NGC 1569: A KINEMATIC STUDY OF THE STARS AND GAS

by

MEGAN C. JOHNSON

Committee Co-Chairs:	H. Richard Miller
	Deidre Hunter
Committee:	Douglas R. Gies
	D. Michael Crenshaw
	Steven T. Manson

Electronic Version Approved:

Office of Graduate Studies

College of Arts & Sciences

Georgia State University

December 2011

DEDICATION

This dissertation is dedicated to my husband, Craig, and my daughter, Kaya, as well as my dear family and friends, who have given me the support and love I've needed to complete this work. I also dedicate this dissertation to my wonderful advisor and mentor, Deidre Hunter. Deidre's endless patience, guidance, and support gave me the confidence to succeed in the competitive world of professional astronomy. I am forever grateful for Deidre.

ACKNOWLEDGMENTS

I would like to extend my sincere gratitude to Se-Heon Oh for his expertise, countless discussions, patience, and attention to detail that helped perfect the gas analysis used throughout this dissertation. Se-Heon's double Gaussian decomposition method used to separate bulk motion from non-circular motion gas was necessary to determine the rotation curve of NGC 1569.

Hong-Xin Zhang was instrumental in determining the stellar mass model and I am eternally indebted to him for all of his help, time, and careful consideration. Also, I would like to thank Erik Tollerud for his participation in the ΛCDM simulation model results that show the expected dark matter halo velocities and mass for NGC 1569.

I would like to thank the Lowell Observatory Pre-doctoral Fellowship for all of the opportunities the program has provided me during the three and a half years I was part of the Lowell family. I have grown into an independent professional astronomer because of Lowell Observatory and Deidre Hunter. I am forever grateful for my time at Lowell, which introduced me to my mentor and friend, Deidre. Deidre has given me the courage and skills necessary to be a successful astronomer. I am most thankful for Deidre!

I appreciate all the wonderful help, care and dedication that Daryl Willmarth and the KPNO staff exhibited during all of our observing runs.

I would like to thank all of the wonderful staff, telescope operators, and astronomers at the Green Bank NRAO site for all of their help and support during the preparation of and obtaining of our observations.

This project was funded by the National Science Foundation under the LITTLE THINGS grant number AST-0707563 to DAH. This research has made use of the NASA/IPAC Extragalactic Database (NED) which is operated by the Jet Propulsion Laboratory, California Institute of Technology, under contract with the National Aeronautics and Space Administration.

TABLE OF CONTENTS

LIST OF TABLES

LIST OF FIGURES

LIST OF ABBREVIATIONS

AIPS	The Astronomical Image Processing System
CCD	Charged Coupled Device
CCM	cross-correlation method
DEC	Declination
FWHM	full-width at half-maximum
GALEX	The GALaxy Evolution eXplorer
GBT	Robert C. Byrd Green Bank Telescope
HI	neutral hydrogen
HST	*Hubble Space Telescope*
IDL	Interactive Data Language
IR	infrared
IRAF	Image Reduction and Analysis Facility
kpc	kiloparsecs
KPNO	Kitt Peak National Observatory
LITTLE THINGS	Local Irregulars That Trace Luminosity Extremes The HI Nearby Galaxy Survey
$M_{\rm dm}$	dark matter mass
$M_{\rm dyn}$	dynamical mass
$M_{\odot}$	solar masses
$M_{\rm tot}$	total mass

$M_{\rm vir}$	virial masses
MW	Milky Way
NGC	New Galaxy Catalog
NRAO	National Radio Astronomy Observatory
PA	position angle
RA	Right Ascension
SED	spectral energy distribution
SSC	supermassive star cluster
Th-Ar	thorium-argon
THINGS	The HI Nearby Galaxy Survey
UV	ultraviolet
VLA	Very Large Array
$V_{\rm gas}$	gas velocity
$V_{\rm helio}$	heliocentric radial velocity
$V_{\rm exp}$	expansion velocity
$V_{\rm max}$	maximum rotational velocity
$V_{\rm sys}$	systemic velocity
$V_{\rm star}$	stellar velocity
$\sigma_{\rm obs}$	observed velocity dispersion
$\sigma_{\rm z}$	velocity dispersion perpendicular to the disk

– 1 –
Introduction

1.1 Background

Dwarf galaxies are the most common large-scale objects in the cosmos. They are an essential component necessary for understanding the structure and evolution of the universe. Historically, dwarf galaxies have been thought to be the "building blocks" of larger galaxies. However, there is recent evidence that dwarf galaxies observed today have actually formed later, after the most massive galaxies collected their baryons (Tossi 2003; Guo & White 2009; Paudel et al. 2010b).

A more cohesive picture of dwarf galaxy formation and evolution is becoming clearer. There is strong evidence that all morphological classes of dwarfs can be related on a continuous evolutionary track, particularly due to results from studies of dwarf galaxy locations and environments (Grützbauch et al. 2010; Barazza et al. 2009; Sánchez-Janssen, Aguerri, & Muñoz-Tuñón 2008). Dwarf irregular (dIm) galaxies tend to be found in the field (Hunter & Elmegreen 2006; Dunn 2007); dwarf elliptical (dE) galaxies are generally found in galaxy clusters or groups (de Rijcke et al. 2005); dwarf spheroidal (dSph) galaxies are found closest to massive hosts such as the Milky Way (MW) (Dunn 2010) and are the lowest mass, lowest surface brightness objects detected with virtually no neutral hydrogen content (Burkert 1997).

The spatial distribution of these dwarf galaxies paints an evolutionary picture in which dIm galaxies can become either dE or dSph galaxies through processes that alter their morphology and gas content (e.g., van Zee, Skillman, & Haynes 2004; Dellenbusch et al. 2008). If this theory is correct, then most dwarf galaxies were

at one time dIm galaxies. Dwarf-dwarf galaxy mergers, tidal interactions and ram pressure stripping are the key forces that can transform dIm to dE or dSph galaxies (de Lapparent et al. 2004; Lisker et al. 2009; Paudel et al. 2010a) and can finally result in cannibalism or a minor merger with a large, massive host like the MW. There is now evidence that globular clusters in the MW have come from dwarf galaxies that the MW has cannibalized or is in the process of cannibalizing (Forbes and Bridges 2010).

Of course, there are objects that are not consistent with this suggested evolutionary path such as isolated dE and dSph galaxies (example, Cetus [Sarajedini et al. 2002]). Sawala et al. (2010) performed numerical cosmological simulations focusing on isolated dwarf galaxies. The study found that stellar feedback in low mass systems such as Cetus was enough to remove all remaining gas and cease star formation, thus, making the formation of isolated dSph galaxies plausible. Isolated dE galaxies are more difficult to explain, such as IC 225 (Gu et al. 2006). Some authors such as Conselice, Gallagher, & Wyse (2001) argue that transformation from dIm to dE galaxies is not likely because of the over-brightness and compactness of dE galaxies compared to dIm systems. Instead, these isolated objects may have been ejected from tidal interactions within a galaxy group or cluster, or they may have formed in isolation (Sawala et al. 2010).

Can the kinematics of a dwarf galaxy provide information about its evolutionary history? Many studies of the stellar kinematics of dSph galaxies have shown small stellar velocity dispersions that range from 5-10 km s^{-1} (Walker et al. 2007; Kalirai et al. 2010). Other studies of the stellar kinematics of dE systems have shown internal

stellar velocity dispersions that range from ∼16-87 km s^{-1} (Geha et al. 2010; Chilingarian et al. 2007; de Rijcke et al. 2005). One expects dIm galaxies to have lower stellar velocity dispersions compared to dE galaxies if dIm galaxies are mainly field objects regulated by internal processes and dEs are the products of an external disturbance. If dIm systems are perturbed by infall to a group or cluster and transform to dE galaxies, then tidal effects, mergers and ram pressure stripping can kinematically heat up stellar and gas disks while also removing most of the gas. Tidal effects can also cause a rotating disk to lose angular momentum, thus slowing the overall rotation of a disk. The combination of angular momentum loss and kinematic heating is a recipe that can increase the stellar velocity dispersion and convert a dIm system to a dE system.

1.2 NGC 1569

NGC 1569 is a well-studied nearby post-starburst dwarf galaxy. It has three supermassive star clusters (SSCs) that are believed to have formed from the most recent episode of intense star formation that ended about 20 million years ago. Table 1.2 gives some of the global parameters of NGC 1569. One of the important properties to note is the distance of 3.36 ± 0.2 Mpc (Grocholski et al. 2008). This distance places NGC 1569 comfortably within the IC 342 galaxy group, which has an average distance of 3.35 ± 0.09 Mpc (Karachentsev 2005). Having a group association allows NGC 1569 the possibility of interacting or merging with other galaxies in the IC 342 galaxy group, thus giving this system the ability to transform from a dIm to a dE galaxy. NGC 1569 is, in fact, a complex system with complex kinematics, and there is

Table 1.1. Global Parameters for NGC 1569

Parameter	Value	Ref[a]
Other Names	UGC 03056, ARP 210, VII Zw 016	1
D (Mpc)	3.36 ± 0.20	2
$M_{\rm V}$	-18.2	3
μ_{25} (mag arcsec^{-2})	22.3	5
Galaxy diameter to 25 mag arcsec^{-2} in B, D_{25} (arcmin)	3.6	3
V-band disk scale length, R_D (arcmin)	0.39 ± 0.02	3
Center (RA, DEC) (J2000)	(04:30:49.8, +64:50:51)	3
Minor-to-major axis ratio, b/a	0.55	3
$L_{H\alpha}$ (ergs s^{-1})	5.67 x 10^{40}	4
Star Formation Rate Density (SFR_D) ($M_\odot yr^{-1}kpc^{-2}$)	1.3	4
$V_{\rm sys,stars}$ (km s^{-1})	-82 ± 7	*
$\sigma_{\rm z,stars}$ (km s^{-1})	21 ± 4	*
Stellar Major Axis PA (degrees)	121	*
Inclination from stellar de-projection, i_{opt} (degrees)	60	*
$V_{\rm sys,HI}$ (km s^{-1})	-85	*
$V_{\rm rot}$ (km s^{-1}), from HI not corrected for asymmetric drift	33 ± 10	*
$V_{\rm max}$ (km s^{-1}), from HI corrected for asymmetric drift	50 ± 10	*
$\sigma_{\rm HI}$ (km s^{-1})	23	*
HI Major Axis PA (degrees)	122.5	*
Inclination from HI kinematics, i_{HI} (degrees)	69	*
Kinematic Center, (X_{pos}, Y_{pos}), (RA,DEC)	(04:30:46.125,+64:51:10.25)	*

[a] *Indicates this work.

References. — (1) NASA Extragalactic Database; (2) Grocholski et al. 2008; (3) Hunter & Elmegreen 2006; (4) Hunter & Elmegreen 2004; (5) de Vaucouleurs et al. 1991

evidence that will be presented in this dissertation of an interaction or a past merger that has created the dIm galaxy observed today.

Could NGC 1569 be in transition from a dIm to a dE galaxy? Dellenbusch et al. (2008) identify five galaxies as "transition" objects between the dI (dwarf irregular) and the dE morphological classes. In their study, they list six characteristics that are common among all galaxies in their sample:

1) Star formation rates between 0.1 and 1 $M_{\odot}$ yr^{-1}. $\Longrightarrow$ Using the star formation rate density and the disk scale length in Table 1.2, NGC 1569 has an average star formation rate of 0.6 $M_{\odot}$ yr^{-1}, which is in agreement with values derived by Angeretti et al. (2005).

2) Star formation is centrally concentrated and the outer regions are comprised of older stars. $\Longrightarrow$ According to Aloisi et al. (2001), NGC 1569 has young stars in the center, intermediate age stars evenly distributed throughout the galaxy and older stars in the outskirts of the disk.

3) Lower amounts of HI gas compared to dIs and BCDs (blue compact dwarfs) and slightly higher HI gas content as compared to dE systems. Typical dIs and BCDs have a $M_{\rm HI}/L_{\rm B} > 0.2\ M_{\odot}/L_{\odot}$, dE galaxies have $M_{\rm HI}/L_{\rm B} < 0.1\ M_{\odot}/L_{\odot}$, and transition dwarfs have a $M_{\rm HI}/L_{\rm B} \leq 0.1\ M_{\odot}/L_{\odot}$. $\Longrightarrow$ By converting the $M_{\rm V}$ from Table 1.2 into $M_{\rm B}$ using the (B - V) color from Hunter & Elmegreen (2006) and then converting $M_{\rm B}$ into $L_{\rm B}$. Using an $M_{\rm HI}$ = 2.6 x 10^8 $M_{\odot}$, as determined from this work, NGC 1569 has an $M_{\rm HI}/L_{\rm B} \approx 0.12\ M_{\odot}/L_{\odot}$.

4) High oxygen abundance ratios, with 12 + log(O/H) > 8.4. $\Longrightarrow$ According to Larsen et al. (2008), NGC 1569 has an oxygen abundance ratio 12 + log(O/H) = 8.54.

5) Outer optical colors are similar to typical BCDs with $(\text{B-R})_0 \approx 1$, but bluer than

dEs, which have a $(B\text{-}R)_0 \approx 1.3 - 1.4$. $\Longrightarrow$ NGC 1569 has a $(B\text{-}R)_0 \approx 1$.

6) Smooth outer isophotes that resemble early- rather than late-type galaxies. $\Longrightarrow$ NGC 1569 shows an equal concentration of light in the outer regions in the V-band image of Figure 2.1 in Chapter 2, thus, contains smooth outer isophotes.

As the above list shows, NGC 1569 fits all of these criteria. Furthermore, recent studies of dE galaxies have shown underlying disk-like structures (Paudel et al. 2010b; Lisker et al. 2009). Lisker et al. (2009) suggest that dE galaxies in the Virgo cluster that possess disk-like structures provide evidence that early type dwarf galaxies were once late type dwarfs. NGC 1569 has a disk structure, as shown here in this work, but perhaps thicker than those of typical dIm galaxies.

1.3 Goals and Motivation

The stellar and gas kinematics of NGC 1569 are explored in this dissertation, with the goal of shedding light on its evolutionary history and the reason for its recent starburst. The stellar kinematics are derived from long-slit, integrated light, spectroscopy and the high-resolution HI kinematics are derived from HI data that were part of The HI Nearby Galaxy Survey (THINGS; Walter et al. 2008). Additionally, a new method of imaging the high-resolution HI data cube is discussed and a double Gaussian decomposition of the HI line profiles, a method developed by Oh et al. (2008), is applied in order to separate bulk motions from random motions. Also, this dissertation surveys the extended HI gas content around NGC 1569. Large-scale structures can result from either an interaction or a recent merger.

One main objective for this kinematic research is to identify the shape of NGC 1569 in order to determine if it is a disk or a triaxial system. The kinematic measure, $V_{\rm max}/\sigma_{\rm z}$, is used where $V_{\rm max}$ is the maximum rotation of the galaxy and $\sigma_{\rm z}$ is the velocity dispersion of the stars perpendicular to the disk. This kinematic measure can tell us if NGC 1569 is rotationally supported, i.e., a disk. For example, elliptical and dEs have $V_{\rm max}/\sigma_{\rm z} < 1$ (Figure 4-6 in Binney & Tremaine 1987; Pedraz et al. 2002) while spirals have $V_{\rm max}/\sigma_{\rm z} > 1$, usually 2 - 5 (Bottema 1993; Vega Beltrán et al. 2001).

NGC 1569 is a well studied object because of its post-starburst nature and it contains three of the nearest SSCs, which are young analogs for the globular clusters observed in the MW (Hunter et al. 2000). By understanding the stellar and gas kinematics of this system and the evolutionary history, it is possible to understand how galaxies may have formed in the early universe when starbursts, interactions, and mergers were more common. This dissertation can give insight into the star formation mechanisms and provide evidence for the "building block" scenario that may have been present in the early universe by understanding a nearby example of a candidate dwarf-dwarf galaxy merger remnant, NGC 1569.

This work is part of a large collaborative effort called Local Irregulars That Trace Luminosity Extremes, The HI Nearby Galaxy Survey (LITTLE THINGS; Hunter et al., in preparation). One of the goals of the LITTLE THINGS survey is to understand how dIm galaxies form stars. LITTLE THINGS is a multi-wavelength study of 41 dIm and Blue Compact Dwarf (BCD) galaxies. LITTLE THINGS was granted close

to 376 hours in 2007 and 2008 on the Very Large Array (VLA[1]) in the B-, C-, and D-array configurations in order to obtain deep HI maps for 21 galaxies. The other 20 galaxies are from the VLA archives. In addition to the HI data, LITTLE THINGS has extensive, Hα and optical photometry for each dIm galaxy from previous studies (Hunter & Elmegreen 2004; Hunter & Elmegreen 2006) and has also collected GALEX ultraviolet for most and near- and mid-infrared data (ground based JHK and *Spitzer*) for a subsample.

1.4 Dissertation Outline

This dissertation is outlined as follows: Chapter 2 describes the optical spectroscopy used to determine the stellar and ionized gas kinematics of NGC 1569. Chapter 3 discusses the high-resolution HI data used to determine the gas kinematics and Chapter 4 outlines the mass modeling for the stars and gas. Chapter 5 explores the implications for NGC 1569 being a transition dwarf while Chapter 6 describes results from deep HI imaging around a large region of NGC 1569. Finally, Chapter 7 summarizes the observations and explores the future work for understanding dwarf starburst galaxies.

[1]The VLA is a facility of the National Radio Astronomy Observatory (NRAO). NRAO is a facility of the National Science Foundation operated under cooperative agreement by Associated Universities, Inc.

– 2 –

Optical Spectroscopy

2.1 Stellar Spectra

2.1.1 Observations

NGC 1569 was observed with the KPNO 4-meter telescope + Echelle spectrograph for three nights in 2008 February and five nights in 2008 November. Table 2.1 lists the observations and shows the total number of exposures, along with total integration time in seconds, used to make each galaxy and sky spectrum. Long-term status was granted on the 4-m for observations of the sample, and this made acquisition of all optical spectroscopic data for NGC 1569 possible. The crucial first step was to identify the center of the galaxy and position angle (PA) of the major axis in order to be able to place the slit. This was done by analyzing intensity contours of the V-band image. Four PAs were observed, all centered on the morphological center of the galaxy: the major axis (PA = 121°), the minor axis (PA = 31°) and ±45° from the major axis. Figure 2.1 shows the V-band image with each slit position placed over the image in black. During the 2008 February observing run, the major and minor axes of NGC 1569 were observed and during the 2008 November observing run, the intermediate angles (±45° from the major axis) as well as the ionized gas, O[III]λ5007 Å, at two PAs were also observed.

Table 2.1. Optical spectroscopic observations of NGC 1569 taken with the KPNO 4-m + Echelle spectrograph in 2008.

UT Date Obs.	PA[a]	N_{gal}[b]	t_{gal}(s)[c]	N_{sky}[d]	t_{sky}(s)[e]	N_{spec}[f]	N_{RV}[g]
Mg Ib spectral region							
02/01/2008	Major axis - 121°	5	9000	5	9000	7	4
02/02/2008	Major axis - 121°	5	9000	5	7393	9	5 + 1
02/03/2008	Minor axis - 31°	4	7200	4	5673	4	11 + 1
11/19/2008	+ 45° from major axis - 166°	8	13,800	7	12,000	4	5
11/20/2008	− 45° from major axis - 76°	3	5400	2	3600	2	6 + 1
11/21/2008	− 45° from major axis - 76°	8	14,400	8	13,860	6	9
11/22/2008	− 45° from major axis - 76°	5	9000	5	8841	3	10
	Major axis - 121°	3	5400	3	5400	4	10
O[III]λ5007 Å observations							
11/23/2008	Major axis - 121°	3	4800	3	1800	95	NA
11/23/2008	Minor axis - 31°	3	1800	1	600		NA

[a]PA observed;

[b]Number of galaxy exposures co-added into a single spectrum;

[c]Total integration time, in seconds, on galaxy;

[d]Number of sky exposures co-added into a single spectrum;

[e]Total integration time, in seconds, on sky;

[f]Number of one-dimensional spectra extracted;

[g]Number of radial velocity standard stars used in cross-correlation function. The "+ 1" is in reference to the solar spectrum, from twilight flats, used as a radial velocity standard star.

The "fast UV" camera was used along with pre-slit filter GG 495. The Echelle was converted into a two-dimensional, long-slit spectrograph by replacing the cross-disperser with a mirror flat. This permitted the isolation of a single order and produced a $3'$ long slit. In order to maximize throughput, while maintaining high spectral resolution, the slit was opened to a width of $2''.5$. For the stellar kinematic data, the Mg Ib stellar absorption features were targeted at wavelengths 5183.6 Å, 5172.7 Å, and 5167.3 Å, and thus, the post-slit filter KP 1433 was used to isolate order 10 for the 316-63° Echelle. This filter has a central wavelength of 5204 Å and a full-width half-maximum (FWHM) of 276 Å. The free spectral range of the Echelle was 517 Å centered at 5170 Å, but, for the Tektronics 2048 x 2048 CCD that was used, only 286 Å fit across the chip. The prominent Mg Ib stellar absorption features are easily detected and provide an obvious region for accurate cross-correlation analysis with respect to MW radial velocity standard stars.

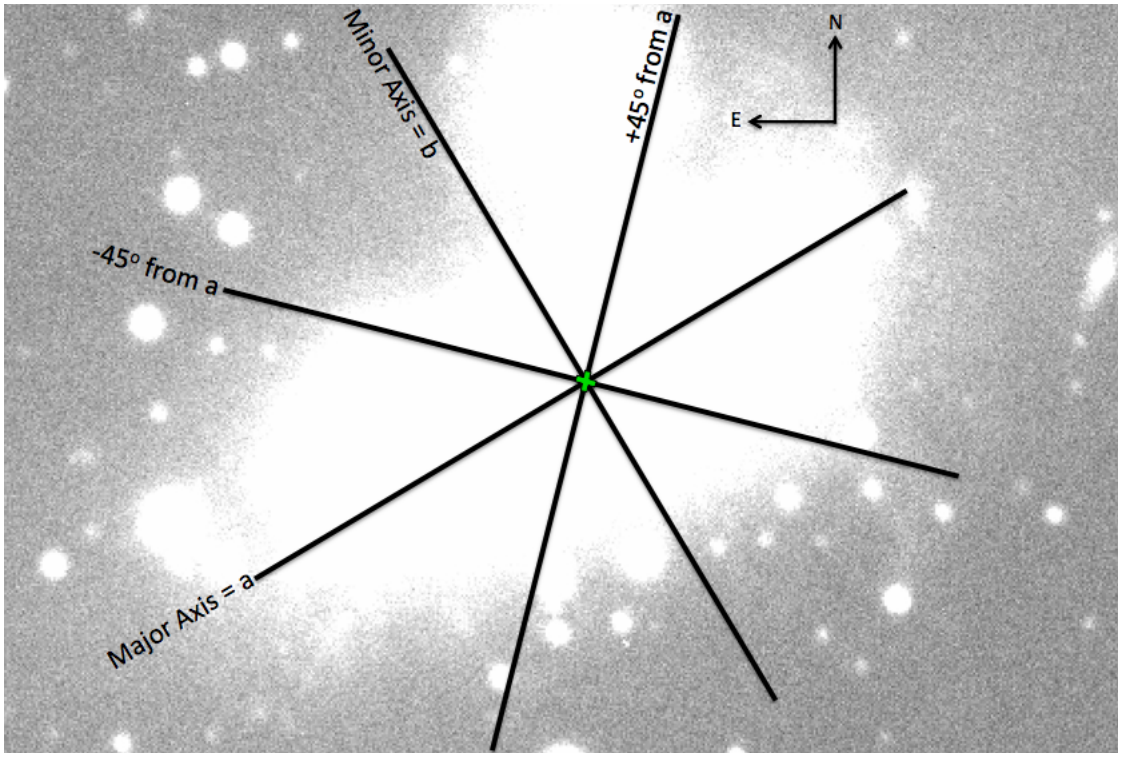

Figure 2.1 V-band image of NGC 1569 showing the four PAs of the 3′ long slit of the Echelle spectrograph. The black lines represent, approximately, the position, length and width of the 3′ long slit. The green 'X' in the center marks the morphological center where the center of the slit was placed; North is up and East to the left. There is a bright MW star to the north of the galaxy.

For this spectral range, the setup provided a FWHM = 0.38 Å as measured from the central lines of Th-Ar comparison lamp exposures, giving a resolving power of R = 13,500 (at 5130Å) and a velocity resolution of ∼21 km s^{-1}. A spatial pixel scale of about 1.″2 pix^{-1} was achieved, while binning by 2 pixels in the spatial direction, and a final spectral pixel scale of 0.14 Å pix^{-1} was obtained. Finally, at the beginning of each run, Daryl Willmarth, of the KPNO staff, carefully aligned the East-West direction of the slit along the rows of the CCD.

On the first night of each observing run, a single radial velocity standard star was moved in short 30″ steps along the slit. These data were used to determine the spatial pixel scale and to trace the spatial slit distortion. At the beginning of each night, ten dome flats were taken using a white screen inside the dome illuminated by a lamp from the top of the telescope and used these to determine pixel-to-pixel variations in the detector. Also, twilight exposures were taken frequently by observing a uniformly illuminated spot on the sky. The rotator on the Echelle was set to the desired PA before observations began, and generally one PA was used during a night.

After all flats were taken, a series of radial velocity standard stars were observed. These MW stars were selected to have a range of spectral types, F, G, and K-type, and luminosity classes to provide a varied spectral stellar library for the cross-correlation analysis. Table 2.2 lists the standard stars used in the cross-correlation. The same stars were observed from night to night and run to run to minimize and identify systematic offsets. However, the spectral template library contained a wider variety of spectral types and classes during the November run due to the availability of more standard stars.

For NGC 1569, 1800 s exposures were taken, making certain that the center of the slit was positioned accurately by centering on a nearby foreground star before each exposure, zeroing the telescope coordinates, and then off setting to the morphological center of the galaxy. After each galaxy exposure, to ensure proper sky subtraction, a dark region of the sky, close to the galaxy, was observed for 1800 s. Following every object and sky exposure, Th-Ar comparison lamp exposures were taken in order to acquire accurate wavelength calibration as a function of time and position. The galaxy had five to seven exposures taken, which were co-added together for a total integration time of 2.5 – 3.5 hours, for each PA during a single night. Each night ended by observing a second series of radial velocity standard stars.

Table 2.2. Radial velocity standard stars used for cross-correlation.

HD No.	Apparent Magnitude, V	Spectral Type & Class	RA (hh:mm:ss)	DEC (° : ′ : ″)	$V_{\rm helio}$[a] (km s^{-1})	σ_V (km s^{-1})	UT Date Obs.
3765	7.36	K2 V	00:41:17.4	+40:13:56	-63.0	0.2	11/20/2008
8779	6.41	K0 IV	01:26:53.5	-00:21:18	-5.0	0.5	02/03/2008
9138	4.84	K4 III	01:30:37.9	+06:11:15	+35.4	0.5	02/03/2008
							11/22/2008
12029	7.44	K2 III	01:59:11.2	+29:25:16	+38.6	0.5	11/22/2008
22484	4.28	F9 IV-V	03:37:18.5	+00:25:41	+27.9	0.1	02/01/2008
							02/02/2008
							02/03/2008
							11/22/2008
23169	8.50	G2 V	03:44:23.9	+25:45:06	+13.3	0.2	02/03/2008
26162	5.50	K1 III	04:09:39.8	+19:37:52	+23.9	0.6	02/01/2008
32963	7.60	G5 IV	05:08:27.3	+26:20:18	-63.1	0.4	02/02/2008
							11/21/2008
65583	6.97	G8 V	08:01:03.6	+29:11:09	+12.5	0.4	11/19/2008
							11/22/2008
65934	7.70	G8 III	08:02:42.1	+26:36:49	+35.0	0.3	11/22/2008
66141	4.39	K2 IIIb Fe-0.5	08:02:42.5	+02:18:39	+70.9	0.3	11/22/2008
75935	8.46	G8 V	08:54:20.3	+26:52:50	-18.9	0.3	11/21/2008
90861	6.88	K2 III	10:30:22.2	+28:32:15	+36.3	0.4	11/21/2008
92588	6.26	K1 IV	10:41:50.1	-01:47:11	+42.8	0.1	11/19/2008
							11/22/2008
102494	7.48	G9 IVw...	11:48:22.8	+27:17:36	-22.9	0.3	11/22/2008
122693	8.11	F8 V	14:03:15.6	+24:31:14	-6.3	0.2	02/03/2008
126053	6.27	G1 V	14:23:41.4	+01:12:08	-18.5	0.4	02/02/2008
							02/03/2008
132737	7.64	K0 III	15:00:14.4	+27:07:37	-24.1	0.3	02/01/2008
							02/02/2008
							02/03/2008
136202	5.06	F8 III-IV	15:19:44.9	+01:44:01	+53.5	0.2	02/03/2008
144579	6.66	G8 IV	16:05:14.4	+39:08:02	-60.0	0.3	02/01/2008
							02/03/2008
145001	5.00	G5 III	16:08:27.6	+17:01:29	-9.5	0.2	02/02/2008
							02/03/2008
154417	6.01	F8.5 IV-V	17:05:42.8	+00:41:26	-17.4	0.3	02/03/2008
182572	5.16	G7 IV Hδ 1	19:25:22.5	+11:57:47	-100.5	0.4	11/20/2008
							11/21/2008
187691	5.11	F8 V	19:51:26.1	+10:26:15	+0.1	0.3	11/19/2008
							11/21/2008
194071	7.80	G8 III	20:22:58.8	+28:16:26	-9.8	0.1	11/20/2008

Table 2.2 (cont'd)

HD No.	Apparent Magnitude, V	Spectral Type & Class	RA (hh:mm:ss)	DEC (° : ′ : ″)	$V_{\rm helio}$[a] (km s^{-1})	σ_V (km s^{-1})	UT Date Obs.
203638	5.41	K0 III	21:24:38.4	-20:48:55	+21.9	0.1	11/20/2008
							11/21/2008
212493	4.79	K0 III	22:28:17.3	+04:44:19	+54.3	0.3	11/19/2008
							11/21/2008
							11/22/2008
213014	7.45	G9 III	22:28:36.3	+17:18:25	-39.7	0.0	11/19/2008
213947	6.88	K2	22:35:00.6	+26:38:32	+16.7	0.3	11/21/2008
222368	4.13	F7 V	23:40:23.3	+05:40:21	+5.3	0.2	11/20/2008
							11/22/2008
223311	6.07	K4 III	23:48:58.7	-06:20:00	-20.4	0.1	11/20/2008
							11/21/2008

[a]Velocities are heliocentric radial velocities.

2.1.2 Data Reductions

All data reductions were accomplished using the Image Reduction and Analysis Facility (IRAF[1]). To begin reductions, CCDPROC was used to fit the overscan to all images in order to remove the electronic pedestal. Next, pixel-to-pixel variations were corrected by flat-fielding using dome flats taken each night. Special attention was given to trimming the two-dimensional flats so that the steep drop-off of light towards the edges would not complicate the normalization function. All dome flats from a single night were combined, corrected for bad pixels by interpolating across the bad pixel regions, and fit with a curve over the entire wavelength region in order to normalize the spectral response across the chip, leaving just pixel-to-pixel response variations.

The next steps were to correct for all slit distortions, both spatially and spectrally, and to place all images on a constant wavelength scale. The IRAF package LONGSLIT was used with the tasks IDENTIFY, REIDENTIFY, and FITCOORDS

[1]IRAF is distributed by the National Optical Astronomy Observatory, which is operated by the Association of Universities for Research in Astronomy (AURA) under cooperative agreement with the National Science Foundation.

to achieve the distortion corrections. First, the radial velocity standard star that was moved spatially along the slit was used to map out the distortion along rows of constant position, and then, the comparison lamp exposures were used to trace the distortion along columns of constant wavelength. These fitting procedures produced coordinate maps that were then applied to every respective object exposure using TRANSFORM. Figure 2.2 shows before and after distortion corrections as applied to a comparison lamp exposure. Next, a slit function was applied that corrected for the minor illumination drop off at the edges of the slit in the spatial direction. This was achieved by combining the twilight flats from a single night and using ILLUM to fit a two-dimensional function to the illumination pattern along bins of summed columns in the spatial direction.

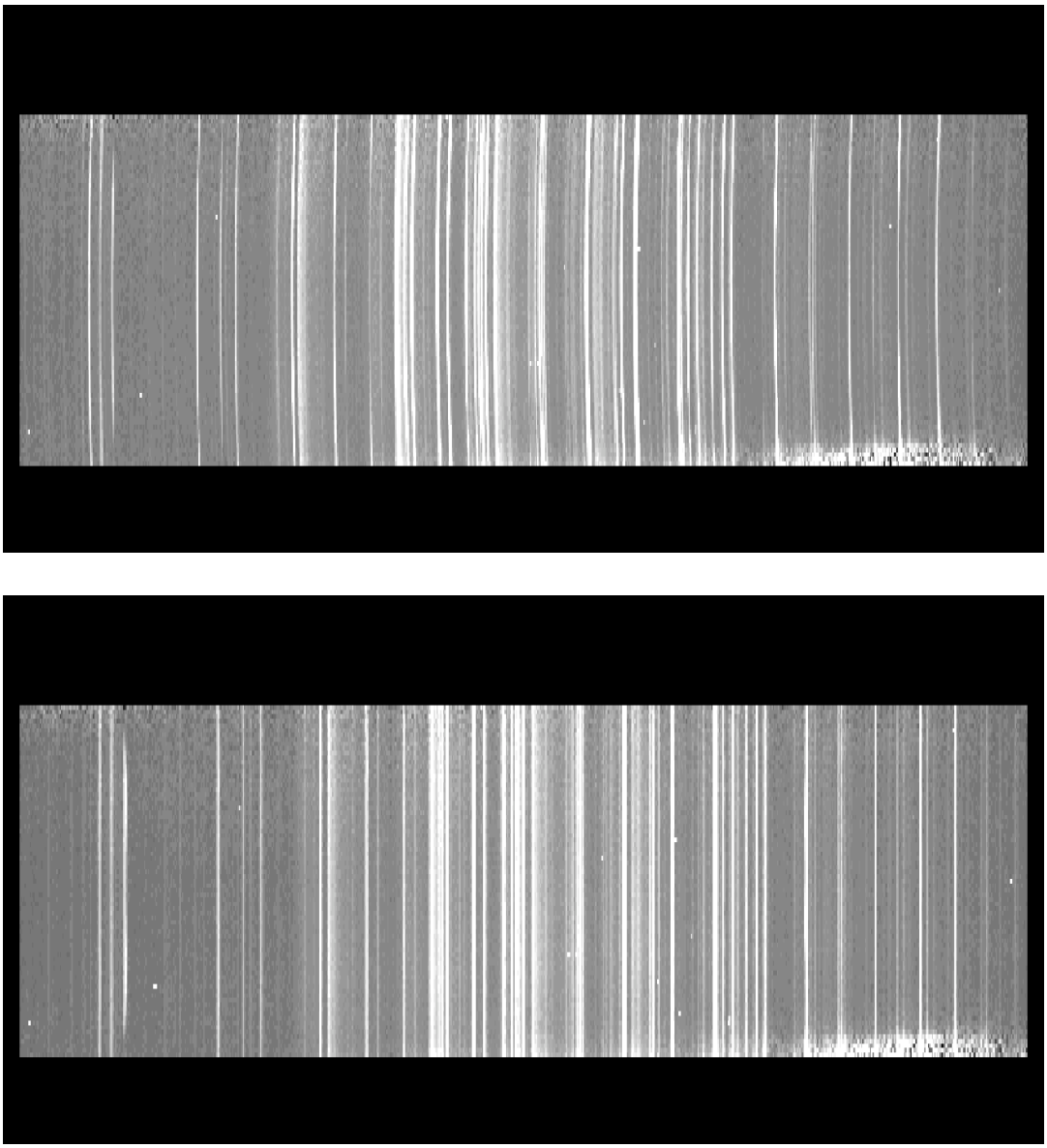

Figure 2.2 Top: Two-dimensional Th-Ar comparison lamp exposure *before* distortion corrections were applied. Bottom: Two-dimensional comparison lamp exposure *after* distortion corrections were applied. For both panels, wavelength is along the horizontal axis and the vertical axis is the spatial direction of the slit.

Before combining the spectra, careful measure was taken to ensure proper galaxy alignment. This was accomplished by over-plotting all galaxy spectra that were to be combined and analyzing the peak flux in individual images. If necessary, a pixel shift was applied to one or more galaxy exposures to align peaks in each image. IMCOMBINE was implemented with cosmic ray rejection and all galaxy images from a single night with the same PA were combined into a single spectrum. The same combining process, without the shifting procedure, was applied to the sky images. Finally, the co-added sky image was subtracted from the co-added galaxy image while taking care to scale the combined sky image, when needed, to correct for differing exposure times. Figure 2.3 shows a co-added galaxy spectrum of the major axis of NGC 1569 before (*top*) and after (*bottom*) sky subtraction.

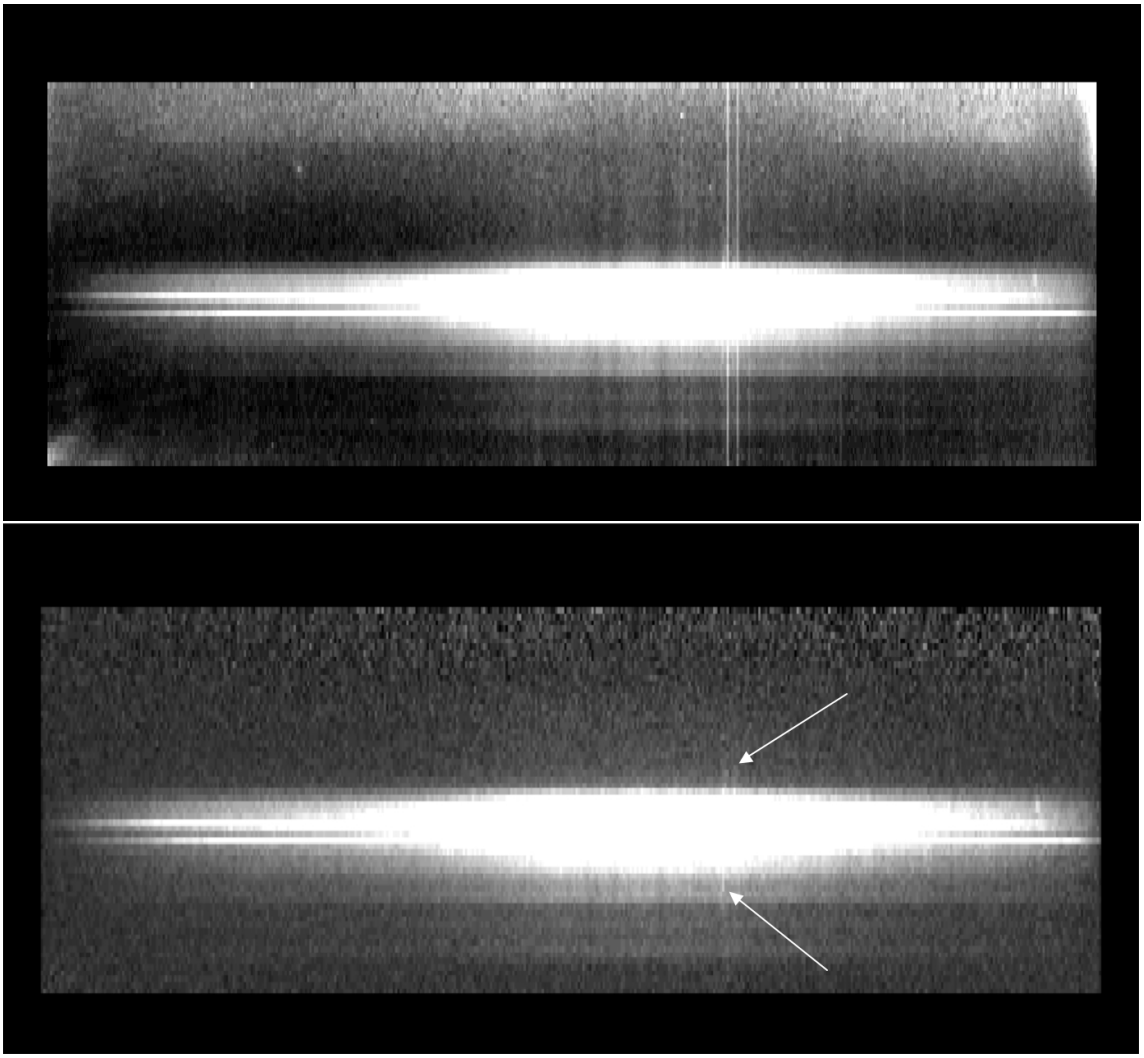

Figure 2.3 Top: Five 1800s spectra co-added to create a two-dimensional galaxy spectrum of the major axis of NGC 1569 *before* sky subtraction. Bottom: Same as top only *after* sky subtraction. For both panels, wavelength is along the horizontal axis ($\sim$238 Å total coverage) and the vertical axis is the spatial direction along the slit ($\sim 3'$) with west pointing up. The bottom panel shows residual sky emission lines, indicated by the white arrows. The bright region in the spatial center, about $1'$, was used in the cross-correlation process.

2.1.3 Analysis of Data

2.1.3.1 Extracting One-Dimensional Spectra

The task SCOPY was used in IRAF to extract one-dimensional stellar spectra from the two-dimensional spectra of NGC 1569. It was necessary to sum over a series of consecutive rows in the spatial direction during spectral extraction in order to increase the signal-to-noise. In the portion of the spectrum that contains the brightest light, from radii 0″ to -25″ (West of center), which is also where the SSCs reside (shown in Figure 2.4), five rows at a time were summed, ∼6″ of the major axis along the slit. For the regions of the galaxy that have a lower light concentration, from radii +17″ to 0″ (East of center), ten rows of the major axis were summed, ∼12″. To avoid diluting the true stellar velocities and velocity dispersions, no more than 12″ were summed, twice the HI resolution, which, at a distance of 3.36 Mpc (Grocholski et al. 2008), corresponds to 195 pc.

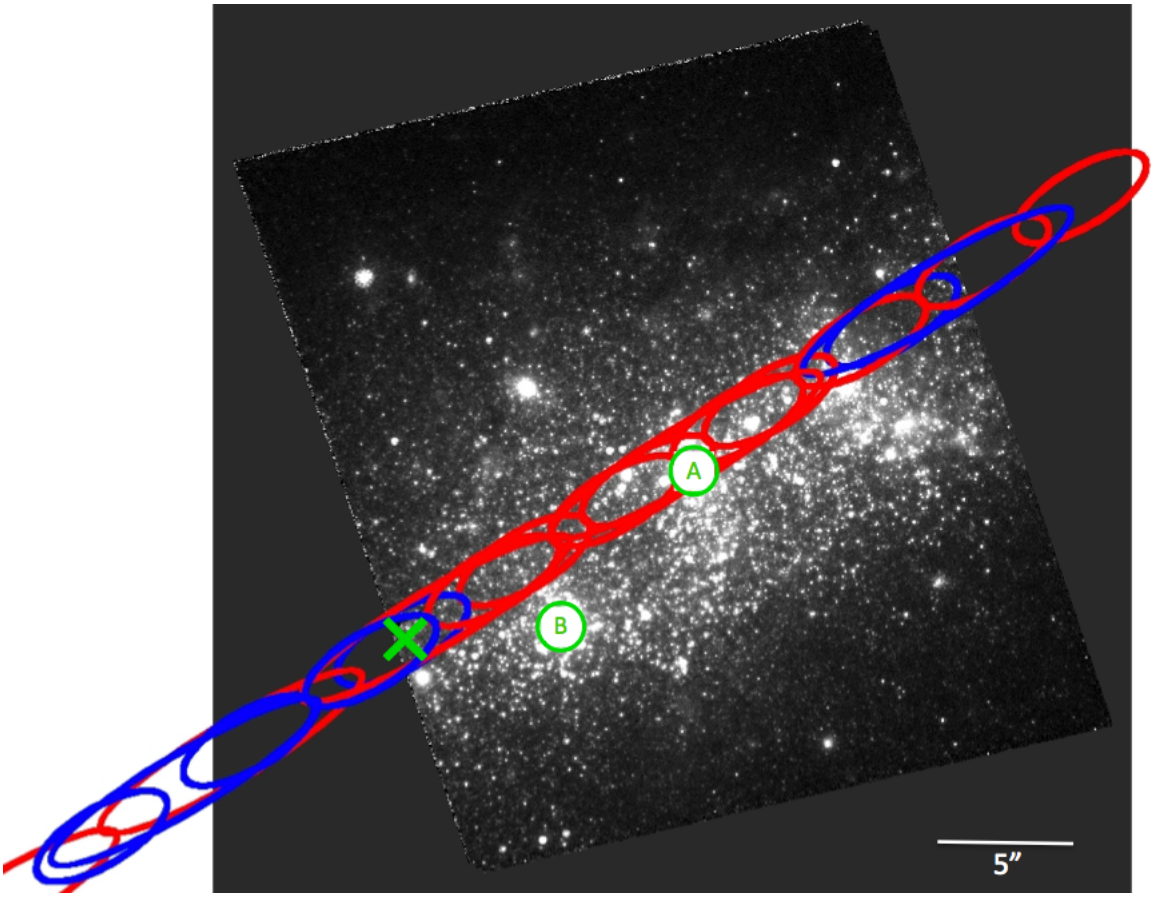

Figure 2.4 An *HST* image of the center of NGC 1569 showing three SSCs (“A” is composed of two SSCs). The ovals represent bins over which the stellar kinematics were determined. Red and blue ovals show red- and blue-shifted velocities, respectively, with respect to the systemic velocity. The green ‘X’ marks the center of the slit and the galaxy.

One-dimensional spectra were also extracted from the radial velocity standard stars using the IRAF task APALL. The center of the peak emission in each star was identified, and the background was fit using the spatial regions of the slit that contain no stellar data. In some cases, the twilight sky exposures were used to extract a solar spectrum, which was used in the cross-correlation method (CCM) as a G2 V radial velocity standard star. Table 2.1 identifies the nights that utilized these solar spectra by the "+1" added to the number of standard star spectra in column 9. Once one-dimensional spectra were extracted, the $V_{\rm helio}$ radial velocities from the United States Nautical Almanac (2008) were added into the header of each star. These spectra are the templates that were used in the CCM. The IRAF task CONTINUUM was used to fit a cubic spline function to the continuum in the spectra of the galaxy and the template stars. At this point, all spectral data were fully reduced, properly extracted, continuum subtracted, and ready for the CCM.

2.1.3.2 Cross-Correlation Method

The FXCOR task in IRAF was used for all CCM computations. The template stars were cross-correlated with each other to test the CCM and to check the accuracy of the stars' velocities. This also gave us the inherent FWHM due to instrumental and data reductions effects.

The one-dimensional spectra from the galaxy were cross-correlated with the stellar templates observed during a single night. The heliocentric radial velocities, corrected for Earth's motion, and velocity dispersions of the bulk of the stars in NGC 1569 were determined, for each spectrum, by fitting a single Gaussian curve to the peak

of the CCM. Excluded from the fit were regions containing residual emission line features due to internal galaxy emission or atmospheric emission lines that were not completely removed during the sky subtraction step. The bottom image of Figure 2.3 shows these residual sky emission lines at around 5196.8 Å and 5199.1 Å indicated by the white arrows in the two-dimensional galaxy spectrum of the major axis. Figure 2.5 demonstrates a one-dimensional galaxy spectrum extracted from the bottom image of Figure 2.3. The residual sky lines were avoided by selecting appropriate wavelength ranges for the CCM. The noisy ends of the spectrum that resulted from the spectral efficiency fall-off at the ends were also excluded. For this particular spectrum, the regions, shown by the horizontal brackets in Figure 2.5, from 5105 - 5196 Å and 5200-5263 Å, were used in the CCM.

Figure 2.6 shows the CCM for one template star, HD 144579, cross-correlated with 7 independent galaxy spectra extracted along the major axis. The plots shown in this figure are the output of FXCOR in IRAF. Given in each plot is the peak of the CCM with the number of points, $V_{\rm helio}$, and FWHM (shown as 'Width' in Figure 2.6) of the given position along the major axis of NGC 1569.

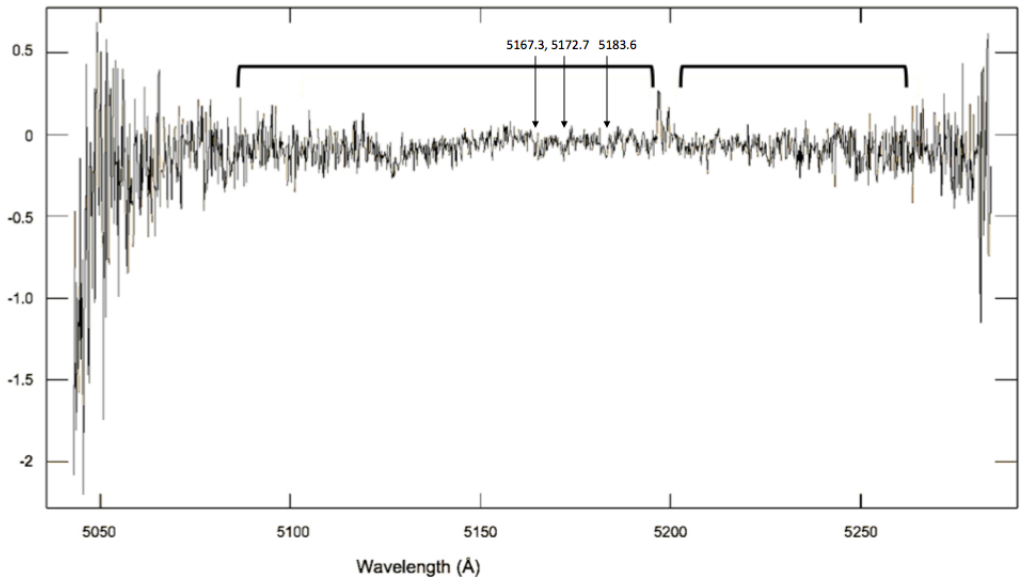

Figure 2.5 Example of a one-dimensional galaxy spectrum, summed over 6.″1, extracted from the two-dimensional spectrum shown in the bottom panel of Figure 2.3. This is along the major axis at a radius of +18″ (East) from the center of NGC 1569. The regions identified by the horizontal brackets were the regions used in the cross-correlation fit. They were chosen to avoid emission lines left from the sky subtraction and the noisy ends of the spectrum. The same regions were used both for the galaxy and for the radial velocity standard stars.

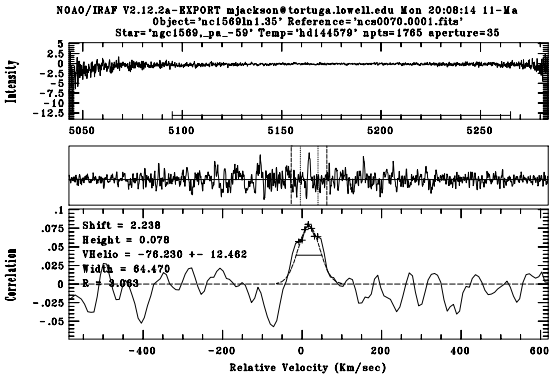

(a) $-20\farcs9$ position, summed over $12\farcs2$

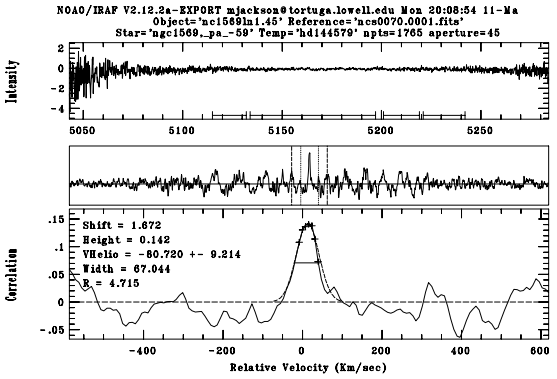

(b) $-8\farcs7$ position, summed over $12\farcs2$

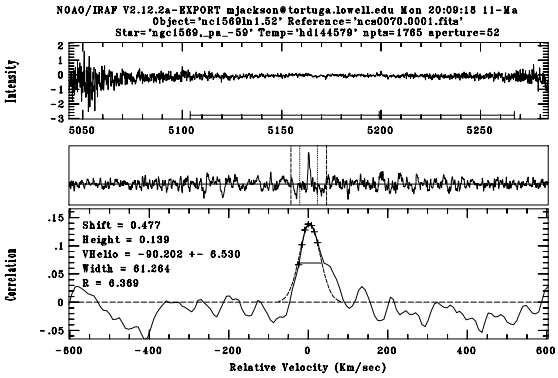

(c) $-0\farcs086$ position, summed over $6\farcs1$

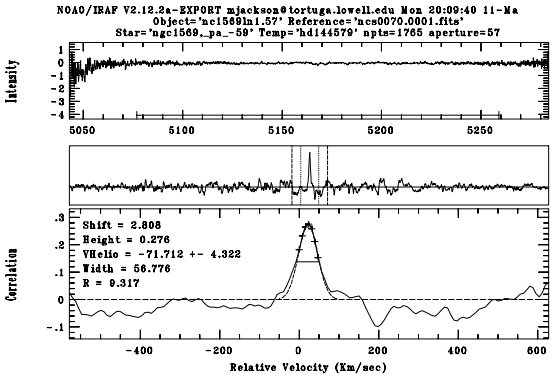

(d) $6\farcs0$ position, summed over $6\farcs1$

Figure 2.6 Cross-correlation function (CCF) peaks for seven spectra extracted along the major axis of NGC 1569 cross-correlated with the radial velocity standard star HD 144579. The spectra shown above the CCM peaks are the full one-dimensional extracted galaxy spectra showing the regions of the spectra used in the CCM marked by the horizontal lines along the wavelength axis. The middle panel shows the CCF, and the bottom panel expands the plot around the CCF peak.

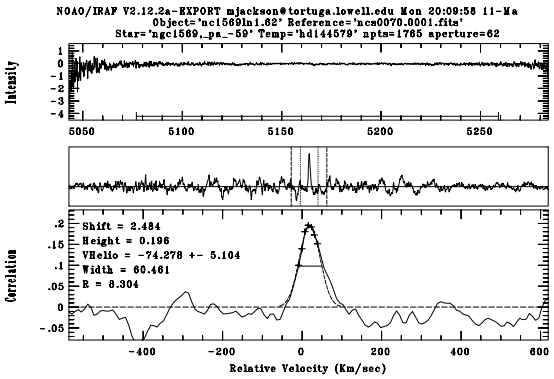

(e) 12.″2 position, summed over 6.″1

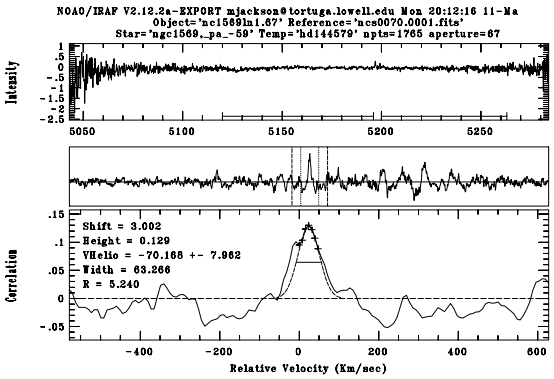

(f) 18.″3 position, summed over 12.″2

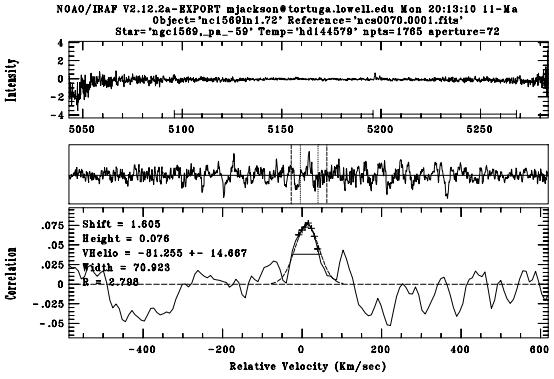

(g) 24.″4 position, summed over 12.″2

Figure 2.6 Continued

2.1.4 Results

Heliocentric radial velocities ($V_{\rm helio}$) of NGC 1569 as a function of radius for all four PAs were successfully acquired. Each template star was cross-correlated with each galaxy position, and the weighted average of the template stars was used to determine the $V_{\rm helio}$ values at each galaxy radius. Figure 2.7 shows position-velocity (P-V) graphs, where the positive positions are in the eastern direction. The error bar in the x-direction on the graph, which is the distance from galaxy center, represents the spatial area of the slit over which the velocities were determined. The weighted average of the minor axis velocity points was used to determine a systemic velocity, $V_{\rm sys}$, of -82.1±6.9 km s^{-1}, which is denoted by the horizontal solid line in Figure 2.7. This value is consistent with those obtained by Reakes (1980), $V_{\rm sys}$ = -77 km s^{-1}, and de Vaucouleurs et al. (1991), $V_{\rm sys}$ = -74 km s^{-1}, but inconsistent with the value obtained by Schneider et al. (1992), $V_{\rm sys}$ = -104 ± 4 km s^{-1}.

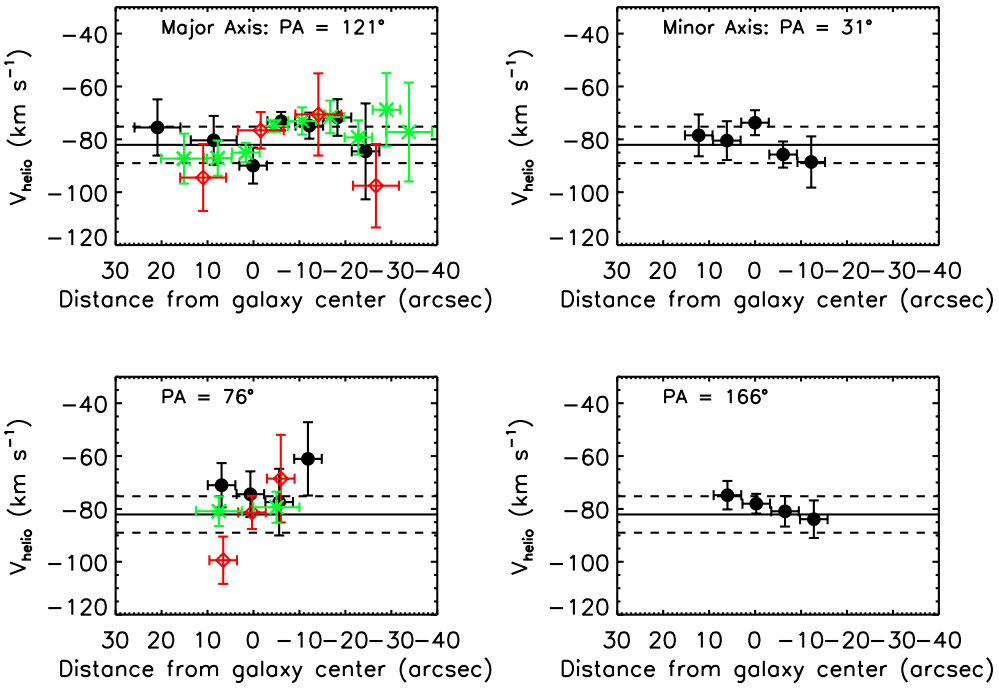

Figure 2.7 Observed heliocentric velocities in the stars along four PAs. Red diamonds, green stars, and black filled circles represent independent points derived from different observing nights. The dashed lines represent the ± 6.9 km s^{-1} uncertainty in $V_{\rm sys}$. East is at positive distances from the galaxy center; West are negative distances. Error bars along the x-axis show the spatial range summed along the slit.

No assumptions can be made about the stellar and HI disks having the same geometry because there are examples of dIm systems in which the stars and gas have very different kinematics. In the case of dIm galaxy WLM, Leaman et al. (2009) compare the kinematics of the stars and HI and discover that the stars and HI are kinematically decoupled and do not possess the same geometry. They conclude that the stars lie in a thicker disk than the HI. Hunter et al. (2002) determined that the stars in NGC 4449 are in a face-on disk, while the HI disk is inclined so that it exhibits rotation as well as a counter-rotation component in the center. Therefore, the stellar kinematics and gas kinematics are carefully examined independently here so that the comparison is more robust.

To begin, the stars alone are investigated. The four PAs are used to constrain the inclination and line of nodes. Figure 2.8 shows the results of a least squares fit to the following formula for the major axis and the two intermediate PAs ($\pm$ 45° from the major axis) where the intermediate PAs are de-projected onto the major axis using the following equation:

$$V_{obs} - V_{sys} = \frac{V(R)\ \sin(i)\ \cos(\eta - \theta)}{[\sec^2(i) - \tan^2(i)\ \cos^2(\eta - \theta)]^{1/2}} \tag{2.1}$$

where, i is the inclination of the disk, η is the PA of the observed point, θ is the PA of the major axis (line of nodes), $V_{\rm obs}$ is the observed line-of-sight radial velocity, $V_{\rm sys}$ is the systemic velocity, and $V(R)$ is the rotational velocity at radius R. The above equation (equation 2.1) came from private communication with Vera Rubin. Although the velocities of the stars do not follow circular motion in all four position angles, the inclination of the disk was still able to be constrained to $i \approx 60°$ and the

major axis PA to ∼120°. Both of these estimates agree well with the HI results of Chapter 3.2.2. Furthermore, Figure 2.9 shows P-V plots of the stars plotted with HI intensity contours. These plots demonstrate the kinematic likeness between the stars and HI, as the stars follow the HI in all four PAs. These plots will be discussed in more detail in Chapter 5.1.1.

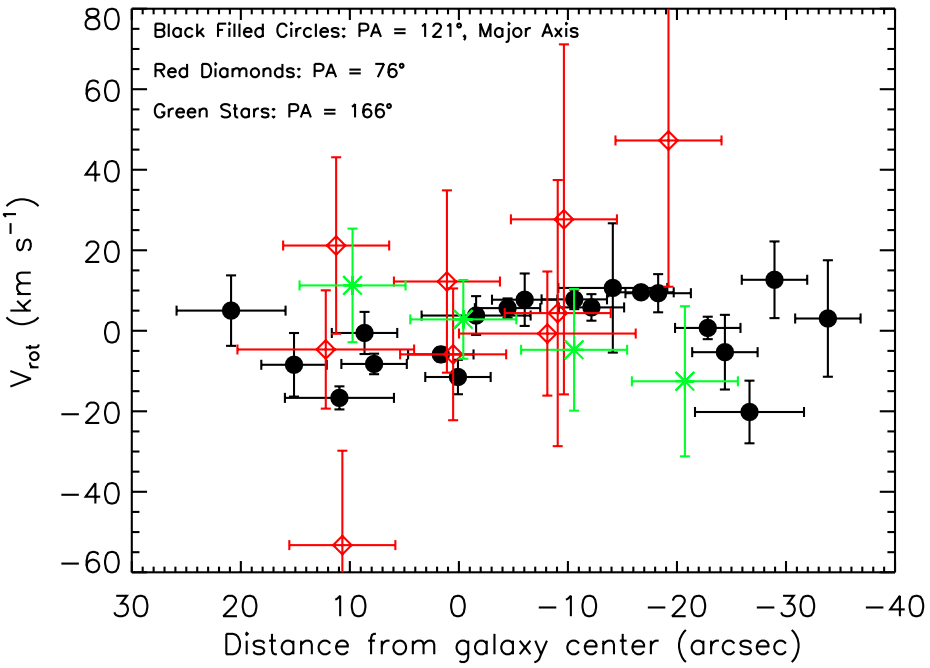

Figure 2.8 De-projected velocities of the stars relative to V_{sys}. Black filled circles are points along the major axis. Red diamonds represent the -45° from the major axis PA, PA = 76°. Green stars represent the +45° from the major axis PA, PA = 166°. East is at positive distances from the galaxy center; West are negative distances. Error bars along the x-axis show the de-projected spatial range summed along the slit.

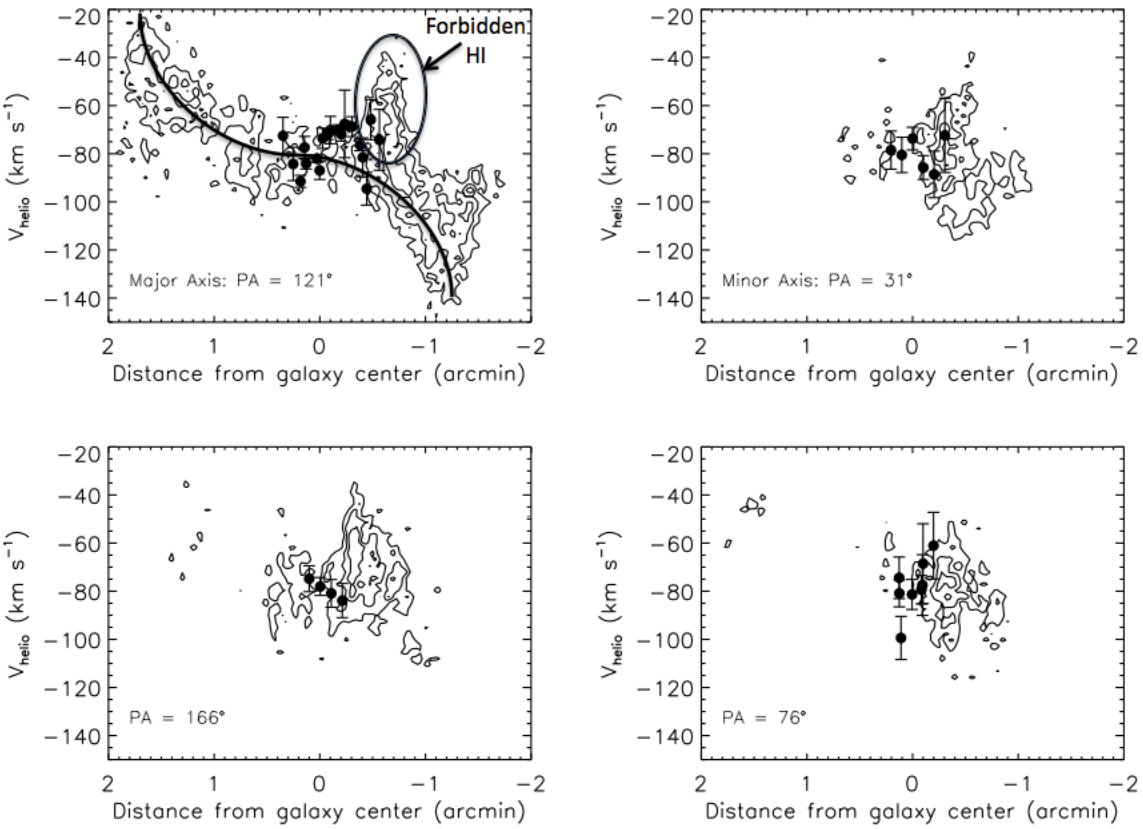

Figure 2.9 Position-velocity diagrams taken along the four optical slit PAs showing HI contours with stellar data over plotted. Positive distance corresponds with eastward direction while negative distance corresponds with westward direction. The solid line in the upper left plot, major axis, shows the ordered rotation of the HI. This line is a best fit line to the HI intensity contours. The oval in the upper left plot identifies the forbidden HI motion, i.e., motion counter to the circular velocity. The stars and the HI follow each other very closely at all four PAs.

To determine the intrinsic velocity dispersions of the stars in NGC 1569 as a function of radius, a correction for instrumental broadening must be made. The instrumental broadening was determined by cross-correlating the template stars with each other. The intrinsic broadening of a single star should be zero, so the FWHM of the cross-correlation of the template stars with each other ($\mathrm{FWHM_{instr}}$) represents the instrumental signature. On average, the $\mathrm{FWHM_{instr}}$ was approximately 42 $\pm$ 2 km $\mathrm{s^{-1}}$. The instrumental $\mathrm{FWHM_{instr}}$ was subtracted in quadrature from the FWHM of the cross-correlation peak of the template stars cross-correlated with the galaxy spectra ($\mathrm{FWHM_{obs}}$). Therefore, using the definition of a Gaussian, the intrinsic velocity dispersions of the stars in NGC 1569 were determined by the following:

$$\sigma = \frac{\sqrt{\mathrm{FWHM_{obs}}^2 - \mathrm{FWHM_{instr}}^2}}{2.354} \tag{2.2}$$

The resulting stellar velocity dispersions are shown in Figure 2.10 for each of the four PAs. The average of the velocity dispersion, σ_{obs}, weighted by the uncertainty of each point, for all four PAs is 21 $\pm$ 4 km $\mathrm{s^{-1}}$.

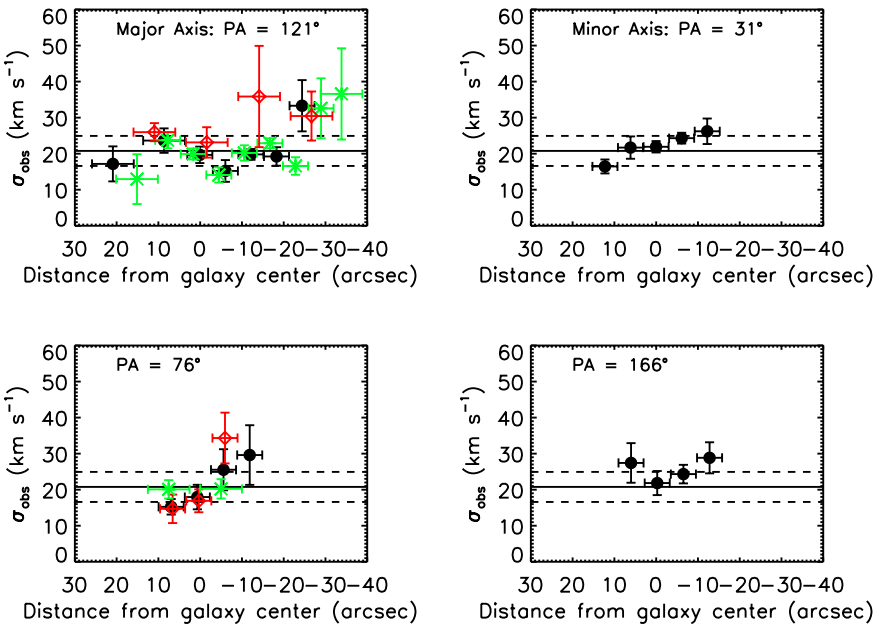

Figure 2.10 Stellar velocity dispersions observed along the four optical slit PAs. Black filled circles, red diamonds, and green stars represent independent points derived from different observing nights. The solid line shows the average velocity dispersion, $< \sigma_z >$ = 21, and the dotted lines indicate the uncertainty, $\pm$ 4 km s^{-1}. Error bars along the x-axis show the spatial range summed along the slit. East is at positive distances from the galaxy center; West are negative distances.

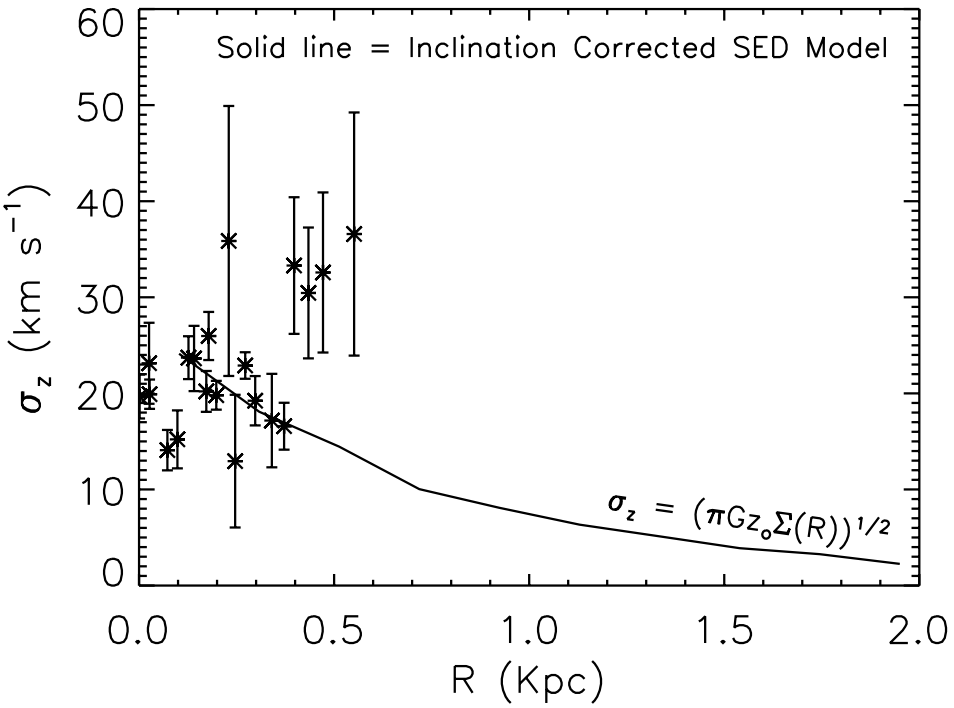

Figure 2.11 Observed stellar velocity dispersions measured from the spectra (star symbols). The solid line represents the inclination-corrected model velocity dispersion expected from the stellar mass surface density, determined from SED fitting (presented in Chapter 4.2). z_o is the stellar scale height. The bulk of the points (R $<$ 0.35 kpc) lie on or near the expected values. But, the points between 0.35 $<$ R $<$ 0.6 kpc are too high, indicating a region of unusually high stellar velocity dispersion. This may be a region where the stellar disk is thicker.

In order to disentangle $\sigma_{\rm R}$ (velocity dispersion in the radial direction), $\sigma_{\rm z}$ (velocity dispersion perpendicular to the disk), and σ_ϕ (velocity dispersion in the tangential direction) from $\sigma_{\rm obs}$, the following relation from Gerssen, Kruijken, & Merrifield (1997) was used:

$$\sigma_{obs}^2 = [\sigma_R^2\ \sin^2(\eta-\theta) + \sigma_\phi^2\ \cos^2(\eta-\theta)]\sin^2 i + \sigma_z^2\ \cos^2 i \tag{2.3}$$

Here, again, η is the observed PA, θ is the major axis PA and i is the inclination of disk. Since the HI and stars are well matched, the better determined inclination of $i = 69^\circ$ and major axis PA of $122^\circ.5$ from the HI kinematics can be used here. Since there are only a few points along each intermediate PA, i.e., $\pm$ 45° from the major axis, a converging result was not possible. Therefore, the major axis was used, where $(\eta - \theta) = 0$, in equation 2.3, thus $\sigma_{\rm R} = 0$. Following Swaters (1999), the assumption was made that the stellar velocity dispersion in the stars follows the MW properties observed for stars near the sun. So, $\sigma_\phi \approx \sigma_{\rm z}$, and, therefore, $\sigma_{\rm obs} = \sigma_{\rm z}$ for the major axis. This relationship is used in Chapter 4.2 and in Figure 2.11, which will be discussed more later.

Swaters (1999) found a relation between integrated $M_{\rm B}$ of a galaxy and the central vertical velocity dispersion:

$$log\ \sigma_z = -0.15 M_{\rm B} - 1.27 \tag{2.4}$$

This relation predicts a σ_z of 21 km s^{-1} for NGC 1569, which is equal to the observed value of 21 km s^{-1}. NGC 1569 agrees well with the overall trend observed in spiral galaxies, i.e., lower luminosity systems have lower velocity dispersions.

2.2 Ionized Gas Spectroscopy

2.2.1 Observations and Data Reductions

The telescope setup for these observations is the same as for the stellar spectral observations except for the use of a different post-slit filter, namely, KP 1547. Due to the filter change, the grating position was adjusted slightly and the spectrograph was re-collimated at the beginning of the fifth night of the 2008 November observing run. The KP 1547 filter has a central wavelength of about 5015 Å and a FWHM of 27 Å, and so, makes a good narrowband filter for targeting the O[III]λ5007 Å emission feature. Both the major and minor axes were observed. Dome flats and twilight flats were taken, as well as one radial velocity standard star that was stepped along the slit spatially in the same fashion as for the other filter, described previously. The cross-correlation method was not used for determining the heliocentric radial velocities of the ionized gas for the O[III] emission line, but instead a multiple Gaussian decomposition procedure described below was used. Therefore, there was no need to observe any radial velocity standard stars like those observed for the stellar spectral data.

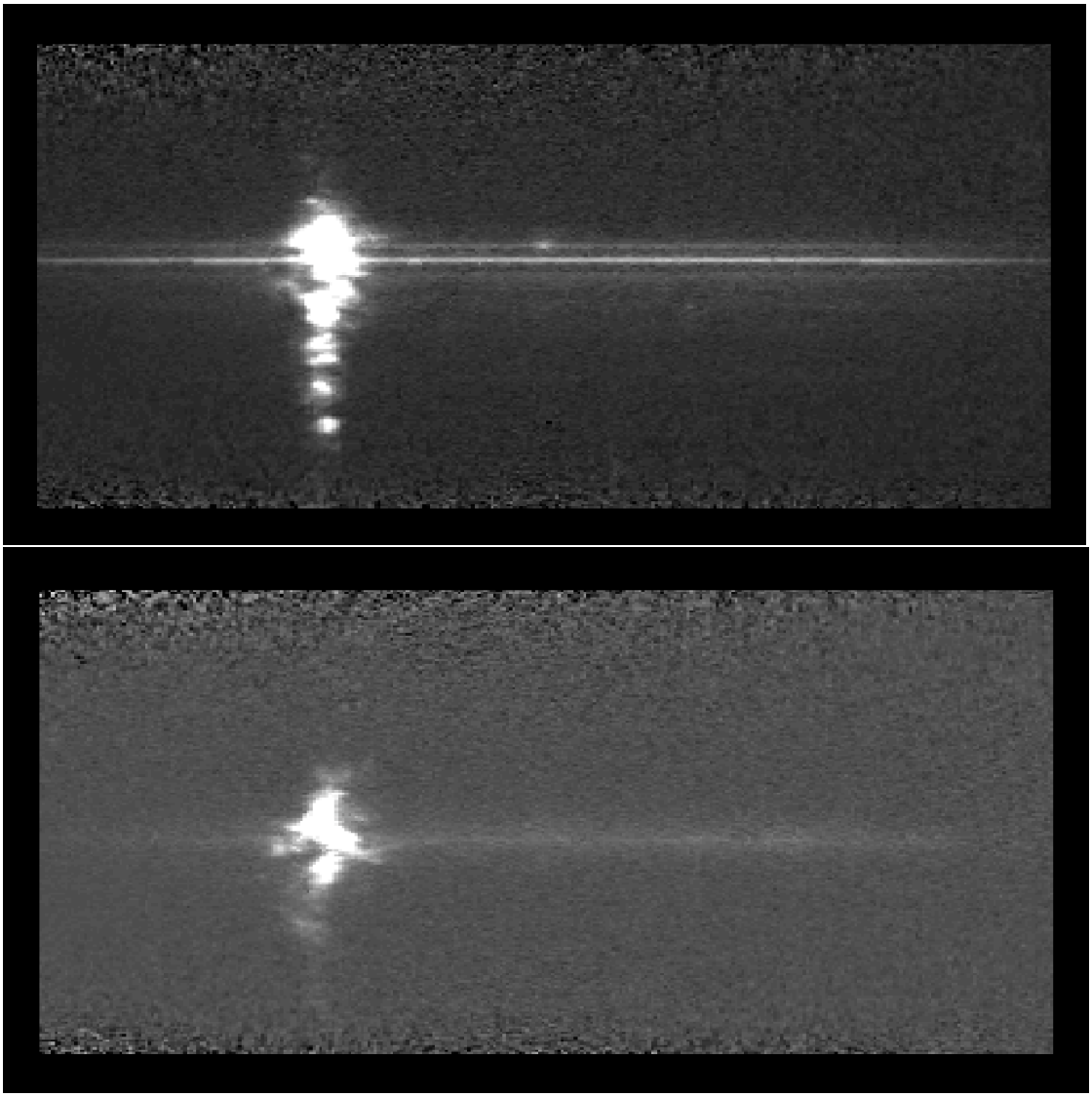

Figure 2.12 Top: Co-added, sky subtracted, two-dimensional spectrum of the O[III]λ5007 Å emission feature for the major axis of NGC 1569. Bottom: Same as top, only for the minor axis. Wavelength is along the horizontal axis ($\sim$41 Å total coverage) and the vertical axis is the spatial direction of the slit ($\sim 3'$). West increases up.

Additionally, comparison lamp exposures were taken after each object image for accurate wavelength calibration. Three galaxy and three sky spectra were obtained for the major axis PA, and three galaxy spectra for the minor axis. However, due to threatening clouds during the course of the night, only one sky image for the minor axis was observed. The sky image was scaled to compensate for the large difference in exposure time. Despite the difficulties, the brightness of the O[III] emission line made it possible to obtain highly resolved emission line spectra. The same data reduction procedure was followed as for the stellar spectral data. Figure 2.12 shows the fully reduced, two-dimensional, co-added, O[III]λ5007 Å emission spectra for the major and minor axes of NGC 1569.

2.2.2 Extracting One-Dimensional Spectra

Due to the starburst nature of NGC 1569, many star forming regions lie throughout the observable disk, and hence, create bright O[III] features seen along the spatial direction of these spectra. Because the emission features are so bright, a single spectrum from each spatial line was able to be extracted, using the IRAF task SCOPY, giving a spatial scale of $1\farcs09$ per pixel (17.7 pc). Also, at this wavelength, a velocity resolution of 27 km s^{-1} was achieved.

2.2.3 Multiple Gaussian Decomposition

In order to determine the velocities of these extracted O[III]λ5007 Å emission spectra, the task SPLOT in IRAF was used. As an example, Figure 2.13 shows a single extracted spectrum of the O[III]λ5007 Å emission feature taken from the major axis.

It is evident that there are three distinct peaks over a total width of 4.1 Å, or, ∼176 km s^{-1}. The SPLOT task is able to disentangle multiple Gaussian components in blended features, such as the ones in Figure 2.13. The three velocities obtained for the peaks in Figure 2.13 are -133.9, -84.2, and -31.5 km s^{-1} spanning a range of over 100 km s^{-1} at a distance of $-13\farcs2$ from the center of the galaxy along the major axis. This fitting procedure was repeated for each spectrum extracted along the slit.

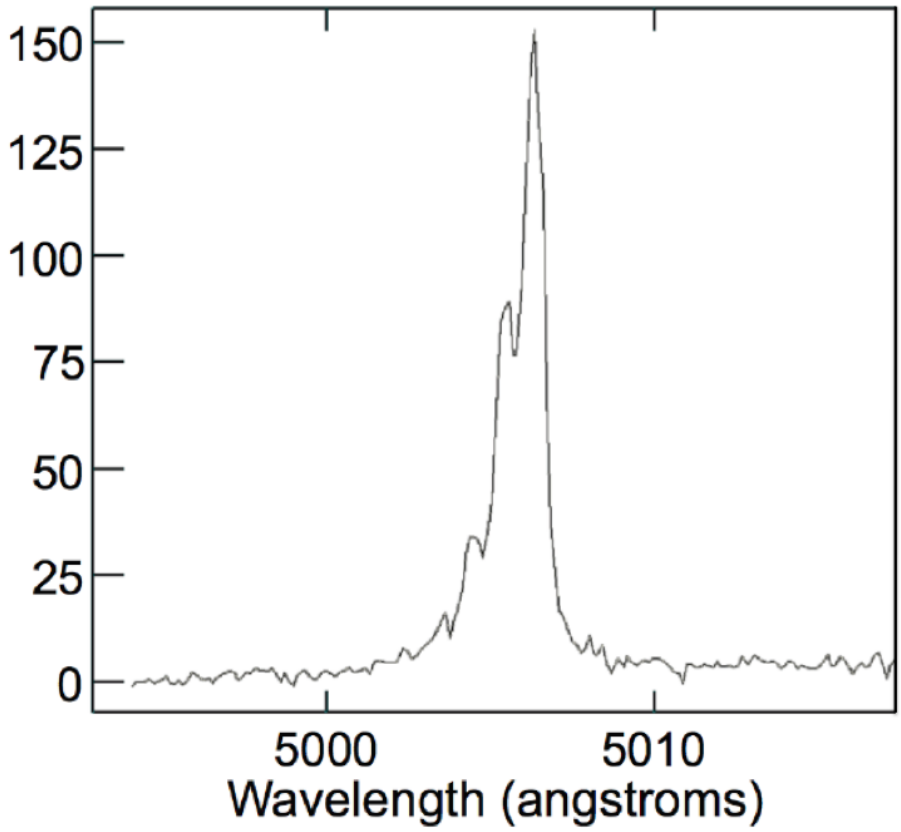

Figure 2.13 A one-dimensional extracted spectrum of the O[III]λ5007 Å emission feature at a radius of -13″ from the center of NGC 1569 along the major axis. Three Gaussian peaks are seen. The total width of the blended emission feature at zero intensity is $\sim$4.1 Å, or, $\sim$176 km s^{-1}.

2.2.4 Results

Figure 2.14 shows the decomposed line-of-sight radial velocities of the ionized gas for the major axis, as well as the stellar and HI velocities for comparison. The HI velocities in this figure come from a P-V slice through the major axis of the HI data cube. There was no deconvolution done to produce these HI velocities, they are simply the observed velocities along the major axis position angle. The velocities of the ionized gas match the velocities of Hα along the major axis as detailed in Tomita et al. (1994). In fact, when the positions and velocities from Tomita et al. are compared, they line up perfectly.

In Figure 2.14, three expanding ionized gas shells are observed whose kinematic signatures are outlined. The expanding shell centered around -20″ from the galaxy center has an expansion velocity of $\sim$70 km s^{-1}, and the stars over plotted in Figure 2.14 perfectly match the velocities of the center component of the ionized gas. These middle velocities of the ionized gas also coincide with the bulk motion of the HI gas. Curiously, this agreement extends to the peculiar dip to lower velocities at the western edge of the oval outline, as pointed to by the black arrow in Figure 2.14. These matches in velocities are presumably HII regions connected with particular bright stars. Within this expanding shell, there is only one HI velocity point. The absence of HI in this region is due to an HI hole from blowout created by SSC A, which will be discussed further in Chapter 5.1.1. SSCs A and B reside at radii -22″ and -12″, respectively. Due to the lack of HI and the matching stellar and ionized gas velocities, even including peculiar motions, it is likely that the stellar spectra

are dominated by a young, luminous stellar population that are associated with HII regions and created the expanding shell from blowout during the most recent star formation episode.

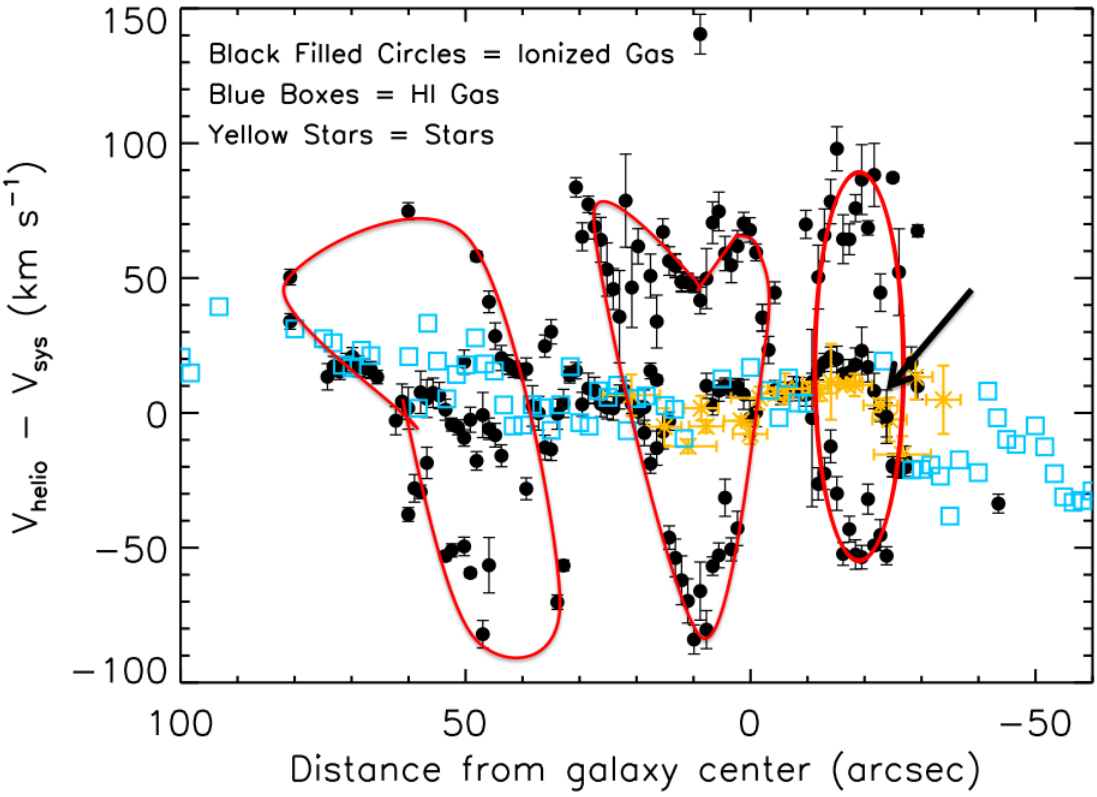

Figure 2.14 Position-velocity plot of the ionized gas (black filled circles), HI gas (blue boxes), and stars (yellow stars) along the major axis. The red polygons outline three expanding gas shells. Note the close correspondence between the stars and ionized gas, including peculiar motions, in the western-most oval. The stars follow the ionized gas that is in the center velocity of the red oval and these velocities also match the neutral gas velocities. The black arrow points to the dip in velocities. East is at positive distances from the galaxy center; West are negative distances.

The expanding shell centered at $+10''$ in Figure 2.14 also shows matching stellar and ionized gas velocities in the center velocity of the shell. Again, since the stars match the central velocities of the ionized gas, i.e., the ordered motion of the galaxy, it is likely that this ionized gas is from nearby HII regions that formed the stars dominating the stellar spectra. The highly peculiar velocities of the ionized gas are likely a superbubble created from blowout produced by the stars that formed in the central velocity HII regions. This shell, however, shows more HI than the shell centered at a radius of -20″, and the velocities of the HI gas match the stars and low velocity ionized gas, all of which are the bulk rotation of the galaxy. Because the stars follow the bulk motion, it is not as obvious as for the western shell, but it is possible that the spectra are dominated by young, luminous stars that were formed in the HII regions centered at $+10''$.

The third and final shell, centered at a distance of $\sim +50''$ does not show any stellar velocities because the signal-to-noise in this region of the stellar spectra was too low to extract any useful stellar information. Perhaps, this expanding ionized gas shell is the most recently formed feature where stars are still in the process of forming and are imbedded in their neonatal gas clouds. Stars do exist in this region as can be seen in the V-band image (see Figure 2.1). However, due to the exponential drop-off in the stellar light, the surface brightness is low here. Studies of HII regions of NGC 1569 (Greve et al. 1996; Hunter et al. 1993; Waller 1991; Götz et al. 1990; Young, Gallagher, & Hunter 1984) show that there is star formation in the region of the eastern shell, but it is not as intense as that at the other end of the galaxy. On the other hand, it could be that this is an older area of the galaxy where all

of the young, bright stars have evolved away from the main sequence leaving lower luminosity, older stars behind that the stellar spectra were not able to detect. One can only speculate if the stars in this region ($+50''$ from the center) are young or old because they are not directly observed with our stellar spectra due to their faint collective light. Again, note that the velocities of the ionized HII regions and HI gas agree well in this area.

– 3 –

High Resolution HI Data from the VLA

3.1 Introduction

All of the high-resolution HI data that are used in determining the gas kinematics of NGC 1569 come from the THINGS survey. THINGS was a large study conducted using the VLA, B-, C-, and D-array configurations for the purpose of obtaining 21 cm emission line, HI data on 34 nearby galaxies (Walter et al. 2008). These HI data have both high spatial resolution, $\sim 6''$, and spectral resolution, ≤ 5.2 km s^{-1}.

The THINGS calibrated uv-line data were used, but a new multi-scale cleaning algorithm (MSCLEAN) was implemented using the Astronomical Image Processing System (AIPS[1]) for imaging the HI data of NGC 1569 (see, e.g., Cornwell 2008; Rich et al. 2008; Greisen et al. 2009). This MSCLEAN algorithm produced four final cubes with spatial resolutions of $135''$, $45''$, $15''$, and $0''$, respectively. A beam size of $7\farcs71$ x $7\farcs04$ (RA x DEC) and a channel separation of 2.58 km s^{-1} was achieved as well as a field of view of $51\farcm2$ x $51\farcm2$ (RA x DEC). Figure 3.1 shows the total integrated HI spectrum of NGC 1569. At velocities 0 to $\sim$ -20 km s^{-1}, the apparent absorption seen in the spectrum is from confusion with the MW. Here, the emission from NGC 1569 is less than that of the foreground MW emission. So, when the MSCLEAN algorithm subtracts the MW emission from NGC 1569's emission, a negative "bowl" is observed in the data cube in the corresponding velocity channels and, hence, it appears as absorption in the integrated spectrum.

[1]The Astronomical Image Processing System (AIPS) has been developed by the NRAO.

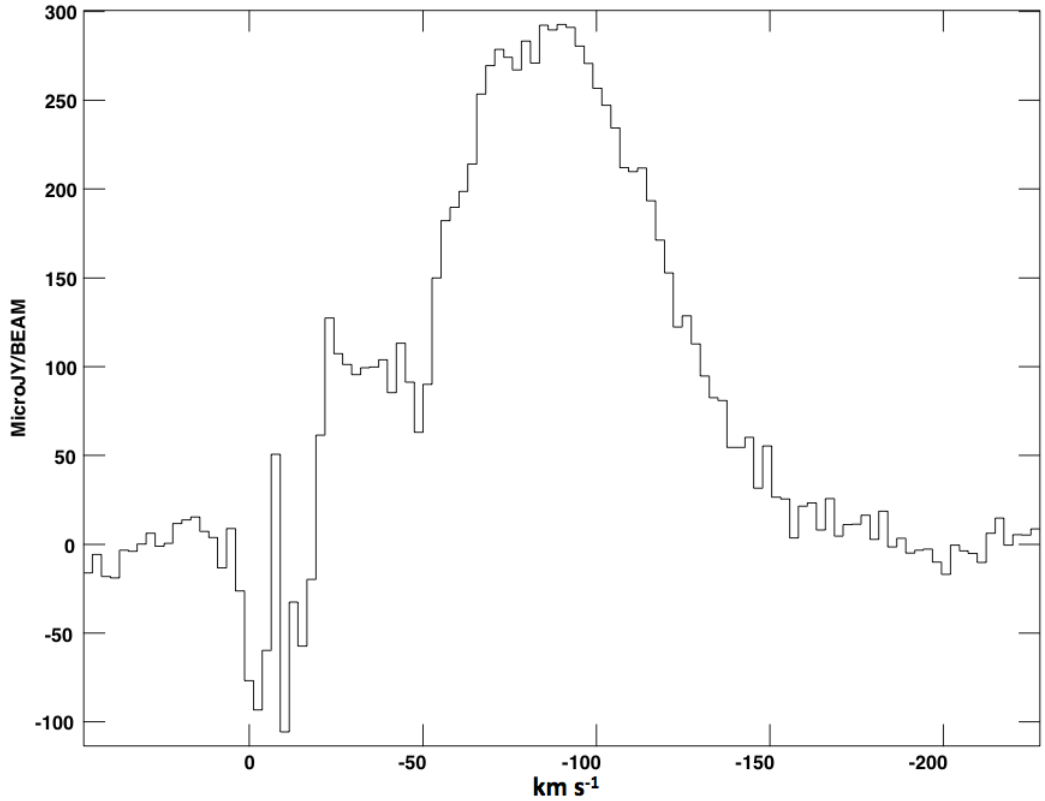

Figure 3.1 Integrated HI spectrum of NGC 1569. The spectrum is centered at -90 km s^{-1} and the integration occurred over a small box containing NGC 1569 and not over the entire field of view. The integration box has bottom left corner coordinates of (RA = 04^{h}:31^{m}:38.50^{s}, DEC = $+64°$:$47'$:$18.30''$) and top right corner coordinates of (RA = 04^{h}:30^{m}:04.82^{s}, DEC = $+64°$:$53'$:$51.65''$). This was done in order omit MW emission contamination from the uncleaned area surrounding NGC 1569.

MSCLEAN produces a single cube, the 0″ cube, that has both correct flux and correct noise, which is a great advantage over standard cleaning methods. For a comprehensive review of the multi-scale cleaning algorithm, please see Ficut-Vicas et al. (in preparation) and for a brief description see Appendix A. Figure 3.2 shows the LITTLE THINGS integrated flux map. See Appendix B for an explanation of the flux to surface density transformation used for the intensity scale. Figure 3.2 shows tenuous emission to the south and northeast of the galaxy that was imaged for the first time due to the capabilities of the multi-scale cleaning algorithm. This extended emission will be discussed further in Chapter 6.

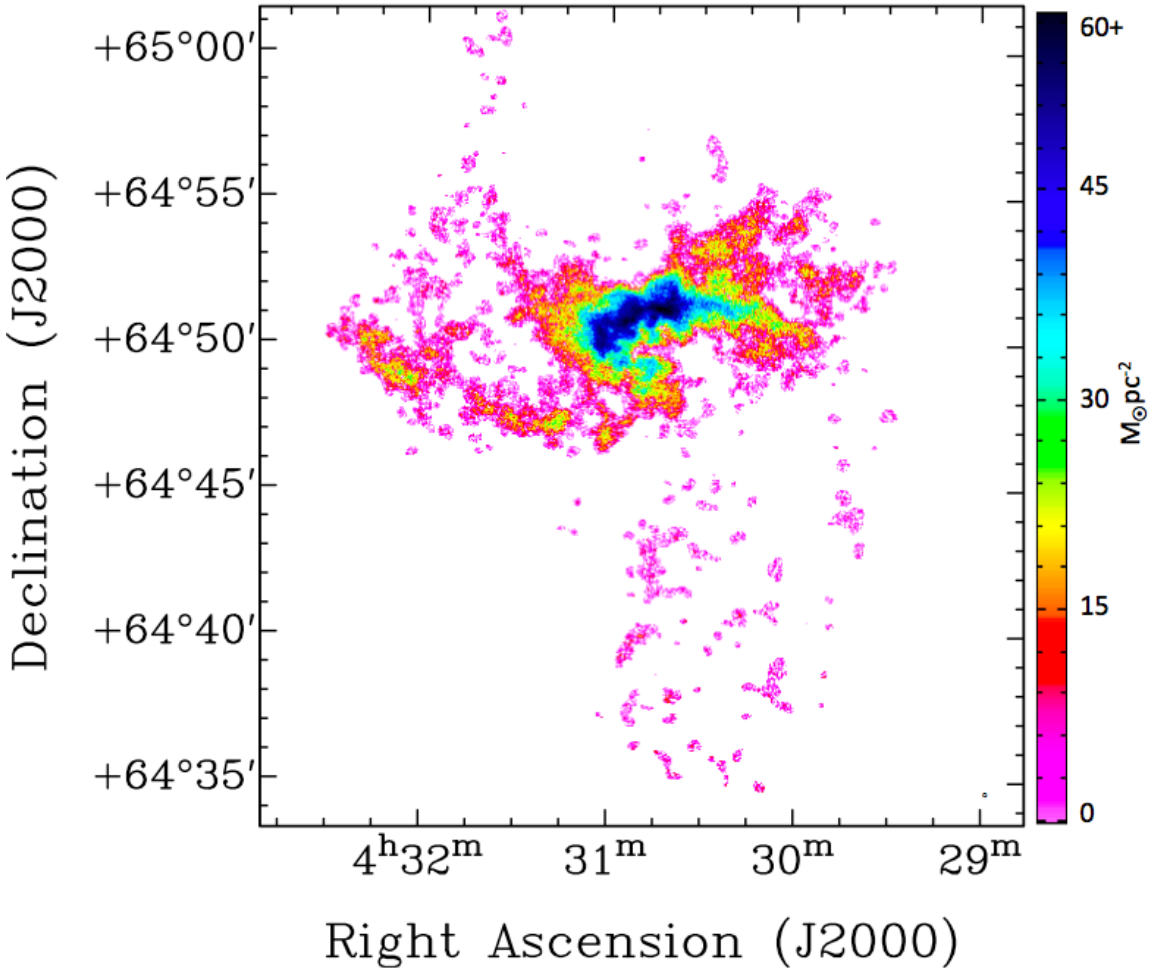

Figure 3.2 Integrated HI flux map of NGC 1569. The multi-scale cleaning algorithm implemented by LITTLE THINGS was able to image tenuous emission to the south and northeast for the first time.

3.2 Extracting the HI Bulk Velocity Field

This section presents the results from a double Gaussian decomposition method used in order to extract the bulk HI velocity field.[2]

3.2.1 Tilted Ring Models

Rotation curves have been widely used for assessing the dynamics of galaxies. They can be derived from observing the stellar kinematics or nebular emission in a galaxy disk, but they can also be determined from high-resolution HI data that frequently extend far beyond the stellar disk. For example, analyses of stellar rotation curves from the emission spectra of nebular emission regions of nearby spiral galaxies provided the first evidence of unknown dark matter on galaxy scales and HI rotation curves showed that the rotation curves remained flat as far as could be measured (Rubin & Ford 1970; Rubin et al. 1978; Navarro et al. 1995; Bosma 1981). Here, the THINGS HI data, imaged with the new MSCLEAN algorithm, is used to determine the rotation of the HI gas for NGC 1569.

One common method of constructing rotation curves of disk galaxies from high-resolution HI data is the tilted ring model in which the galaxy is divided up into individual annuli, which are fit separately (Begeman 1989). The first step in applying this model is to create a two-dimensional velocity field out of a three-dimensional HI data cube. Then, from the extracted velocity map, a series of ring parameters are determined by independently fitting a series of concentric, circular rings in the plane of the disk. The ring parameters are: inclination of the galaxy disk (i); PA of the

[2]Se-Heon Oh contributed to the bulk velocity field extraction and asymmetric drift correction described in the following sections. The author is very grateful for Oh's participation in this work.

major axis (θ) measured east from north; kinematic center (X_{pos}, Y_{pos}); systemic velocity ($V_{\rm sys}$); expansion velocity in the radial direction of the disk ($V_{\rm exp}$); and the rotational velocity ($V_{\rm rot}$). The ring size and spacing between rings must be fixed and usually determined using the beam size as the smallest ring radius and ring width. In the tilted ring model, these rotational parameters are determined by assuming an axisymmetric thin disk with closed circular orbits and are fit independently to each ring in succession.

This technique is applied in order to extract the rotation curve of NGC 1569. Usually, one uses the intensity-weighted velocity field, shown in Figure 3.3, but due to the dominance of non-circular motions, this method cannot be applied directly here. Therefore, a two-dimensional velocity field for the ordered, bulk rotation must first be extracted.

3.2.2 The Bulk Velocity Field

NGC 1569 shows a dominance of non-circular, random motions as seen in the intensity-weighted mean velocity field, moment 1 map, in Figure 3.3. In Figure 3.3, the light and dark blue features across NGC 1569 show the high velocity HI clouds that are offset from the bulk motion of the galaxy disk. A 'typical' rotating disk galaxy generally displays a grading scale of isovelocity contours with high velocity HI on one side and low velocity HI on the opposite side. The systemic velocity of the system separates the two halves. This is not what is observed here. The velocities appear to be scattered randomly across the galaxy disk. However, a method developed by Oh et al. (2008) can extract bulk rotation from even chaotic systems like NGC 1569.

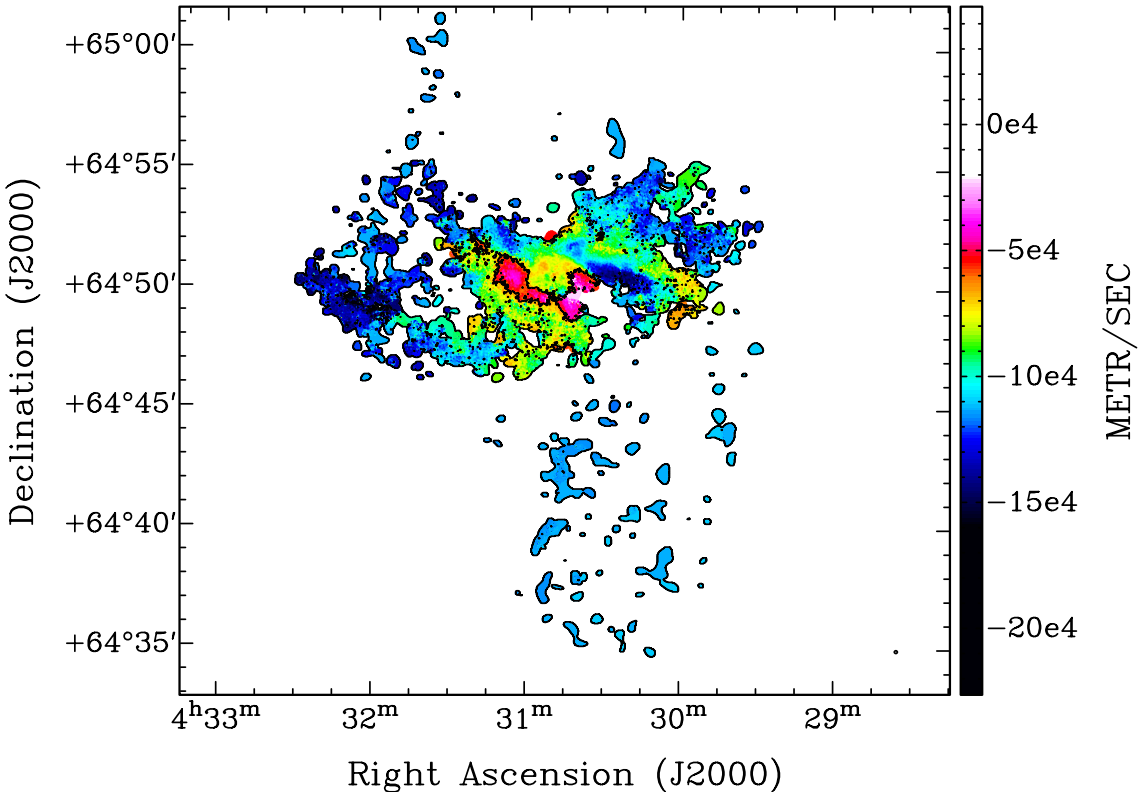

Figure 3.3 Intensity-weighted HI velocity field of NGC 1569.

To extract the bulk motion, a double Gaussian deconvolution procedure is used that separates velocities of HI clouds superimposed upon each other at a given position in the HI data cube. The velocities derived from the central wavelengths of the extracted Gaussian peaks are then compared to a model velocity field. This model velocity field, and its derivation, are described in detail in Appendix C along with the bulk extraction procedure. At each position in the galaxy, if there are two distinct velocities detected, then, the velocity that most closely resembles the model velocity field is extracted into a bulk motion map while the outlying velocity is extracted into one of two non-circular motion maps. The *strong* non-circular motion map contains all velocities that are derived from Gaussian peaks that have a *higher* intensity than the bulk motion velocity, while the *weak* non-circular motion map contains all velocities that are derived from Gaussian peaks that have a *lower* intensity than the bulk motion velocity.

Figures 3.4 and 3.5 show examples of strong and weak non-circular velocity peaks, respectively, in NGC 1569 in comparison to the bulk velocity peak. As shown in Figure 3.5, for NGC 1569, even the weak non-circular velocities challenge the bulk rotation peaks as the intensity of the peaks are almost comparable.

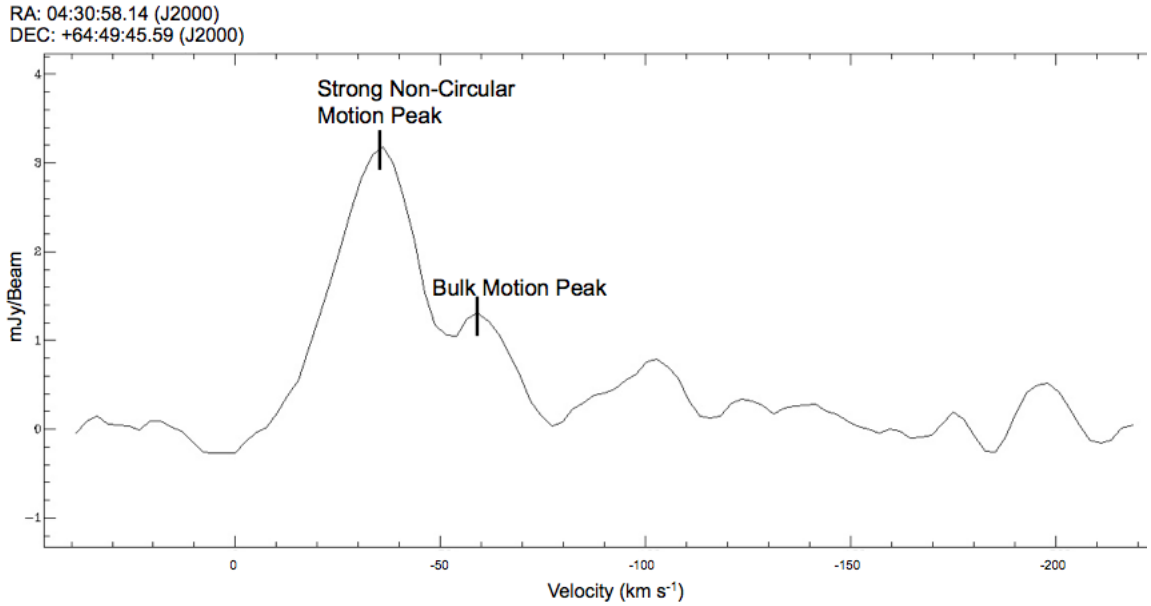

Figure 3.4 Example of a line profile through a single position within NGC 1569 demonstrating a strong non-circular motion peak. The peak flux is higher than that of the bulk motion peak. The RA and DEC of this line profile are given in the upper left corner of the graph.

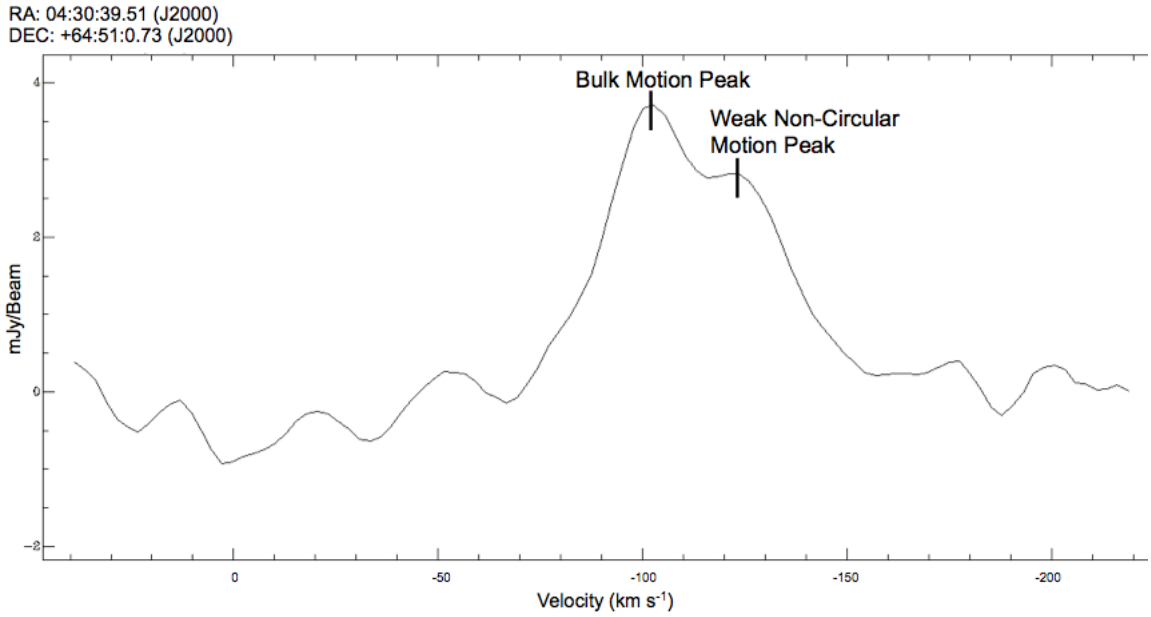

Figure 3.5 Example of a line profile demonstrating a weak non-circular motion peak that is a lower flux than the bulk motion peak. The RA and DEC of the position where this line profile was extracted are given in the upper left corner of the graph.

Figure 3.6 shows (a) the final bulk velocity map, (b) the strong non-circular velocity map, (c) the weak non-circular velocity map, and (d) the strong non-circular motions superimposed on the weak non-circular motions map. The solid black line indicates the position and observed length of the major axis of the stellar spectra. The black oval in each panel of Figure 3.6 identifies an HI cloud that has systemic motions significantly deviating from the bulk motion of the galaxy. In fact, this cloud is virtually absent in the bulk velocity field (see panel (a) in Figure 3.6). This cloud may be in-falling into the galaxy and be responsible for the starburst activity. This is discussed in more detail in Chapter 6.3. In Chapter 3.3, the HI rotation curve is derived using this two-dimensional bulk velocity field and the tilted ring model.

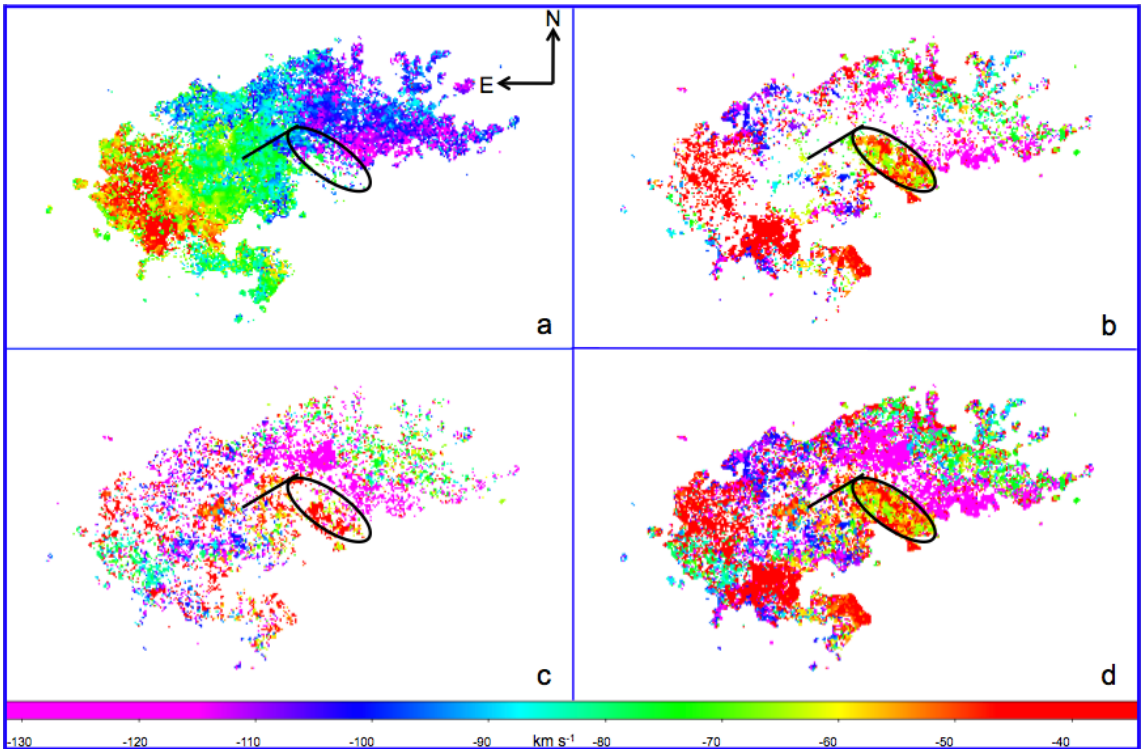

Figure 3.6 Results of the kinematic deconvolution procedure of Oh et al. (2008): (a) Bulk rotation map. (b) Strong non-circular motion map. (c) Weak non-circular motion map. (d) Combined strong + weak motion map. The black oval identifies a strong non-circular motion HI cloud that is believed to be responsible for the recent starburst. The black line identifies the position and length of the slit along the major axis used in the stellar spectroscopy.

3.3 HI Rotation Curve

To determine the rotation curve of NGC 1569 the Groningen Image Processing SYstem (GIPSY[3]) task ROTCUR is used, which applies the tilted ring model discussed in Chapter 3.2.1. The inputs for ROTCUR are the bulk velocity field, Figure 3.6a, along with the initial values for the rotation parameters (see Chapter 3.2.1). Figure 3.7 shows the results of the observed rotation curve derived after eight iterations of the bulk extraction procedure and tilted ring analysis. Table 1.2 lists the final values of the rotational parameters determined from the tilted ring model. A maximum rotational velocity, $V_{\rm rot}$, of 33 $\pm$ 10 km s^{-1} is found, which was calculated from the average of the last nine data points in Figure 3.7. The systematic error, shown in the lower right corner of Figure 3.7, is high due to the low signal-to-noise in the bulk velocity field. Although Figure 3.7 shows a turnover near the end of the rotation curve, the velocities may not truly identify a constant velocity region of the disk. The signal-to-noise is very low and, hence, the data are unreliable at radii greater than 2 kpc. The implications for this turnover, or lack thereof, are discussed in the following chapter.

[3]The Groningen Image Processing SYstem (GIPSY) has been developed by the Kapteyn Astronomical Institute.

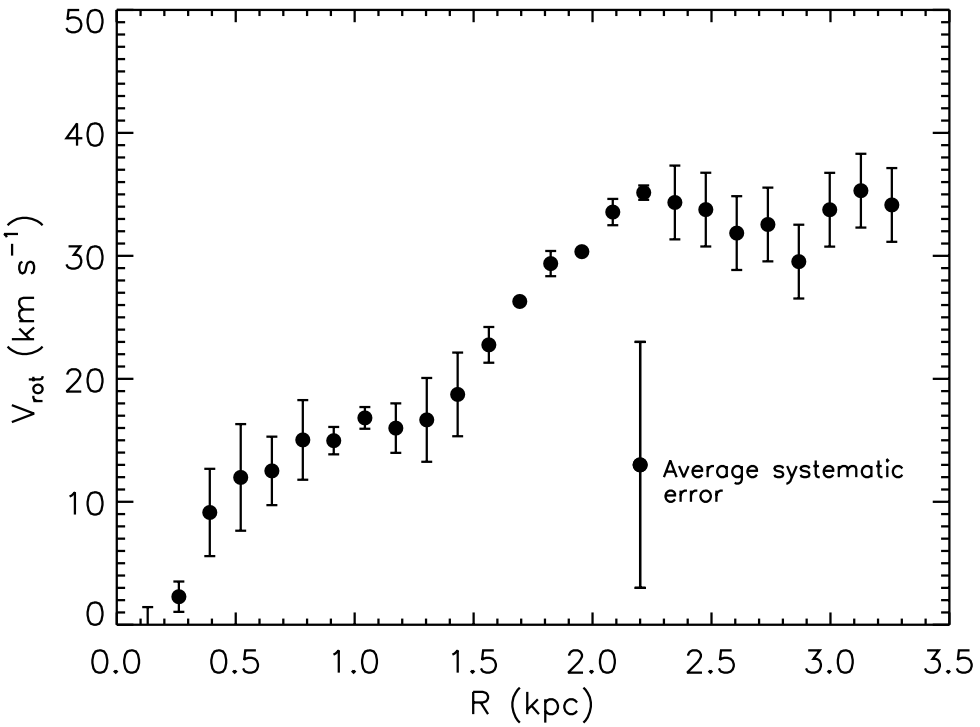

Figure 3.7 Measured rotation curve of the HI gas determined from the bulk motion map using a tilted ring model. A $V_{\rm rot}$ of 33 km s^{-1} is determined from averaging over the region where the curve is flat from ∼2.0 - 3.2 kpc. The errors on the rotation curve points are the standard deviations calculated by assuming a solid body rotation out to 2.0 kpc. The average systematic error is shown for reference.

3.4 Asymmetric Drift Correction to HI Rotation Curve

Because of the high HI velocity dispersions, the observed rotation curve must be corrected for pressure gradients in the radial direction, i.e., asymmetric drift, that can slow down the intrinsic gas rotation. Figure 3.8 shows a velocity dispersion map of the bulk velocity field. This map was created from the bulk velocity field, shown in Figure 3.6(a), by extracting the FWHM values of the Gaussian peaks that were fit to

each bulk velocity. The HI velocity dispersion is high, $< \sigma_{\rm HI} > = 23$ km s^{-1}, compared to the observed rotational speed, $V_{\rm rot} = 33 \pm 10$ km s^{-1}. Therefore, following Bureau & Carignan (2002), the observed bulk rotation curve is corrected for the asymmetric drift, using the following equations, to determine the intrinsic $V_{\rm max}$:

$$\sigma_{\rm D}^2 = -R\ \sigma_{\rm HI}^2\ \frac{\partial\ ln(\Sigma_{\rm HI}\ \sigma_{\rm HI}^2)}{\partial R} \tag{3.1}$$

$$V_{max}^2 = V_{rot}^2 + \sigma_D^2 \tag{3.2}$$

Here, $\sigma_{\rm D}$ is the drift correction, R is the radius, $\sigma_{\rm HI}$ is the HI velocity dispersion, and $\Sigma_{\rm HI}$ is the HI surface density (see Oh 2009 for more details).

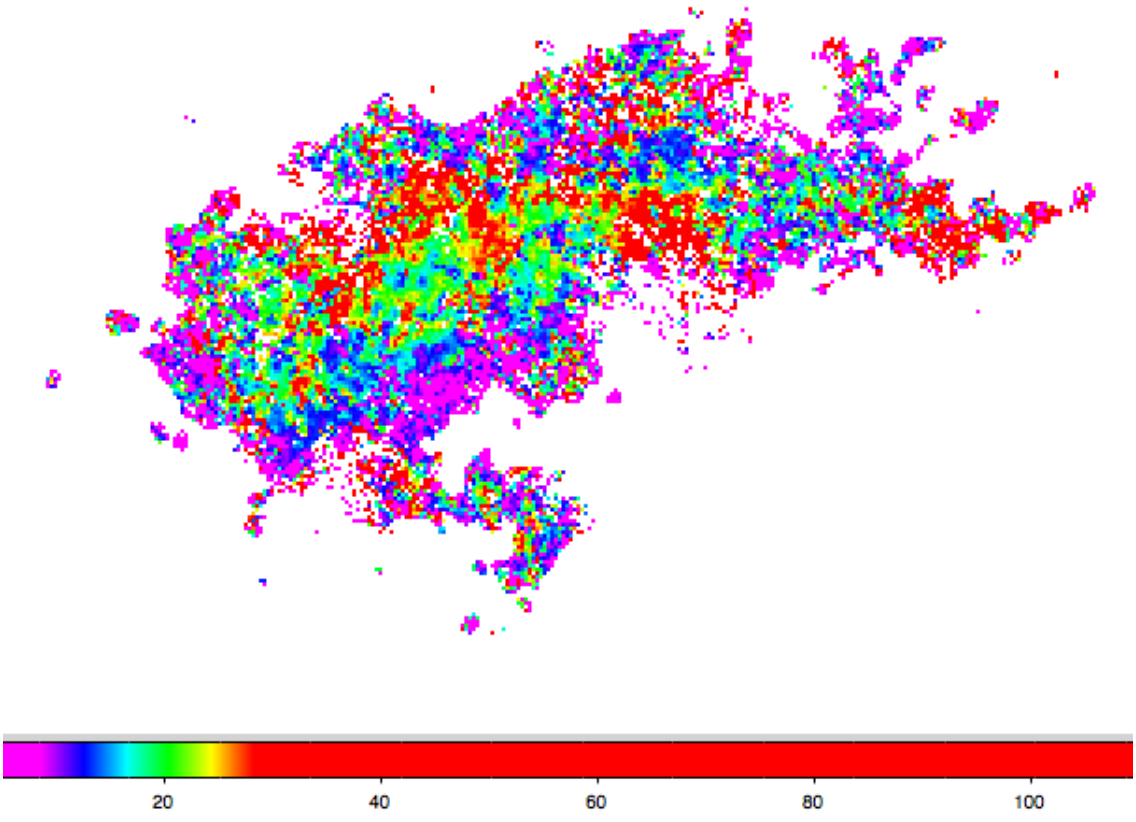

Figure 3.8 FWHM map of the bulk velocity field determined from a signal-to-noise above 2σ. This represents the velocity dispersion in the gas, minus the gas engaged in non-circular motions.

Figure 3.9 shows four plots that outline the steps taken for the asymmetric drift correction, which is described in the following paragraphs. All of the panels in this figure have a maximum radius of about 2 kpc because after this point, the signal-to-noise in the HI bulk motion velocity field, top panel of Figure 3.6, drops off and the solutions become unstable. Therefore, from this point forward the kinematics of the gas in NGC 1569 are evaluated out to a maximum radius of 120″, which, at the distance of NGC 1569, is equal to 1.96 kpc. Figure 3.10 shows the bulk velocity field with a 120″ ring overlaid. It is clear that beyond this ring, the extracted galaxy emission becomes flocculent and irregular.

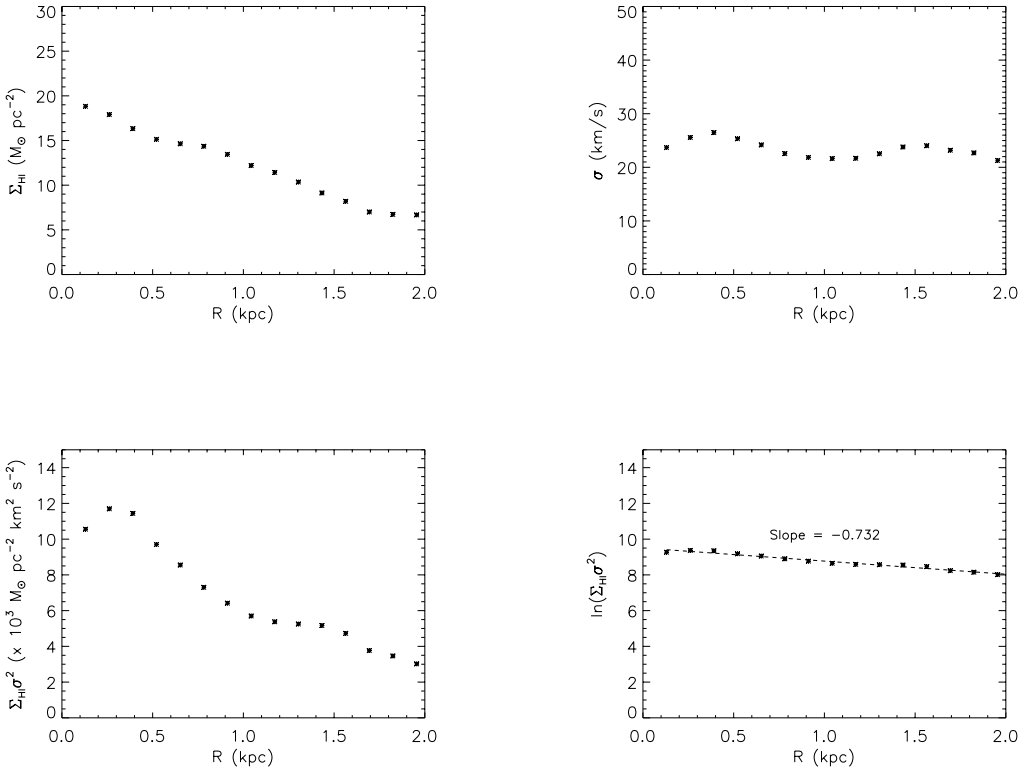

Figure 3.9 Top, Left: Mass surface density profile of HI. Top, Right: HI velocity dispersion as a function of radius. Bottom, Left: HI mass surface density multiplied by the velocity dispersion as a function of radius. Bottom, Right: Natural logarithm of the bottom, left plot. The slope of this line is used in the asymmetric drift correction function.

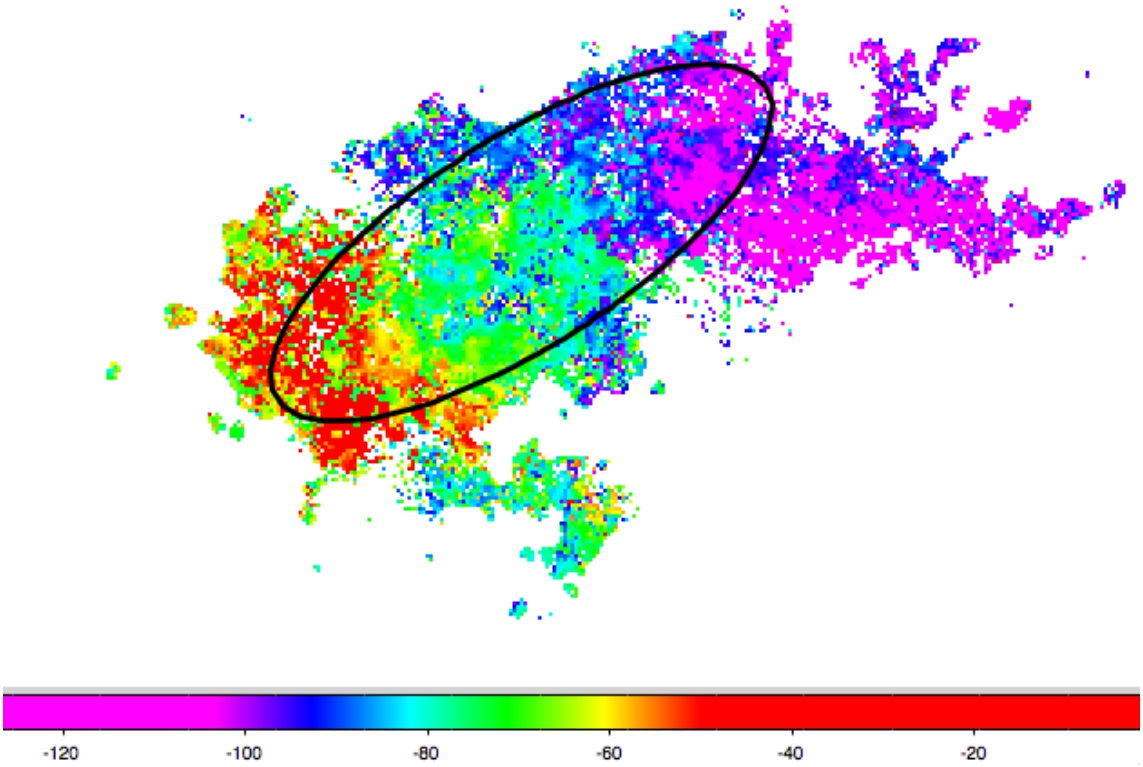

Figure 3.10 Bulk velocity field showing the 120″ radius for which all kinematics are determined for the HI.

For input into Equation 3.1, a surface density profile is created from the integrated intensity map, moment 0 map, shown in Figure 3.2. The GIPSY task ELLINT is used to create integrated concentric elliptical rings using the same parameters determined in the tilted ring model. A factor of 1.4 is included to account for helium and metals and the assumption that all Hydrogen is in atomic form is made. This HI surface density profile is shown in the upper left panel of Figure 3.9.

To calculate the velocity dispersion profile as a function of radius, the GIPSY task ELLINT is again implemented only this time with the intensity weighted velocity dispersion map, moment 2 map, shown in Figure 3.11. The same tilted ring parameters are used, and the HI velocity dispersion profile, shown in upper right panel of Figure 3.9, is derived. Thirdly, the HI surface density profile, from the first step, is multiplied by the HI velocity dispersion profile, from the second step, and the plot in the lower left panel of Figure 3.9 is obtained. And, finally, the natural log of this profile is taken and a slope of the resulting line is determined. The slope has a value of -0.732 and is equal to $\frac{\partial\ ln(\Sigma\ \sigma^2)}{\partial R}$, in Equation 3.1 above. This asymmetric drift correction is applied to all of the velocities in the rotation curve.

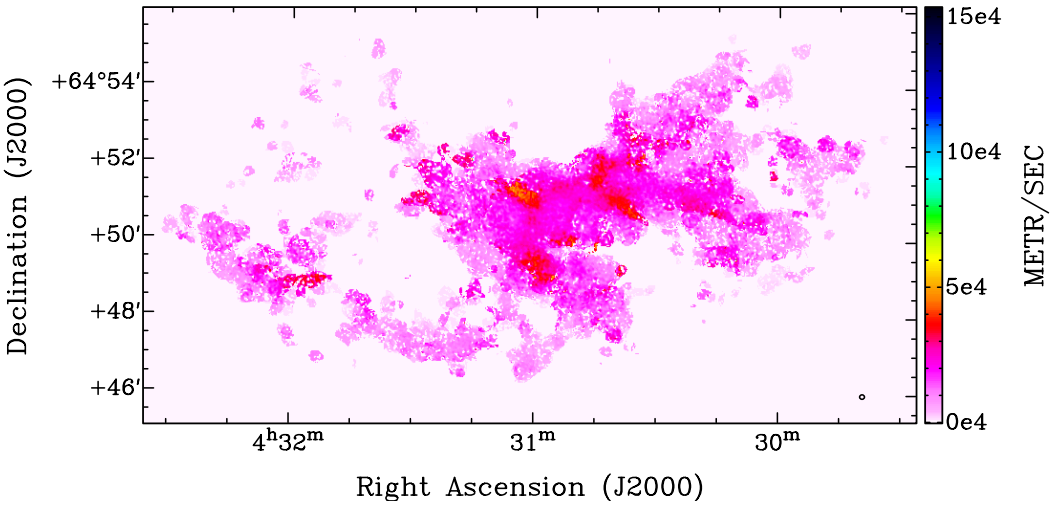

Figure 3.11 Intensity weighted velocity dispersion map from LITTLE THINGS.

Figure 4.3 shows the HI bulk rotation curve derived from the tilted ring model along with the asymmetric drift corrected HI bulk rotation curve. The maximum rotation velocity, determined from HI, increased from the observed $V_{\rm rot} = 33$ km s^{-1} to $V_{\rm max} = 50$ km s^{-1}.

– 4 –

Mass Modeling for the Stars and Gas

4.1 Introduction

Here, the mass modeling of NGC 1569 is discussed. The total baryonic mass in stars and gas is determined. Then, the dynamical mass is calculated from the rotation curve and the dark matter contribution is separated.

4.2 Stellar Mass

To determine the stellar mass as a function of radius, a mass-to-light (M/L) ratio of the stars is needed, but determining accurate M/L ratios in galaxies is a difficult task. Many factors such as limitations in stellar population synthesis (SPS) modeling, the stellar initial mass function (IMF), metallicity, dust, age and recent star formation complicate M/L ratio determinations. For example, NGC 1569 is a post-starburst system, hence modeling the mass assuming a continuous star formation history (SFH) is not reasonable. The widely used Bell & de Jong (2001) stellar models for determining the total mass in stars within spiral disk galaxies make the assumption that there is a smooth SFH and produces a stellar mass of only $\sim$3 x 10^6 $M_\odot$ for NGC 1569, but the combined mass of the three SSCs alone is $\sim$2 x 10^6 $M_\odot$ (Grocholski et al. 2008). Therefore, to more adequately take the SFH into account, the surface stellar mass density is determined by modeling the spectral energy distributions (SEDs) (including *Spitzer* 3.6 μm, 2MASS JHKs and UBV photometry) with stellar population synthesis techniques (Zhang et al. submitted).

It has been known that dwarf galaxies exhibit a diversity of SFHs, so the usually adopted two-component (e.g. exponentially declining plus burst) SED modeling method may bias the modeling parameters, such as the stellar mass. In this study, to avoid the assumption of a form for the SFH, the whole lifetime (here, it is fixed at 12 Gyr) is logarithmically divided into 6 age bins, and the SFR in each age bin is assumed to be constant. Then a SFH library was generated by allowing the SFR of these age bins to vary independently.

Specifically, the Charlot & Bruzual (in preparation, hereafter CB11) population evolution models are used. Compared to the Bruzual & Charlot (2003) models, CB11 implemented a recently improved treatment of the thermally pulsing asymptotic giant branch (TP-AGB; Marigo & Girardi 2007), which is especially relevant to young stellar populations. The Chabrier (2003) stellar IMF, which has a lower-mass cutoff of 0.1 $M_{\odot}$, was adopted in this work. For the internal extinction, the dust attenuation recipe developed by Charlot & Fall (2000) is used, which takes into account different extinction for young ($\leq$ 10 Myr) and old stellar populations. The extinction ratio of the young to old populations is simply fixed at 3, which is the typical value found by Charlot and Fall. The metallicities of the population models are allowed to vary as 0.02, 0.2, or 0.4 $Z_{\odot}$.

The final SFH library consists of a multi-dimensional grid of $\sim 10^7$ models. For each annulus in the galaxy the surface stellar mass density was determined using the Bayesian technique. For each model SED, a probability density function (PDF) was constructed, and the cumulative distribution function (CDF) for the whole range of stellar mass defining the SFHs library was derived by calculating the likelihood

$\sim e^{(-\chi^2)}$ for each model in the library. The most probable stellar mass is taken as the weighted mean of the corresponding PDF, and the uncertainty is derived by cutting off the 16% tail at each end of the PDF.

The multi-band surface photometry is corrected for MW foreground extinction and inclination. Due to the low Galactic latitude of NGC 1569, the MW extinction (and also its uncertainty) toward NGC 1569 is significant. A color excess of E(B-V) = 0.60 mag is used for the foreground MW reddening, which is the average between the value of 0.51 mag given by Burstein & Heiles (1982) and the 0.70 mag given by Schlegel et al. (1998). There is no assumption made about a reddening gradient across NGC 1569. The Cardelli et al. (1989) extinction law is adopted in calculating the appropriate MW extinction at each band. The *Spitzer* 3.6 μm data could have a significant contribution from hot dust in intense starburst regions (Zhang et al. 2010). So, for the inner starburst regions of NGC 1569, the 3.6 μm photometry is excluded from the SED fitting. As expected, the 3.6 μm photometry is more than 0.2 magnitude brighter compared to that predicted from the SED (including 2MASS JHK) fitting.

The results from the SED modeling are presented in Figure 4.1. The right panel of Figure 4.1 shows the cumulative summed stellar mass as a function of radius from the SED fitting. The exponential profile approaches the horizontal asymptote at a mass of $\log(M) = 8.44 \Rightarrow 2.8 \times 10^8$ $M_\odot$, giving the total stellar mass of NGC 1569. The left panel of Figure 4.1 shows the exponential surface density mass profile, corrected for inclination. The stellar mass density profile is a broken or double exponential. For these data, no assumptions are made about disk scale height or constant mass-to-light

ratio. When an $R^{1/4}$ profile, which is appropriate for triaxial systems, is compared to the surface mass density in Figure 4.1, it is clear that it does not fit the data as well as the exponential profile.

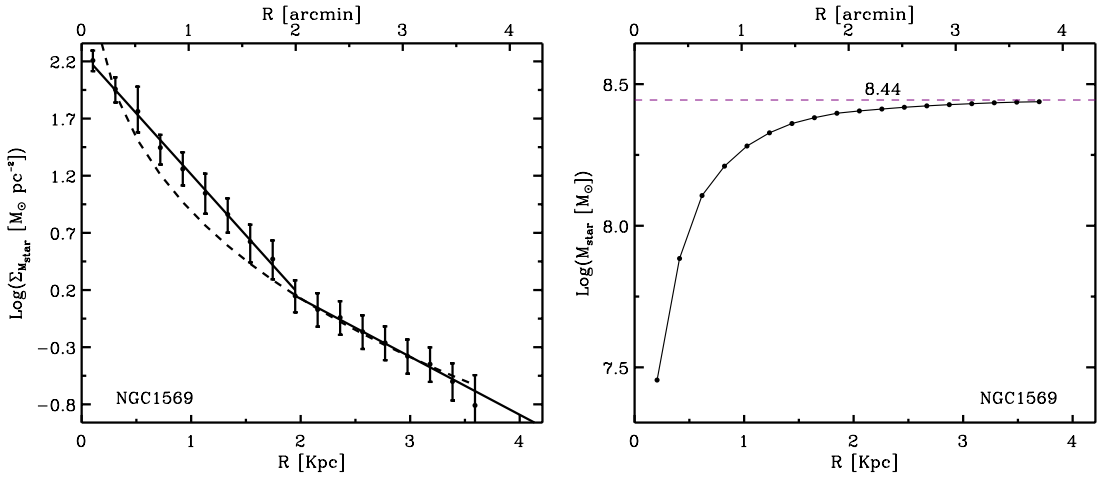

Figure 4.1 Left: Logarithmic stellar mass surface density profile from fitting the SED in elliptical annuli. This has been corrected for an inclination of 69°. The solid lines are a fit to the profile and represent an exponential disk. The dashed line represents an $R^{1/4}$ fit to the surface density profile where the assumption of a constant mass-to-light ratio and constant disk scale height is made. An exponential disk is a better fit than an $R^{1/4}$. Right: Logarithmic integrated stellar mass for NGC 1569 from the elliptical annuli SED fitting.

To see how the $R^{1/4}$ profile compares to the more traditional surface *brightness* profile, a plot of the 3.6 μm photometry surface brightness is made in Figure 4.2. A marginally better fit to the exponential profile is observed over the $R^{1/4}$ profile. The $R^{1/4}$ profile overestimates the surface brightness in the center and underestimates it at $\sim$0.5 kpc. Therefore, the $R^{1/4}$ profile does not fit the data as well as the exponential profile in the inner region of the stellar disk for the surface brightness profile, but especially for the surface mass density. In conclusion, the mass profile of NGC 1569 is best fit as a double exponential disk.

In Figure 4.2, there is a break in the exponential profile around 1.3 kpc where it becomes flatter in the outer disk. This surface brightness profile is a Type III "antitruncated" profile, as described by Erwin et al. (2005). A Type III profile is ascribed to disk flaring in the outer disk in M94 by Herrmann & Ciardullo (2009). They attribute this characteristic to a recent interaction or merger in M94. If this type of surface brightness profile is generally indicative of a flared disk resulting from an interaction or merger, then this would be evidence for an outside influence on NGC 1569.

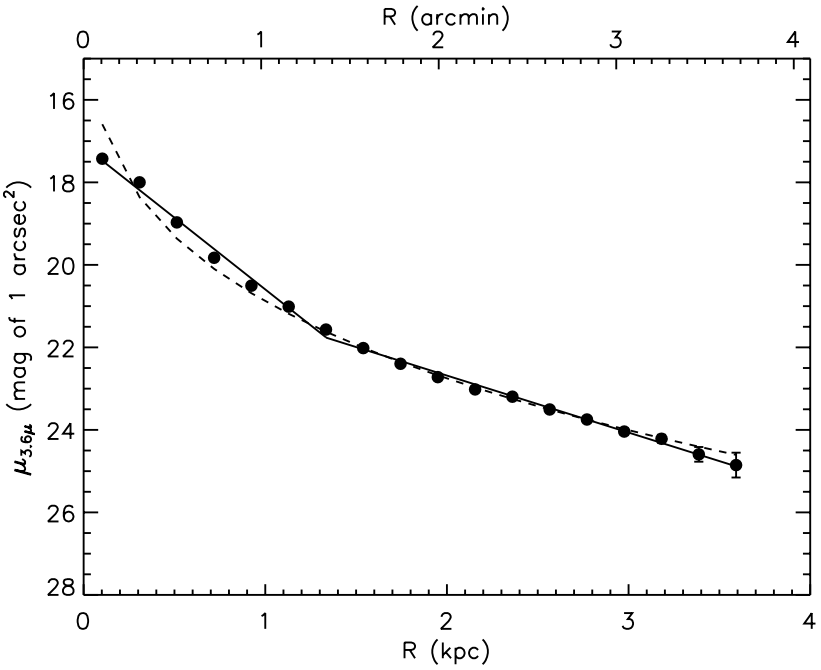

Figure 4.2 Inclination corrected 3.6 μm surface brightness profile. The solid lines are an exponential fit to the profile, and the dashed line represents an $R^{1/4}$ fit. The broken exponential profile fits the data better than the $R^{1/4}$ profile.

To check the validity of the derived stellar surface mass density profile, the observed stellar kinematics are implemented. From Swaters (1999, and references therein), the relationship between vertical stellar velocity dispersion, σ_z, and stellar surface mass density, $\Sigma(R)$ is used:

$$\sigma_z = \sqrt{\pi G z_o \Sigma(R)} \tag{4.1}$$

Here, z_o is the vertical scale height. A vertical $sech^2 z$ scale-height distribution for the stellar component with the empirical relationship determined from spiral galaxies, $h/z_o = 5$ (van der Kruit & Searle 1981) is assumed, where h and z_o are the disk scale-length and scale-height, respectively. From an exponential disk fit to the inner part of the 3.6 μm surface brightness profile, a scale-length, h, of 1.54 kpc is derived, giving a scale-height, z_o, of 0.31 kpc for NGC 1569. Figure 2.11 shows the observed stellar velocity dispersions, plotted so that all radii are positive, along with the model velocity dispersion profile derived from Equation 4.1.

In Figure 2.11, there is general agreement between the observed and predicted stellar velocity dispersions in the center, however, the observed stellar velocity dispersions increase as a function of radius, which is opposite of what is expected. Perhaps this is indicative of a disturbance in the stellar disk at around a radius of 0.4 kpc from the galaxy center. It is not known how the stars act beyond $\sim$0.5 kpc, as the spectra do not probe past this radius, so, no definitive determination can be made for what happens beyond this peculiarity and, its implications for the disk structure.

Using the GIPSY task ROTMOD, the stellar surface density profile was applied, as determined from the SED fitting, to model the expected velocities of the stars.

The assumption that all of the mass is in the stars that are fit by the SED fitting procedure is made, thus, an upper stellar mass limit is achieved. The results for this model are shown in Figure 4.3. The graph also shows that in the inner 1 kpc, half of the observable disk of NGC 1569, the gravitational potential is dominated by the observed stellar mass. Again, the signal-to-noise for the HI kinematic data is only reliable out to 2 kpc, but, the graph is displayed out to 2.5 kpc for comparison to the HI.

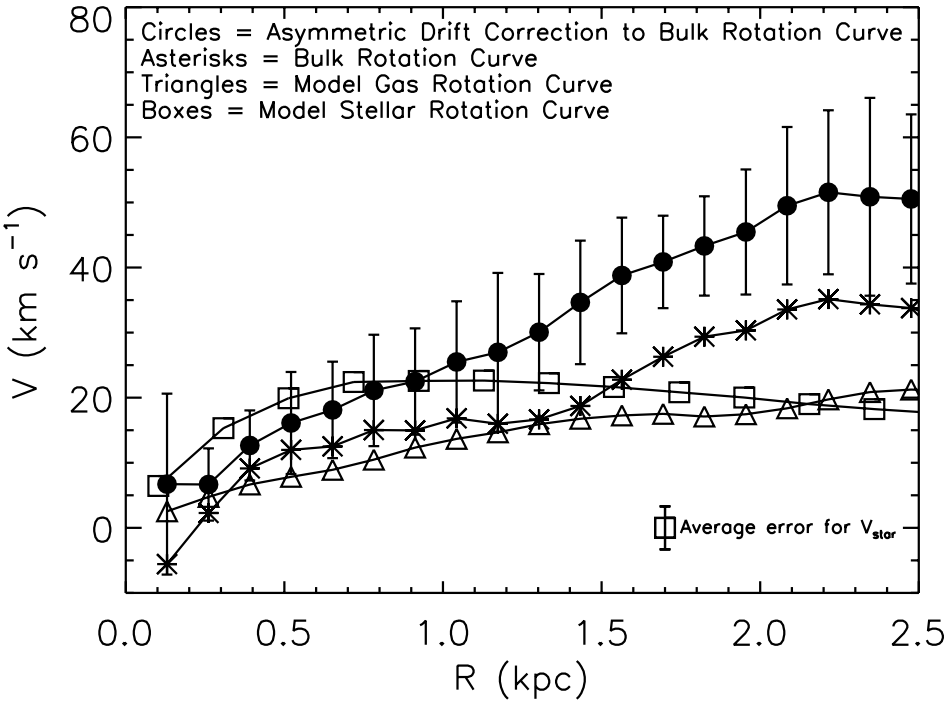

Figure 4.3 Mass modeling of both the stars (boxes) and the gas (triangles) along with the observed bulk rotation curve (stars) and the asymmetric drift corrected rotation curve (filled circles). The average uncertainty for the model stellar rotation are shown in the lower right corner for comparison to the asymmetric drift corrected rotation curve. Within the uncertainties, the stellar mass dominates the entire rotation curve out to 1 kpc, half of the observable stellar and gas disks.

4.3 Gas Mass

The total HI mass of NGC 1569, summed over the entire integrated HI map, Figure 3.2, is 2.3 x 10^8 $M_\odot$ and the average column density, $N_{\rm HI}$, over the galaxy is 2.8 x 10^{19} cm^{-2}. See Appendix B for a detailed explanation for how the total gas mass and column density were derived. To calculate the expected velocities of the gas, based on Newtonian dynamics, as a function of radius, the mass surface density profile of the HI is used. An axisymmetric infinitely thin disk comprised entirely of gas is assumed and the GIPSY task ROTMOD is used (see Oh et al. 2011 for more details). The same procedure used for the stellar velocity profile is followed and the expected model HI rotation curve in Figure 4.3 is derived.

The asymmetric drift-corrected observed rotation curve is plotted in Figure 4.3. Also plotted, is the model stellar rotation curve, discussed in Chapter 4.2, and the model HI rotation curve. It is clear in Figure 4.3 that the model velocities for the stars and gas, determined from their respective mass surface densities, are less than the observed rotation curve velocities at radii greater than 1.7 kpc both before and after the asymmetric drift correction. The maximum rotation velocity of the model HI rotation curve is 18 km s^{-1}, less than half of the asymmetric drift corrected $V_{\rm max}$. This, of course, is known as the missing mass problem. Dark matter is assumed to be the reason for the difference between the observed and model velocities. The dark matter implications will be discussed further in Chapter 4.4.

NGC 1569 also contains molecular hydrogen (H_2). According to Israel (1988), the amount of H_2 in NGC 1569 as a whole is $\sim$ 2 x 10^7 $M_\odot$, which is about 5 x 10^7 $M_\odot$ corrected for the 3.36 Mpc distance. This produces the ratio $M_{\rm H_2}/M_{\rm HI} = 0.2$ over the

galaxy as a whole. The estimate of the total H_2 is a rough approximation, though, because it has been scaled for distance here as well as in Israel's work; and, Israel determined the total H_2 mass by scaling the results derived by Young et al. (1984) for the central 50″ of the galaxy. However, the scaled mass agrees with Obreschkow & Rawlings (2009) who find an H_2 mass of $\sim$ 2 x 10^7 $M_\odot$, corrected for a distance of 3.36 Mpc. In either case, the order of magnitude suggests that the total amount of H_2 is on the order of 10% of the total baryonic mass (stars + gas) in NGC 1569. Figure 5.4 shows the approximate location and projected size of two giant molecular clouds (GMCs) identified by Taylor et al. (1999, see Figures 3 and 4). These GMCs will be discussed further in Chapter 5.1.2.

4.4 Dark Matter Mass

A detailed method has been shown for determining the rotation due to the mass in stars and rotation due to the mass in gas. Here, the dark matter content in NGC 1569 is explored by assuming that the observed, asymmetric drift corrected, rotation represents motion under the total gravitational potential of the system. Using the $V_{\rm max} = 50$ km s^{-1}, a dynamical mass, $M_{\rm dyn}$, of 1.1 x 10^9 $M_\odot$ within a radius of 2 kpc is calculated, using the following equation:

$$M_{\rm dyn}(R) = \frac{V_{\rm max}^2 \, R}{G} \tag{4.2}$$

where, $V_{\rm max}$ is the maximum rotation speed determined from the asymmetric drift corrected rotation curve, and R is the radius where $V_{\rm max}$ is measured. Previously, a total HI mass was determined from the integrated HI map of 2.3 x 10^8 $M_\odot$ (see

Chapter 4.3) and a total stellar mass of 2.8 x 10^8 $M_\odot$ was derived (see Chapter 4.2). However, it is necessary to account for helium and other metals, which were not taken into account when the HI integrated flux map was summed over. Therefore, the HI mass is scaled by a factor of 1.4, which is typical of the metallicity of dwarf galaxies (de Blok et al. 2008), and a total baryonic mass of 6.1 x 10^8 $M_\odot$ is achieved. Subtracting this from the dynamical mass, only 4.9 x 10^8 $M_\odot$ of missing, dark matter within a radius of 2 kpc is left. This is less than the total baryonic mass in NGC 1569.

For the dark matter determination, it is assumed that the turnover radius is found and, hence, the maximum rotation, $V_{\rm max}$, of NGC 1569. However, as mentioned in Chapter 4.3, the signal-to-noise is low in the region where the turnover radius occurs, thus it is uncertain if the intrinsic $V_{\rm max}$ of this system has been identified. If the true maximum rotation speed of the galaxy is actually higher, then the calculation of the dynamical mass, along with the deduced dark matter mass, of NGC 1569 will be underestimated. Furthermore, the edge of the disk mass cannot be definitively seen in the data meaning that the radius of the disk could go on for quite some length. The dynamical mass increases with radius. Also, these calculations use a $V_{\rm max}$ derived under the assumption that the inclination of the HI disk is 69°, which is a rough estimate from the tilted ring model. Therefore, the calculated dynamical mass is expected to be a lower limit at the 2 kpc radius, which is where it was determined. However, if a $V_{\rm max}$ of 50 km s^{-1} is correct, then NGC 1569 has a low dark matter content inside the visible disk, which is unlike any other dwarf galaxy studied (e.g. Oh et al. 2011; Sawala et al. 2011; Walker et al. 2009).

To see the effect of such a low dark matter content in the inner region of the disk of NGC 1569, the dark matter fraction, $\gamma_{\rm dm}(\frac{M_{\rm DM}}{M_{\rm tot}})$, as a function of radius is examined using the following equation given in Oh et al. (2011):

$$\gamma_{\rm dm}(R) = \frac{M_{\rm DM}}{M_{\rm tot}} = \frac{V_{\rm max}(R)^2 - V_{\rm star}(R)^2 - V_{\rm gas}(R)^2}{V_{\rm max}(R)^2} \tag{4.3}$$

where $V_{\rm max}$ is the maximum rotation velocity corrected for asymmetric drift derived from HI, $V_{\rm star}$ is the stellar rotation velocity assuming all the mass is in the stars determined from the SED fitting, and $V_{\rm gas}$ is the gas rotation velocity determined from the HI surface density assuming Newtonian dynamics. Figure 4.4 shows the fraction of dark matter as a function of radius. Most of the values in the inner 1 kpc are negative due to the dominance of the stars. However, in the outer region, beyond 1.5 kpc, the fraction of dark matter is positive, although, even here the values are far below the the average of 0.7 found for a sample of seven dwarf galaxies by Oh et al. Furthermore, the negative dark matter fractions in the inner regions, which are from the over-dominance of the model stellar rotation compared to the rotation curve in the inner 1 kpc, were not observed in any of Oh et al.'s seven dwarf galaxies. Could NGC 1569 be dark matter deficient?

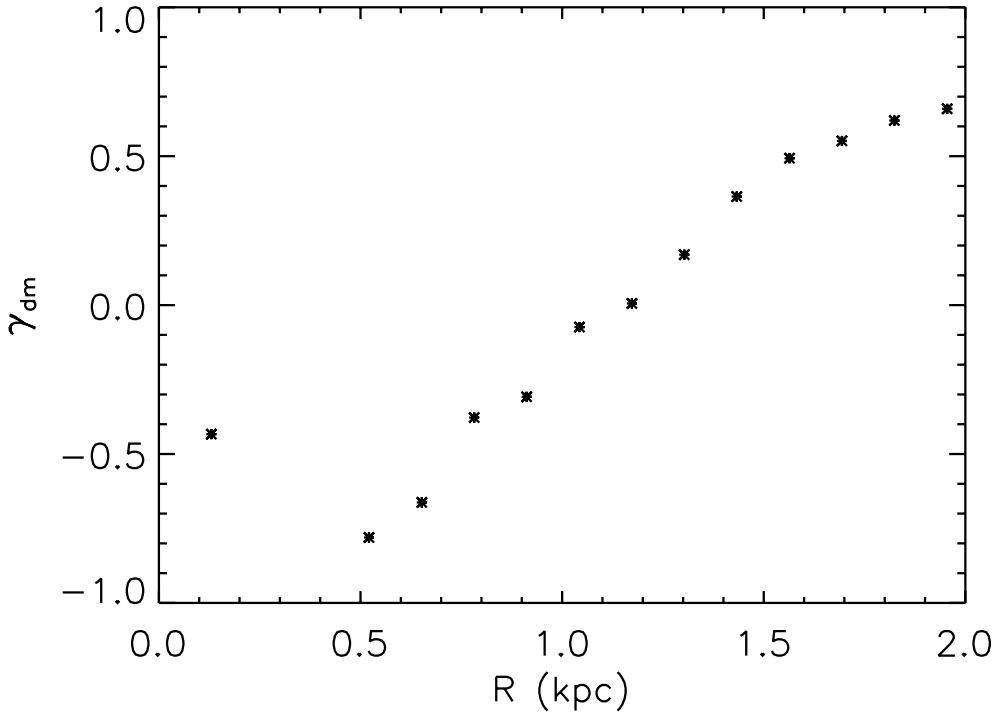

Figure 4.4 Dark matter fraction, γ_{dm}, as a function of radius. The negative dark matter fractions are due to the over-dominance of the stellar rotation curve in the inner regions of the disk. Other dwarfs, by contrast, have γ_{dm} of $\sim$0.7 on average over their entire disks.

To explore this question, cosmological models that assume Cold Dark Matter and a flat universe (ΛCDM) are explored. Erik Tollerud was consulted on employing the results from these simulations in this work. In ΛCDM, the dark matter halos hosting galaxies have an approximately universal shape that follows a concentration-mass relation (e.g. Bullock et al. 2001, Prada et al. 2011). Hence, CDM halos are a one-parameter family, typically parameterized by mass within the virialized extent ($M_{\rm vir}$) or maximum circular velocity ($V_{\rm max}$). Adding the *ansantz* that there is a monotonic mapping of dark matter halo mass to galaxy luminosity (e.g., the brightest galaxies are hosted by the most massive dark matter halos), a galaxy's dark matter halo can be uniquely determined from its luminosity using the technique of abundance matching (Kravtsov et al. 2004, Vale & Ostriker 2004, Conroy & Wechsler 2009). Here, abundance matching is performed, as described in detail in Tollerud et al. (2011a), using the halo $V_{\rm max}$ function from the Millenium II simulation (Boylan-Kolchin et al. 2009) and the r band galaxy luminosity functions of Blanton et al. (2005). The r band absolute magnitude for NGC 1569 ($M_r = -17.6$) is determined from the SED fit described in Chapter 4.2, and this is used to infer that the halo of NGC 1569 has $V_{\rm max} = 95$ km s^{-1}. This implies $M_{\rm vir} \approx 1.6 \times 10^{11} M_{\odot}$, and the virial extent of the halo is $R_{\rm vir} \approx 140$ kpc.

With these values for the total mass of NGC 1569's dark matter halo, the concentration-mass relation implies a unique shape for the halo profile. As outlined in Tollerud et al. (2011b), the halo shape is parameterized using a Navarro, Frenk, & White (1997) (NFW) halo profile and the shape parameters are assigned so that the halo falls on the median of the concentration-mass relation. Figure 4.5 shows the NFW density

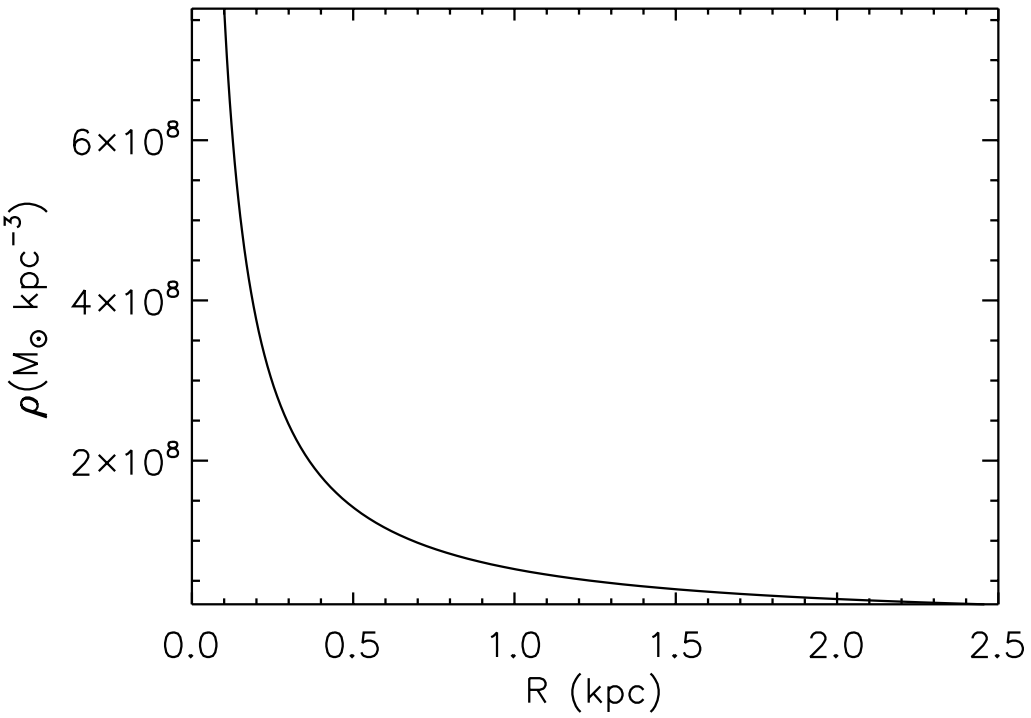

Figure 4.5 NFW density profile from the abundance matching method, assuming an $M_r = -17.6$.

profile as a function of radius for NGC 1569. The resulting circular velocity profile is given as the solid line in Figure 4.6. Figure 4.7 shows the inner region of the NFW profile, solid line, as compared to the modeled gas and stellar masses.

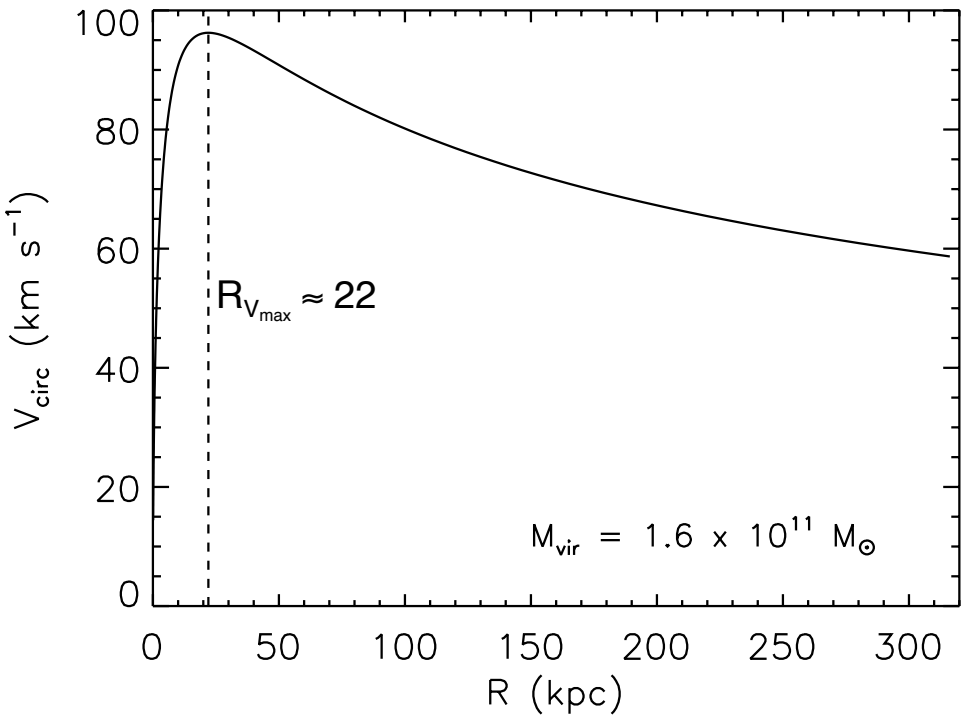

Figure 4.6 NFW velocity profile for the abundance matching method, assuming an $M_r = -17.6$.

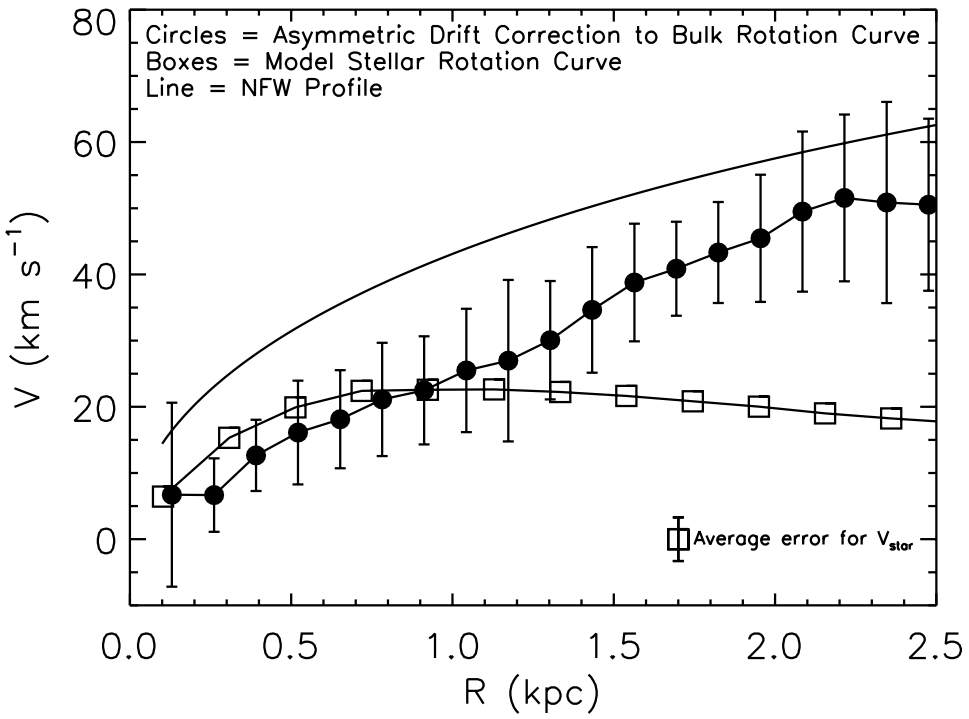

Figure 4.7 NFW profile, solid line, plotted with the modeled gas velocities, filled circles, and modeled stellar velocities, open squares.

It is apparent that the NFW profile predicts slightly more dark matter at $R \sim 1$ kpc than the rotation curve allows, a clear indication of the well-known core-cusp problem of dwarf galaxies (e.g. de Blok 2010 and references therein). However, as is clear from Figures 4.3 and 4.7, the stellar mass is close to the expected dark matter mass in this region, and the uncertain effect of the baryons on the dark matter halo should be significant here. Thus, it is ambiguous whether or not the apparent deficiency of dark matter implies a halo profile inconsistent with ΛCDM, or simply that the baryonic mass of the galaxy is altering the shape of the dark matter halo in the region where the dark matter does not dominate the gravitational forces.

By $R \sim 2$ kpc, however, the ΛCDM prediction lies within the error bars of the measured rotation curve. This further implies that the hint of a turn-around in the rotation curve mentioned in Chapter 3.3 is likely to be an artifact of low signal-to-noise, as the rotation curve implied by this halo profile does not peak until $R \approx 20$ kpc, far beyond the baryonic extent of the galaxy. Additionally, it implies that in a global sense, NGC 1569 is not dark matter deficient - for the largest radius at which the mass can be directly probed, the rotation curve is consistent with ΛCDM predictions.

– 5 –

NGC 1569 as a Dwarf Galaxy in Transition

5.1 Discussion

In this chapter, the results of the integrated kinematic data from the stars, ionized and neutral gas of NGC 1569 are presented. First, the gas and stellar kinematics are compared and then, the kinematics are discussed with respect to the morphology of the galaxy. Finally, a picture of NGC 1569 as a galaxy in transition is described.

5.1.1 Kinematics

In this section, the integrated kinematics of the stars and the gas are compared as well as the location of kinematic features. P-V diagrams made from slicing the HI data cube along the four PAs used for the stellar spectra are shown in Figure 2.9. This includes all motion of the gas: rotation plus peculiar velocities. The stellar velocities are also shown. Positive and negative distance from the galaxy center correspond with eastward and westward directions, respectively. In all four PAs, the stars and the integrated HI gas are observed moving together within the error bars.

The upper left plot in Figure 2.9, which is for the major axis, shows forbidden HI motion in the upper right quadrant between -40 and -70 km s^{-1} at around a distance of -0.′6 from the galaxy center. At some positions between distances of 0′ and -0.′5 the stellar velocities follow the velocity trend of the forbidden rotation, meaning motion counter to ordered rotation, while at some of the positions around -0.′4, the stellar velocities follow the ordered rotation of the HI disk.

Could the gas and stars be showing evidence of counter-rotation? If this were counter-rotation, then one would expect HI contours in the lower left quadrant, which is not observed. Therefore, the forbidden HI motion is identified as an HI cloud in non-circular motion that is moving counter to the overall rotation of the underlying HI disk. In fact, this HI is the northeastern tip of the strong non-circular motion HI cloud identified by the black oval in Figure 3.6. The major axis, PA = 122.°5, slices through the tip of the cloud within the black oval in Figure 3.6. This is seen by the black line in each panel of Figure 3.6 as it denotes the major axis position of the slit. The velocities of this cloud in the strong non-circular motion map, panel (b) of Figure 3.6, match the velocities of the contours in Figure 2.9. Therefore, it is reasonable to conclude that the forbidden HI in Figure 2.9 is an HI cloud in strong non-circular motion.

When the stellar velocities are laid on top of an optical image, it is possible to physically see the areas in the galaxy that correspond to the observed stellar kinematics. Figure 5.1 shows a *Hubble Space Telescope* (*HST*[1]) V-band, [OIII]λ5007Å, Hβ and Hα filter composite image of NGC 1569[2] taken with the Advanced Camera for Surveys and the Wide Field Planetary Camera 2 instruments. The top panel shows the full *HST* image for reference. Several features in this image have been identified for reference in the analysis. The bottom panel shows the *HST* image in black and white greyscale with red and blue ovals on top of the picture representing

[1] *Hubble Space Telescope* (*HST*), is operated by NASA and ESA at the Space Telescope Science Institute (STScI). STScI is operated by the Association of the Universities for Research in Astronomy, Incorporated, under the NASA contract NAS 5-26555.

[2] Image Credit: NASA, ESA, the Hubble Heritage Team (STScI/AURA), and A. Aloisi (STScI/ESA)

the positions of the extracted spectra along the major axis. As discussed in Chapter 2.1.3.1, it was necessary to sum over a series of consecutive rows in the spectra in order to achieve adequate signal-to-noise for the cross-correlation procedure. Therefore, in Figure 5.1, the length of each oval corresponds to the spatial range of the slit that was summed, while the width of the ovals represents the $2\farcs5$ slit width. Red and blue ovals represent red-shifted and blue-shifted, respectively, $V_{\rm helio}$ radial velocities relative to the systemic velocity of NGC 1569. The green 'X' marks the center of the slit and the center of the galaxy.

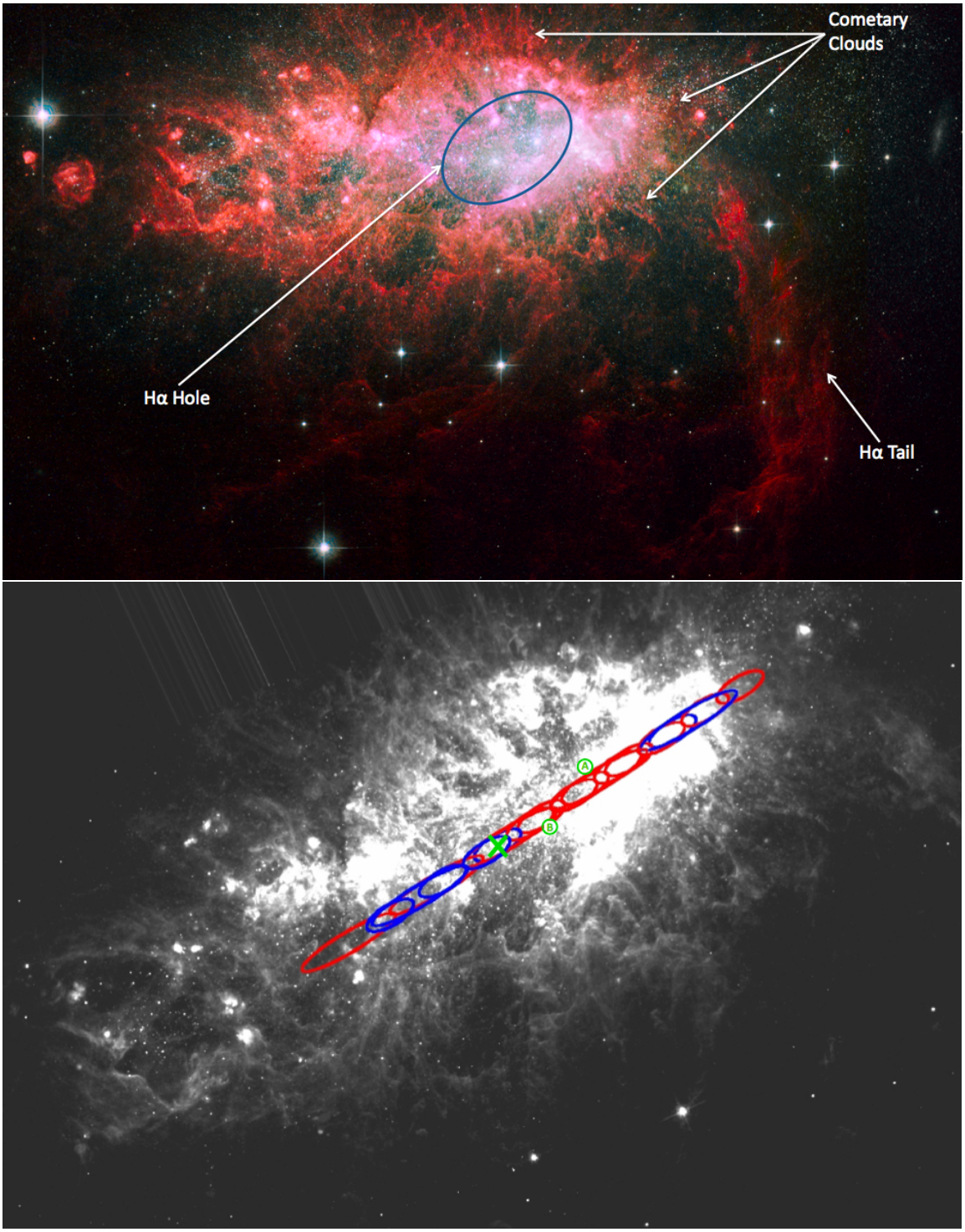

Figure 5.1 Top: *HST* composite image showing detailed Hα emission. Bottom: Same *HST* image only shown in greyscale with the major axis slit superposed. The ovals are the size and position of the extracted stellar spectra. The red ovals correspond to red-shifted velocities relative to the systemic velocity while blue ovals correspond to blue-shifted velocities. The green 'X' marks the center of the slit and the galaxy.

Overlaid on the bottom image of Figure 5.1 are the same red and blue ovals as in Figure 2.4. Each of the ovals plotted on top of the *HST* image are representative of independent data points from the integrated light spectra taken on different nights. Therefore, there are some red- and blue-shifted velocities, with respect to the systemic velocity, shown at the same positions. In the region west (right) of SSC A, the overall rotation of the stars is actually red-shifted, which is seen from the dominance of red ovals. The locations of the blue ovals that reside to the west of SSC A in the bottom image of Figure 5.1, correspond to a distance of -27″ from the galaxy center. If this location is compared with the velocity dispersion plot of the stars for the major axis PA (top left panel) in Figure 2.10, the velocity dispersions of the stars can be seen at -27″ to be larger by $\sim$10 km s^{-1} from the average stellar velocity dispersion. The velocity dispersion increase is the opposite of what is expected because 'typical' disk galaxies exhibit a *decreasing* stellar velocity dispersion with radius (Bottema 1993). The combination of integrated stellar velocity and velocity dispersion both being different from the overall motions of the stars is an indication that in this region, the stellar disk, composed mostly of young, luminous stars, of NGC 1569, is disturbed. Recall that the spectra are most sensitive to the young, luminous stars, which likely formed out of disturbed molecular gas clouds and carry the kinematic imprint of the parent gas.

In the optical *HST* image of NGC 1569, shown in the top panel of Figure 5.1, comet-like structures are observed extending to the northeast and southwest from the SSC region, as indicated by the arrows. Also, there is a large Hα hole where the SSCs reside, identified in Figure 5.1. The projected volume of this hole is estimated to

be about 500 pc^3 at the distance of NGC 1569. These features are likely evidence of blowout from mechanical energy input from the winds from the collection of massive stars in the SSCs. Figure 2.9 also shows a hole in the HI in all four PAs. It is centered around 0.′4 in the major axis PA and around 0.′1 in the remaining three PAs in Figure 2.9. This hole was identified and discussed by Israel & van Driel (1990). It is in this hole that the disturbed stellar kinematics, discussed above, are observed.

Next, the three-dimensional shape of NGC 1569 is explored using the kinematic measure, $V_{\rm max}/\sigma_{\rm z}$. For this relationship, the asymmetric drift corrected $V_{\rm max}$ from the HI analysis is used. The maximum velocity of the baryons that are responding to the total gravitational potential in the galaxy are needed, which means that the corrected rotation curve is required. An asymmetric drift corrected $V_{\rm max}$ of 50 $\pm$ 10 km s^{-1} is derived from the HI analysis, discussed in Chapter 4.3, and the average $< \sigma_{\rm z} >$ of 21 $\pm$ 4 km s^{-1} from the stellar kinematics, discussed in Chapter 2.1.4, are used. These values produce $V_{\rm max}/< \sigma_{\rm z} > = 2 \pm 2$, which is indicative of a thick disk. Perhaps, the disk is thicker in the region of SSC A than in the center of the galaxy because of the increase in integrated velocity dispersion of the stars and the decrease in integrated velocity of the stars in that region, as discussed above. But overall, the disk of NGC 1569 appears to be thick compared to spiral galaxies.

5.1.2 Morphology

Here, the HI morphology and velocity fields are compared with the deep Hα image of NGC 1569 and the *HST* image. Figure 5.2 shows, as contours, the integrated HI map. This image displays tenuous emission, detected for the first time, extending

to the south of the galaxy disk in a teardrop shape and to the northeast; black ovals outline this emission. Also identified in this image, are two features to the east labeled as 'Possible HI Companion' and 'HI Bridge'. These features refer to the work by Stil & Israel (1998, hereafter SI98) who used the Westerbork Synthesis Radio Telescope (WSRT) to obtain high-sensitivity maps of NGC 1569. They concluded that they had detected a low mass HI companion to NGC 1569. The maps detect this HI cloud, which can also be easily seen in Figures 3.2 and 3.3 at around $\alpha =$ 04:32:15, $\delta = +$64:49:00. The extended HI emission, circled in Figure 5.2, and the two features identified by SI98 may be related to one another and show evidence of a recent interaction or merger with NGC 1569. These claims are discussed further in Chapter 6 where the results from deep large-scale HI mapping around NGC 1569 and three of its nearest cosmological neighbors are described.

Figure 5.3 shows the *HST* image from the top panel of Figure 5.1 with contours of the integrated HI map overlaid so that comparisons with the morphologies can be made. What is interesting here is that there is an ultra-dense HI cloud to the west that lies at the edge of the optical galaxy in the same region where the disturbed stellar kinematics are observed. This HI cloud has a density of nearly 100 $M_{\odot}$ pc^{-2} above the surrounding medium, and, if there is hidden molecular gas, the column density could be much larger. Could this dense cloud have formed from the blowout? If one looks back to the *HST* image in the top panel of Figure 5.1 where the Hα comet structures are seen extending out from the Hα hole, it is evident that these structures extend in all directions. One would expect dense HI as a result of blowout to be concentrated in a ring-like structure around the Hα hole instead of piled up to

one side of the disk, as shown here. Thus, it is reasonable to conclude that this cloud is not the result of blowout from massive stars in the starburst and SSCs.

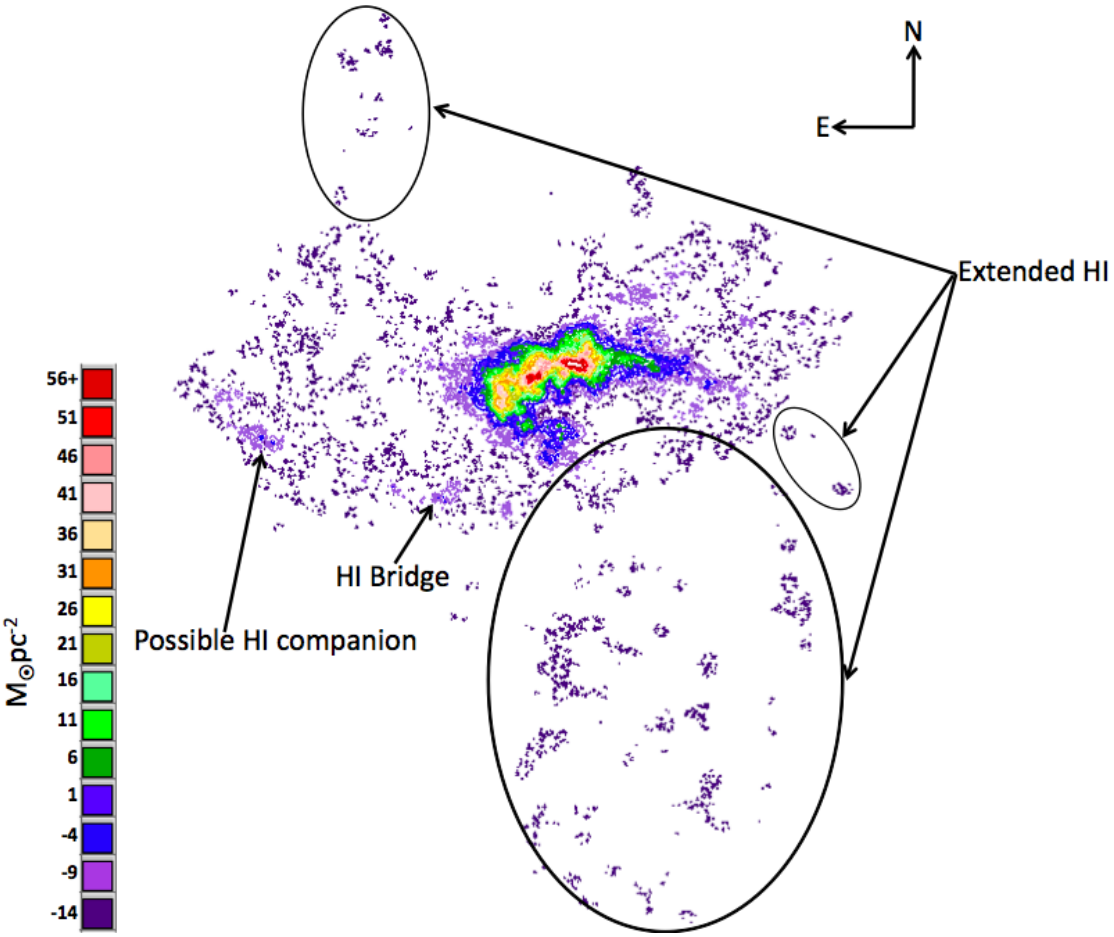

Figure 5.2 Integrated HI contour map showing the entire field. The extended emission features are circled and they are believed to be indicative of a possible interaction or merger. The HI "companion" and HI "bridge" identified by Stil & Israel (1998) are also identified.

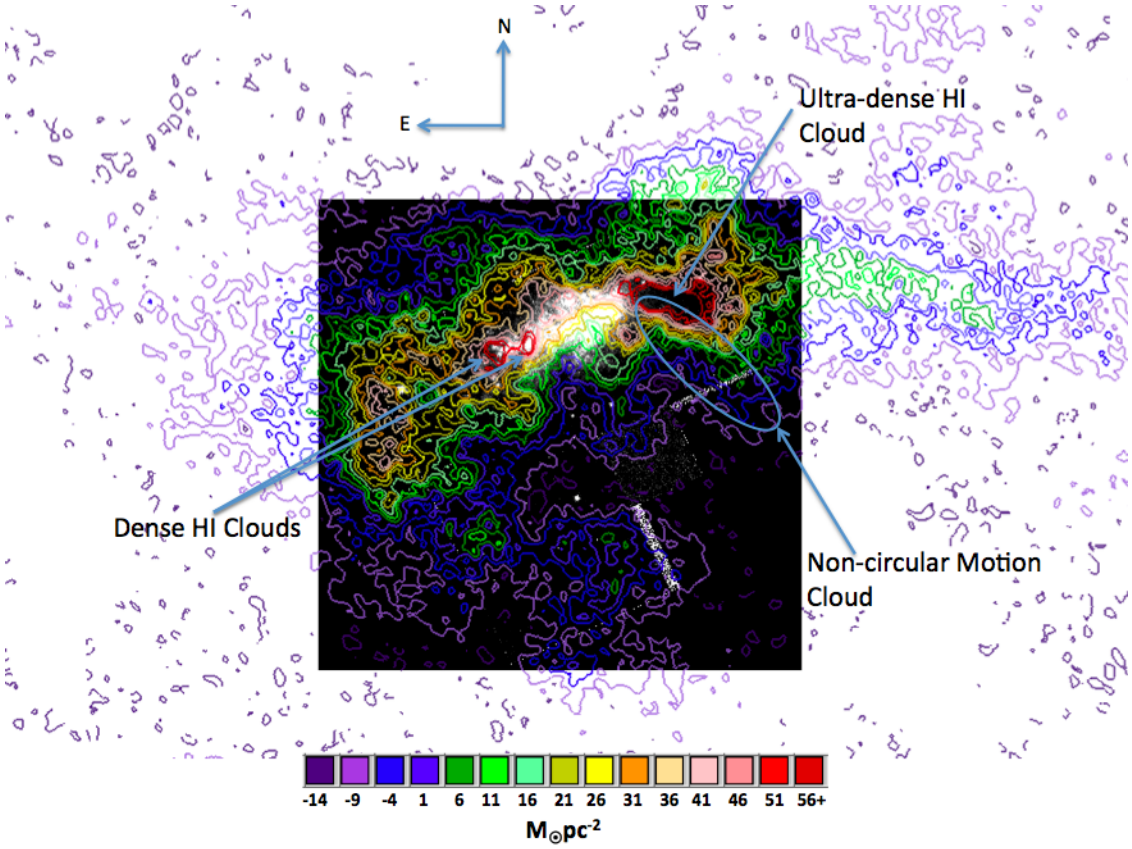

Figure 5.3 *HST* image with contours of the integrated HI map superposed. The ultra-dense HI cloud is identified as well as the two dense clouds on the opposite side of the optical galaxy. These features may have been at one time connected and extended through the current optical galaxy. The non-circular motion cloud, outlined by the blue oval, caused the dense HI gas to collapse into the starburst that ended nearly 20 million years ago.

In Figure 5.3, two smaller, dense HI clouds on the opposite side, east of the optical galaxy are also observed. The trigger for the starburst, as was previously noted in Chapter 3.2.2, could have come from the non-circular motion HI cloud, shown in Figure 3.6 and identified by the blue oval in Figure 5.3, by compressing the interstellar medium of NGC 1569. In this scenario, this cloud snowplowed into the HI gas in the dense region observed to the west of the optical galaxy, which initially created the ultra-dense HI cloud. The starburst was the result of the collapse of ultra-dense gas from this snowplowing effect.

Figure 5.4 is a magnified image of Figure 5.3 that shows SSCs A and B. It appears that, in general, the HI density is more concentrated to the north of the SSCs than it is to the south, as shown by the blue arrows and contour levels. There is a slight HI depression in the contour levels right above SSC A as indicated in Figure 5.4, possibly created in the blowout. Also marked on Figure 5.4 is the location and approximate size of two GMCs, as discussed in Chapter 4.3. These GMCs lie between the ultra-dense HI cloud and the SSCs and are at the top of the non-circular motion HI cloud. Figure 5.4 shows the optical *HST* image in greyscale and the northern tip of the GMCs contains a bright section of stellar light. The region between the ultra-dense HI cloud and the SSCs that contains the GMCs is the most probable area for the next generation of star formation.

When the deep Hα image with the integrated HI contours overlaid is observed, more streamer-like, arced Hα features, which trace HII regions, are seen toward the south than are in the north, as shown in Figure 5.5. The high density HI in the north and the visible Hα features in the south are the results of the projection effects from

the inclination of the galaxy. The projection of the thick disk of NGC 1569 inclined at 69° on the sky makes the southern half of the galaxy closer to Earth than the northern half, which is pointed away from Earth. Therefore, Hα emission can be seen in the southern region because there is less gas in the line-of-sight to absorb the light. Hα arcs and streamers extend nearly all the way through the HI disk in the southern direction of the disk. Similarly, the HI gas appears more dense in the northern half of the disk because there is more gas along the line-of-sight than there is in the southern half of NGC 1569.

Figure 5.5 also shows a strong Hα chimney to the north. The HI depression noted on Figure 5.5, shows the escape route for the Hα emission. Although the HI is more concentrated to the north, due to the projection effect of the inclined disk, the intense stellar winds from the starburst are able to penetrate all the way through the HI disk in the northern half of the galaxy, too. Tenuous Hα emission to the northeast of the optical galaxy stretches all the way through the HI disk just as it does in the southern part of the galaxy.

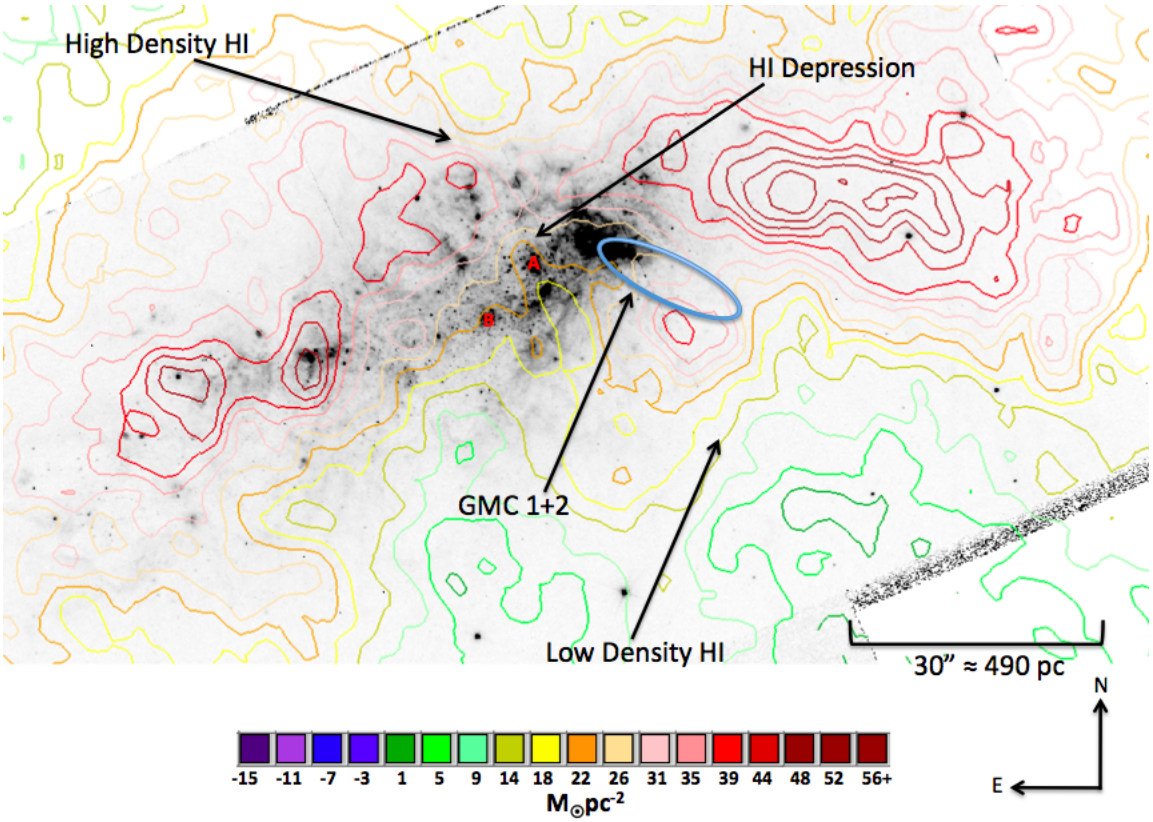

Figure 5.4 *HST* image is shown here with the SSCs A and B labeled and the integrated flux HI contours superposed. Here, the northern part of the galaxy contains more dense HI than the southern region. However, an HI depression directly over SSC A is seen, although this area is still more dense than the southern region.

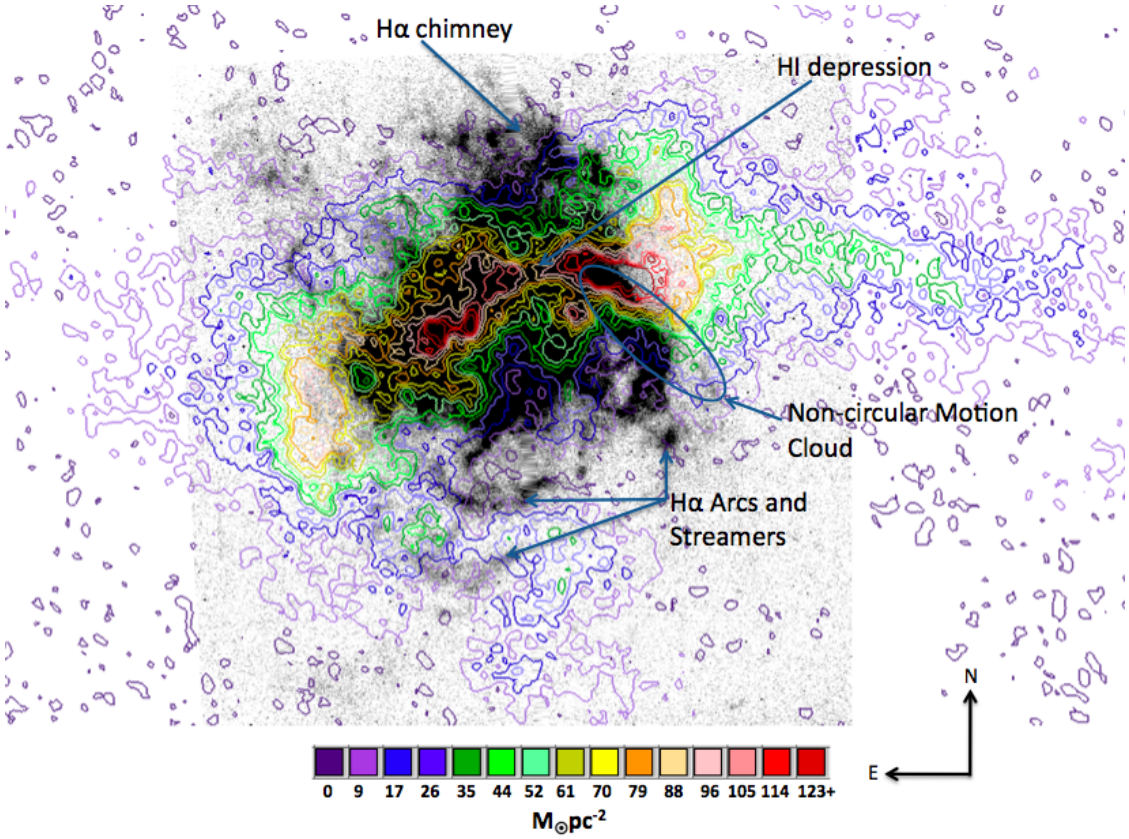

Figure 5.5 Deep Hα image with the integrated HI contours over plotted are shown. More Hα streamers and arcs can be seen to the south due to the lower HI density. To the north, a strong Hα chimney that extends all the way through the HI disk is observed.

The next things examined are the intensity weighted velocity contours overlaid on the Hα image. Figure 5.6 shows the full extent of the HI velocity contours with a low contrast Hα image underneath. In the region around the Hα image, a pseudo-"butterfly" shape in the HI is observed. The western wing of the "butterfly" has velocities that are blue-shifted relative to the systemic velocity, as seen by the blue and purple contours, while the eastern "butterfly" wing has red-shifted velocities, as seen by the orange and red contours. These features are identified in Figure 5.6. It is noted here that both the stellar and gas disks rotate in the same direction and they kinematically follow one another. Also, the location of the non-circular motion cloud from Figure 3.6 is indicated by the black oval in Figure 5.6. The velocity structure of this cloud appears different in Figure 5.6 than in Figure 3.6 because the entire intensity weighted velocity field is being shown in Figure 5.6 instead of just the deconvolved non-circular velocity structure. The 'Possible HI Companion' and 'HI Bridge' discussed by SI98 are identified in Figure 5.6. Both structures are seen as purple contours and do not follow the rotation of the rest of the galaxy. Again, it is surmised that these features are connected to the teardrop, tenuous emission that extends to the south.

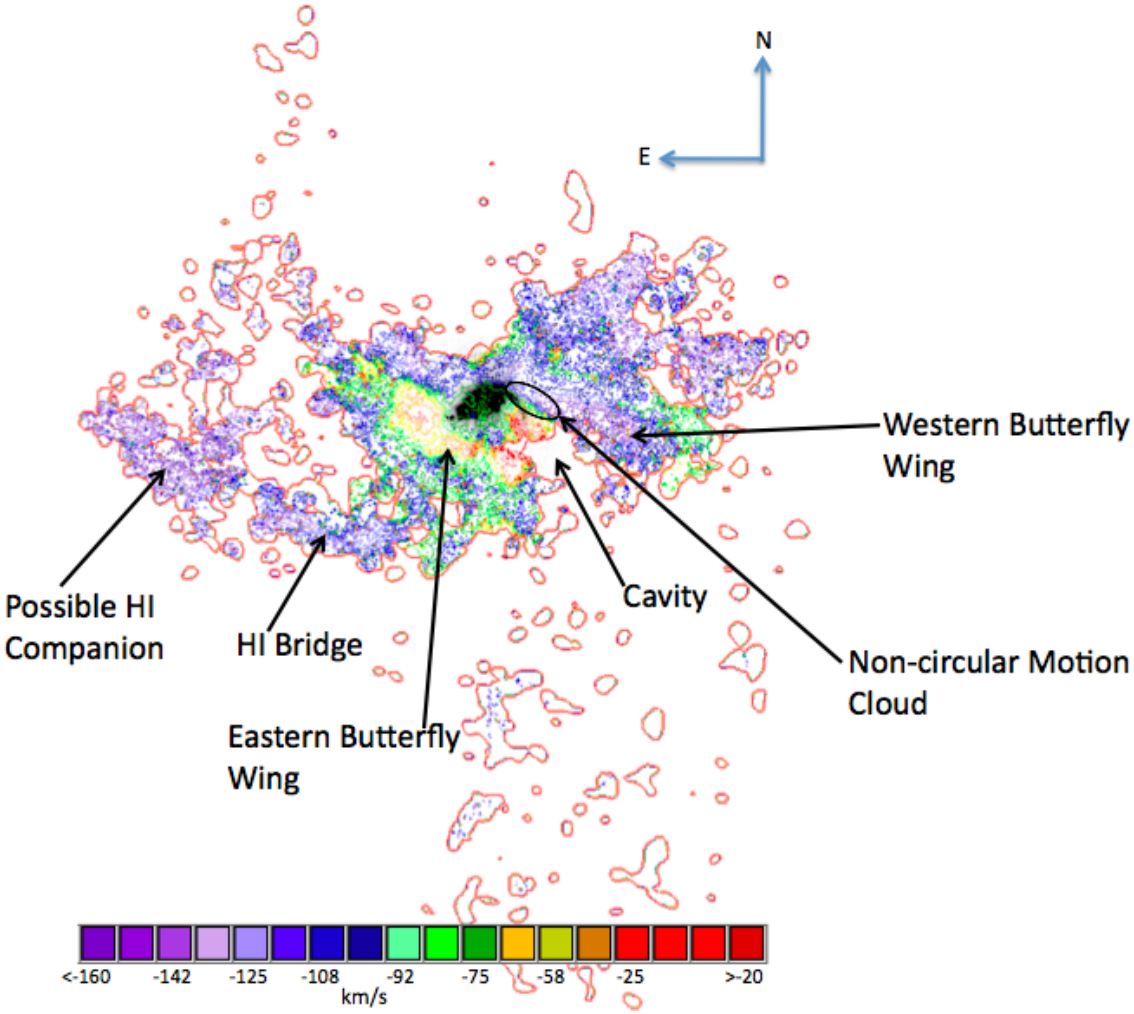

Figure 5.6 Intensity-weighted velocity contour map over plotted on the Hα image. The features identified by Stil & Israel (1998) are marked, as well as the position of the non-circular motion HI cloud shown in Figure 3.6. Two new features are shown here that make up what are called "butterfly wings" in this work. The cavity between the two wings matches the position of X-ray emission (Martin et al. 2002).

To the south of the Hα image in Figure 5.6, a cavity in the HI is seen. This cavity could have been carved out by ultraviolet photons, winds, and explosions from the massive stars in the starburst. Now, however X-ray emission fills in the cavity (Martin et al. 2002). Furthermore, in Figure 5.7, a version of Figure 5.6 that allows the central details to be seen, it is observed that the spectacular Hα tail that extends to the southwest of the optical galaxy is, in fact, the lit up edge of the non-circular motion HI cloud described above. The approximate size and location of the ultra-dense cloud is marked with a blue oval in Figure 5.7. Here, the velocity structure of the ultra-dense cloud is fairly constant, indicating that the cloud is relatively kinematically cool. Perhaps the dense HI region to the west of optical disk will be the location of the next star formation episode, although more information is needed to conclude this definitively.

Figure 5.8 shows the high contrast Hα image superposed with the HI velocity contours. Here, the arcs and streamers to the south line up with knots of turbulent HI: there are red and orange knots, representing low velocity HI, right next to purple and blue knots, which symbolize higher velocity HI. The Hα arcs lie across these features indicating that they are the lit up turbulent or comet-like HII gas.

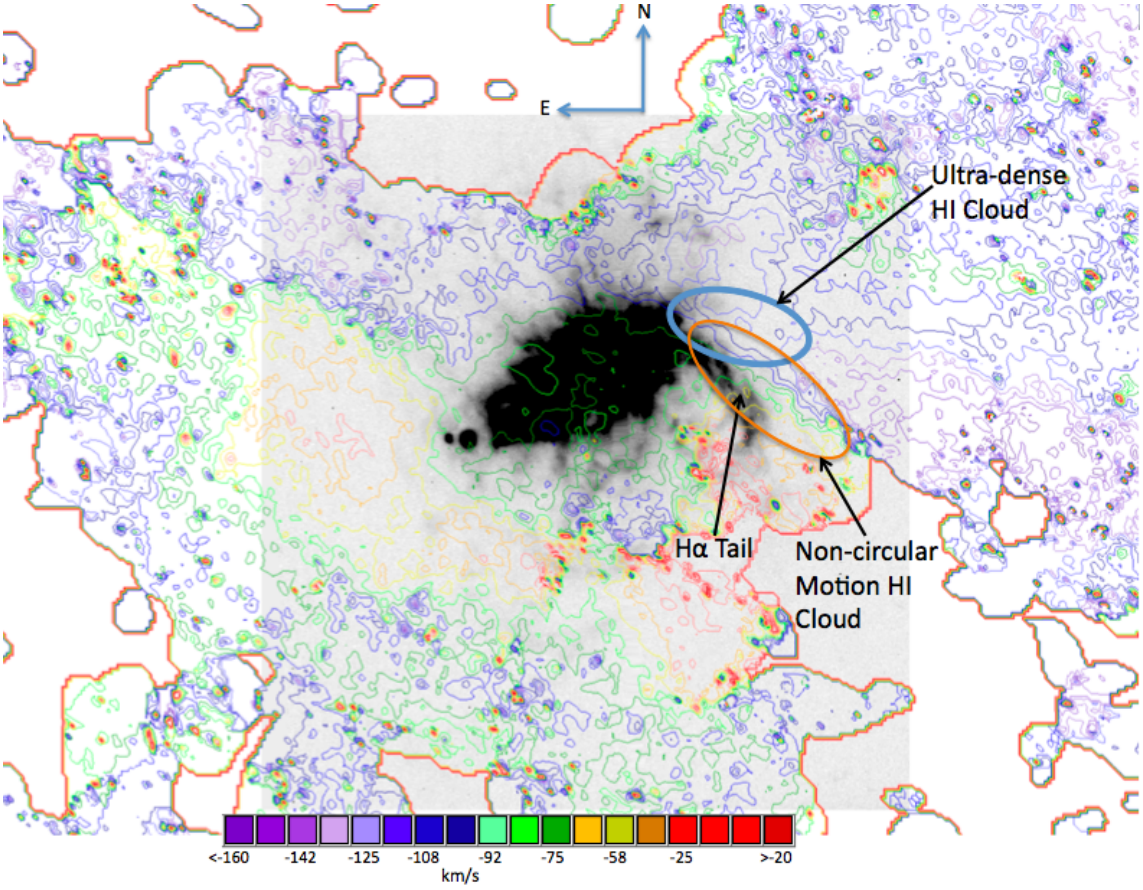

Figure 5.7 A zoomed in version of Figure 5.6 showing the Hα image again with the intensity weighted velocity contours plotted on top. The positions of the ultra-dense HI cloud as well as the non-circular motion HI cloud, are shown. The Hα tail is almost completely within the non-circular motion HI cloud. It is reasonable to conclude that this tail is the lit up edge of the non-circular motion HI cloud.

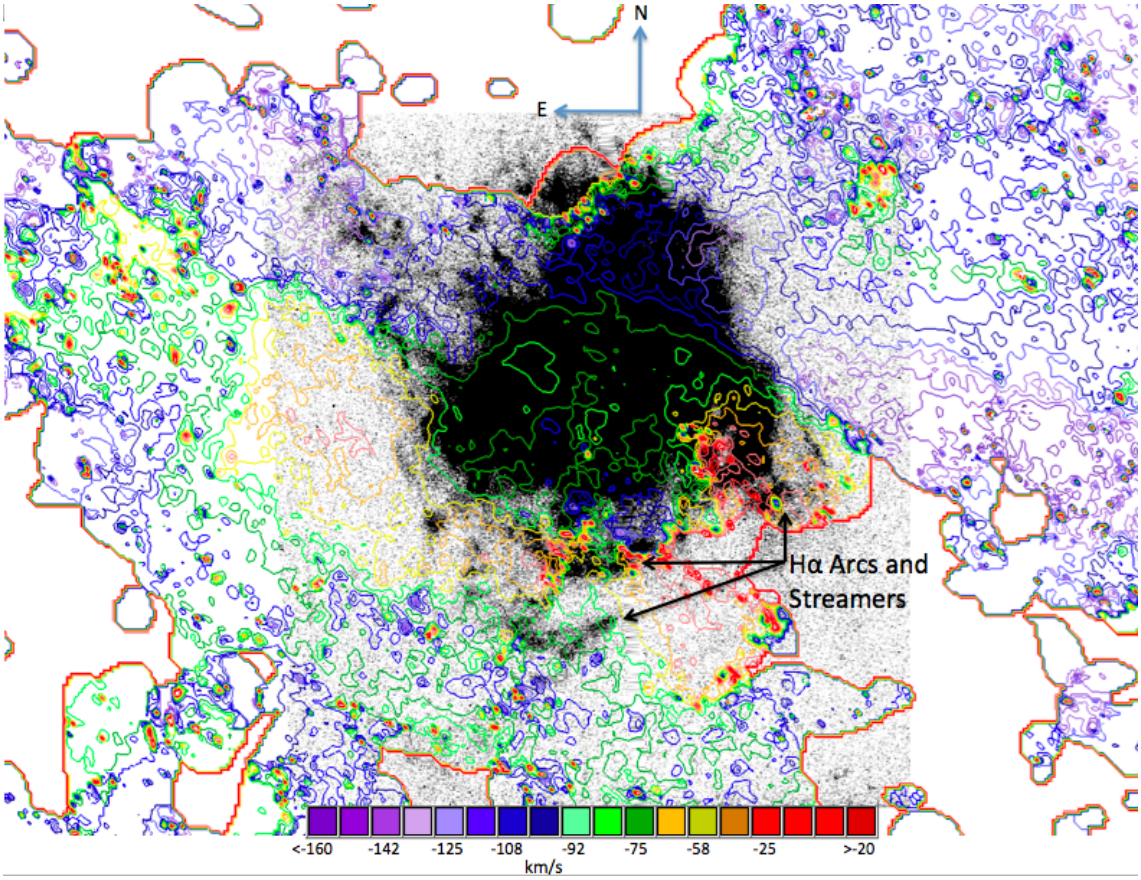

Figure 5.8 Same as Figure 5.7 but the Hα image is displayed with a high contrast so that the outlying Hα filaments can be seen. The Hα streamers and arcs in the southern part of the galaxy correspond with velocity knots of HI and, therefore, it is probable to conclude that these arcs and streamers are the lit up areas of turbulent HI.

5.2 Picture of a Galaxy in Transition

This dissertation presents an in depth analysis of the stellar and gas kinematics of the dIm post-starburst galaxy NGC 1569. The gas and stars kinematically follow each other. NGC 1569 also contains rotating HI and stellar disks, which became evident once the strong non-circular HI motions were successfully separated from the bulk rotation. A stellar velocity dispersion of $\sigma_z = 21 \pm 4$ km s^{-1} was determined, and the data show that NGC 1569 exhibits disk-like characteristics such as a kinematic measure, $V_{max}/\sigma_z = 2 \pm 2$. NGC 1569 is a thick disk and possibly thicker in the region of SSC A because of the observed increase in velocity dispersion of the stars in that region. The contributions of the stars and the gas to the gravitational potential of the galaxy were modeled. This shows that the stellar mass dominates the potential in the inner half of the HI disk, which is unusual in disk galaxies and dwarfs in particular.

The kinematics of NGC 1569 are complex. There is an HI cloud that participates in the strong non-circular motions that is likely responsible for the increase in stellar velocity dispersion in the region of the SSCs and for triggering the recent starburst. To the west of the SSCs lies a dense HI cloud that is believed to be a remnant of a dense ridge that now contains the SSCs. The strong non-circular motion HI cloud is striking the galaxy where the dense HI cloud and the stellar disk meet. Therefore, it appears that either the non-circular motion HI cloud hit the galaxy and snowplowed the gas into the dense HI ridge, or, the ridge was already there when the cloud hit the galaxy. Whichever was the case, this strong non-circular motion HI cloud probably created or impacted the dense HI ridge that stretched across what is now the stellar disk and by shocking this dense HI gas, caused the most recent starburst episode and

the formation of the SSCs. A "butterfly" shape is observed in the HI morphology, which is likely created from blowout.

There is extended HI emission surrounding NGC 1569, which could be indicative of a recent merger or interaction. The possible HI "companion" and HI "bridge" identified by SI98 are also observed in the data. The picture will become clearer in Chapter 6.

NGC 1569 fits into all six characteristics described by Dellenbusch et al. (2008), as discussed in Chapter 1.2, which makes it similar to other starburst "transition" dIm galaxies. It also has stellar velocity dispersions comparable to some dE galaxies, yet possesses disk characteristics. One would expect a transition dwarf to have attributes that fall between dIm and dE galaxies, which NGC 1569 seems to have. It is plausible, therefore, to conclude that NGC 1569 is evolving into something like a dE galaxy.

If NGC 1569 is in the process of forming from either a recent interaction or merger, then in some sense it is "young." The star formation history of NGC 1569 is complex; however, NGC 1569 has formed a large fraction of its stars within the last Gyr (Angeretti et al. 2005), which is why the stellar spectra are likely dominated by young, luminous stars. NGC 1569 may be a nearby example of how dwarf galaxies formed in the early universe. According to hierarchical cosmological simulations that utilize a flat universe dominated by ΛCDM, dwarf galaxies are the building blocks of larger galaxies (Bell et al. 2003; Cole et al. 2000). These simulations show mergers are the dominant mechanism for how spiral and elliptical galaxies form (Kravtsov 2010; Robertson et al. 2006; Steinmetz & Navarro 2002). If this is correct, then in the early universe there must have been a large population of transition objects as

small galaxies merged together to form larger systems. NGC 1569 could be a prime example of how dwarfs evolved in the early universe.

– 6 –

Getting the Big Picture with the GBT

6.1 Introduction

NGC 1569 is one of the nearest examples of a post-starburst dwarf irregular (dIm) galaxy, and it contains three supermassive star clusters (SSCs). The cause of the starburst, however, has not been fully understood. NGC 1569 was thought, up until recently, to be an isolated system in the projected direction of the IC 342 group of galaxies. It lies close to the Galactic plane and is highly obscured, which made an accurate distance determination using stellar color-magnitude diagrams difficult. But, in 2008, Grocholski et al. (2008) found the tip of the red giant branch using the *HST* and published a new distance of 3.36 Mpc placing NGC 1569 well within the IC 342 galaxy group. This opens up the possibility of interactions within the group, a natural way to produce a starburst and explain the observed chaotic kinematics of the stars and gas (but see Brosch et al. 2004).

Therefore, the National Radio Astronomy Observatory's (NRAO[1]) Robert C. Byrd Green Bank Telescope (GBT) was used in the spring of 2010 to map a large region around NGC 1569 in HI line emission. The purpose was to search for extended neutral hydrogen structures that would give evidence of tidal interactions between NGC 1569 and other IC 342 group members. The map includes four galaxies, NGC 1569, UGCA 92 (the nearest object to NGC 1569), IC 342 (the nearest large spiral galaxy to NGC 1569), and UGCA 86 (a dwarf galaxy close to IC 342 in the direc-

[1]The National Radio Astronomy Observatory is a facility of the National Science Foundation operated under cooperative agreement by Associated Universities, Inc.

Table 6.1. Global Parameters for Galaxies in GBT Map

Object	Type	M_V	V_{sys} (km s^{-1})	Distance (Mpc)	Center (l,b)	Ref
(1)	(2)	(3)	(4)	(5)	(6)	(7)
IC 342	SA(s)cd	-19.1	31	3.03	(138.°17, 10.°58)	1,3,8
NGC 1569	dIm	-18.2	-85.4	3.36	(143.°68, 11.°24)	2,4,6
UGCA 86	SAB(s)m	-15.5	72 ± 5	2.96	(139.°76, 10.°65)	1,5,7
UGCA 92	IBm	-13.2	-99	3.01	(144.°71, 10.°52)	1,3,7

Note. — Col. (1) Galaxy name; Col. (2) Galaxy type; Col. (3) Absolute V-band magnitude determined using distance modulus for distances in Col. 5 and total (apparent) V magnitude.; Col. (4) Systemic velocity of galaxy; Col. (5) Distance to galaxy; Col. (6) Galaxy center from NASA Extragalactic Database (NED); Col. (7) References for type and magnitude, systemic velocity, and distance.

References. — Type & Magnitude: (1) Buta & McCall 1999; (2) Hunter & Elmegreen 2006; Systemic Velocity: (3) NED; (4) This work; (5) Stil et al. 2005; Distance: (6) Grocholski et al. 2008; (7) Karachentsev et al. 2006; (8) Fingerhut et al. 2007

tion of NGC 1569). Figure 6.1 shows a map from Buta & McCall (1999) of the IC 342/Maffei galaxy group with the region mapped with the GBT outlined in black. Table 6.1 lists some of the global parameters of each galaxy. Here, the findings from nearly 85 hours of time on the GBT are presented.

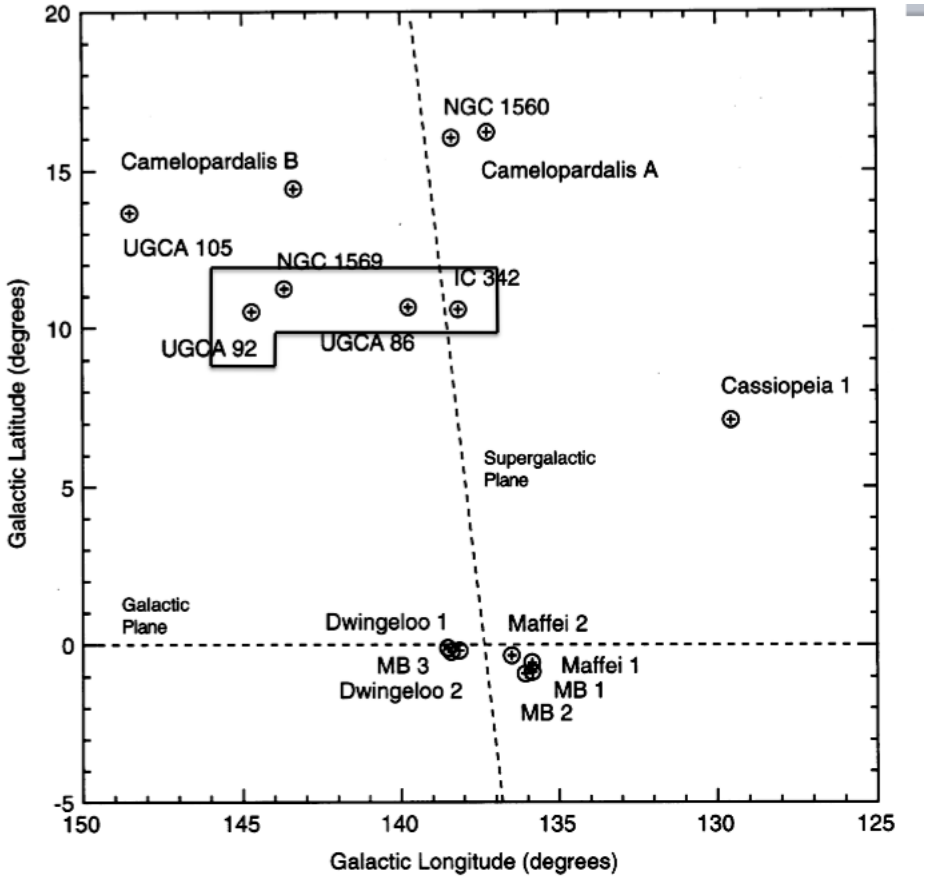

Figure 6.1 Map of IC 342/Maffei galaxy group from Buta & McCall (1999) showing the region mapped with the GBT outlined in black.

6.2 Observations and Data Reductions

The GBT data were collected over the course of four months, 2010 February – May. The observations were taken using the L-band receiver centered at 1.420 GHz using a bandwidth of 12.5 MHz and 16,384 spectral or frequency channels, producing a channel separation of 0.158 km s^{-1}. A beam size of 8.′8, a spatial resolution of 3.′3, and an HI sensitivity to a column density of $N_{\rm HI}$ = 5 x 10^{16} cm^{-2}, determined from 1σ in a channel free of emission, were also achieved. In order to observe the full 9° x 2° (l x b) region, the total area was divided up into four 2° x 2° squares and one 1° x 2° rectangle. Additionally, one 2° x 1° rectangle was added to map an area to the southeast of NGC 1569 to explore structure seen in the map. On-the-fly-mapping was used with a scan rate of 7′ min^{-1} with one minute integration times, and frequency switching was used to calibrate the data since the MW is very close to the galaxy in frequency making position switching ineffective for removal of background emission.

The data reductions were done in two main components. First, GBTIDL[2] was used to remove radio frequency interference, wavy baselines, and to trim the data. Also, GBTIDL was used to fit the baselines of the spectra by applying a second order polynomial. The data were smoothed to a velocity resolution and channel separation of 0.805 km s^{-1} using a boxcar function. The total number of channels was 1201 spanning a velocity range from -461.1 to 505.2 km s^{-1}.

The second component of the data reductions used the Astronomical Image Processing System (AIPS[3]). All of the data were combined together using the AIPS task

[2]Developed by the National Radio Astronomy Observatory; documentation at http://gbtidl.sourceforge.net

[3]The Astronomical Image Processing System (AIPS) has been developed by the NRAO; documentation at http://www.aoc.nrao.edu/aips

DBCON and the data were then gridded together using the task SDGRD to produce a map cube. After the data were gridded, they could be displayed as a single map with the full 9° x 2° region and 2° x 1° appendage.

6.3 Results

Figures 6.2, 6.3, and 6.4 show individual channel maps of parts of the data cube. The channel numbers are given in the upper right corner of each frame. The intensity scales used in the Figures, shown by the antenna temperature, $T_\star$, greyscale bar in degrees Kelvin at the top of each channel block, are constant in each figure but differ from figure to figure so that the interesting features highlighted in each can be easily seen. See Appendix B for a detailed explanation of the transformation from Jansky to Kelvin temperature. Figure 6.2 shows channels that contain extended HI features around NGC 1569. Each frame is one channel, 0.805 km s^{-1}, apart. The velocities in Figure 6.2 range from -117.19 km s^{-1} (channel 428) to -103.52 km s^{-1} (channel 445). NGC 1569 and UGCA 92 are marked in channel 428. The black arrow in channels 431 – 436 identifies a large, $\sim 0\overset{\circ}{.}5$ cloud that is likely associated with NGC 1569. The white arrows in channels 435 – 440, mark two long structures that resemble tidal features also probably associated with NGC 1569. The black arrows in channels 441 – 444 highlight possible HI emission associated with the tidal tails and NGC 1569. These features are discussed in Section 6.4.1.1. The white oval outlines the HI emission *not* associated with the MW warp and is discussed in Section 6.4.1.2.

Figure 6.3 shows the channels that contain MW emission and demonstrates the velocities where it becomes difficult to separate MW from extragalactic HI sources.

All of these channels record the emission between that of NGC 1569/UGCA 92 and IC 342/UGCA 86 in velocity. Every fifth channel is shown here for a velocity separation of 4.025 km s^{-1} between each frame. The corresponding velocities in Figure 6.3 range from -103.52 km s^{-1} (channel 445) to 13.20 km s^{-1} (channel 590).

Figure 6.4 shows the channels that contain IC 342 and UGCA 86. This figure is zoomed in so that UGCA 86 and IC 342 can be easily seen. IC 342 and UGCA 86 are both marked in channel 590. Every tenth channel is shown giving a velocity separation of 8.05 km s^{-1} between frames and the velocities range from 5.15 km s^{-1} (channel 580) to 190.46 km s^{-1} (channel 810). The black arrow in channels 670 - 770 identifies an HI spur feature coming out of UGCA 86 that is described by Stil et al. (2005). The intensity scale in Figure 6.4 was chosen so that the HI spur connected with UGCA 86 can be observed. Figure 6.5 shows three single channels that emphasize the HI spur as well as two newly discovered structures. One is a faint HI tail extending out from the southwest of UGCA 86 reaching toward IC 342, and the second structure is an even fainter HI tail extending out of IC 342 and reaching southeast toward UGCA 86. Both tails and HI spur are identified in the top panel of Figure 6.5 and are discussed in more detail in section 6.4.2.

Table 6.2. Average Column Densities and HI Masses for Identified Features

Object	Center Coords. (l, b)	Channel Range	Velocity Range (km s^{-1})	ΔV (km s^{-1})	$N_{\rm HI}$ (10^{18} cm^{-2})	$M_{\rm HI}$ (10^7 $M_\odot$)
(1)	(2)	(3)	(4)	(5)	(6)	(7)
			IC 342			
Galaxy	(138.°17, 10.°58)	–	–	–	–	–
Tail	(138.°26, 10.°24)	620 – 678	37.4 – 84.1	46.7	2.6	.99
			NGC 1569			
Galaxy	(143.°68, 11.°24)	362 – 482	-170.3 – -73.7	96.5	52	22
0.°5 Cloud	(143.°82, 11.°08)	431 – 436	-114.8 – -110.8	4.0	5.7	2.7
Tidal Tails	(144.°11, 10.°85)	435 – 444	-111.6 – -104.3	7.2	4.9	6.2
			UGCA 86			
Galaxy	(139.°76, 10.°65)	602 – 804	22.9 – 185.6	162.8	120	31
Spur	(139.°54, 10.°73)	656 – 763	66.6 – 152.6	86.2	14	2.1
Tail	(139.°72, 10.°27)	620 – 670	37.4 – 77.6	40.3	3.2	1.5
			UGCA 92			
Galaxy	(144.°71, 10.°52)	386 – 488	-151.0 – -68.9	82.1	76	14

Note. — Col. (1) Galaxy/Feature name; Col. (2) Galactic coordinates of the center of the galaxy/feature; Col. (3) Channel range over which the flux was integrated; Col. (4) Velocity range over which the flux was integrated; Col. (5) Total range in velocity over which the flux was integrated; Col. (6) Average HI column density of the galaxy/feature; Col. (7) Total HI mass, assuming distances from column 5 in Table 6.1

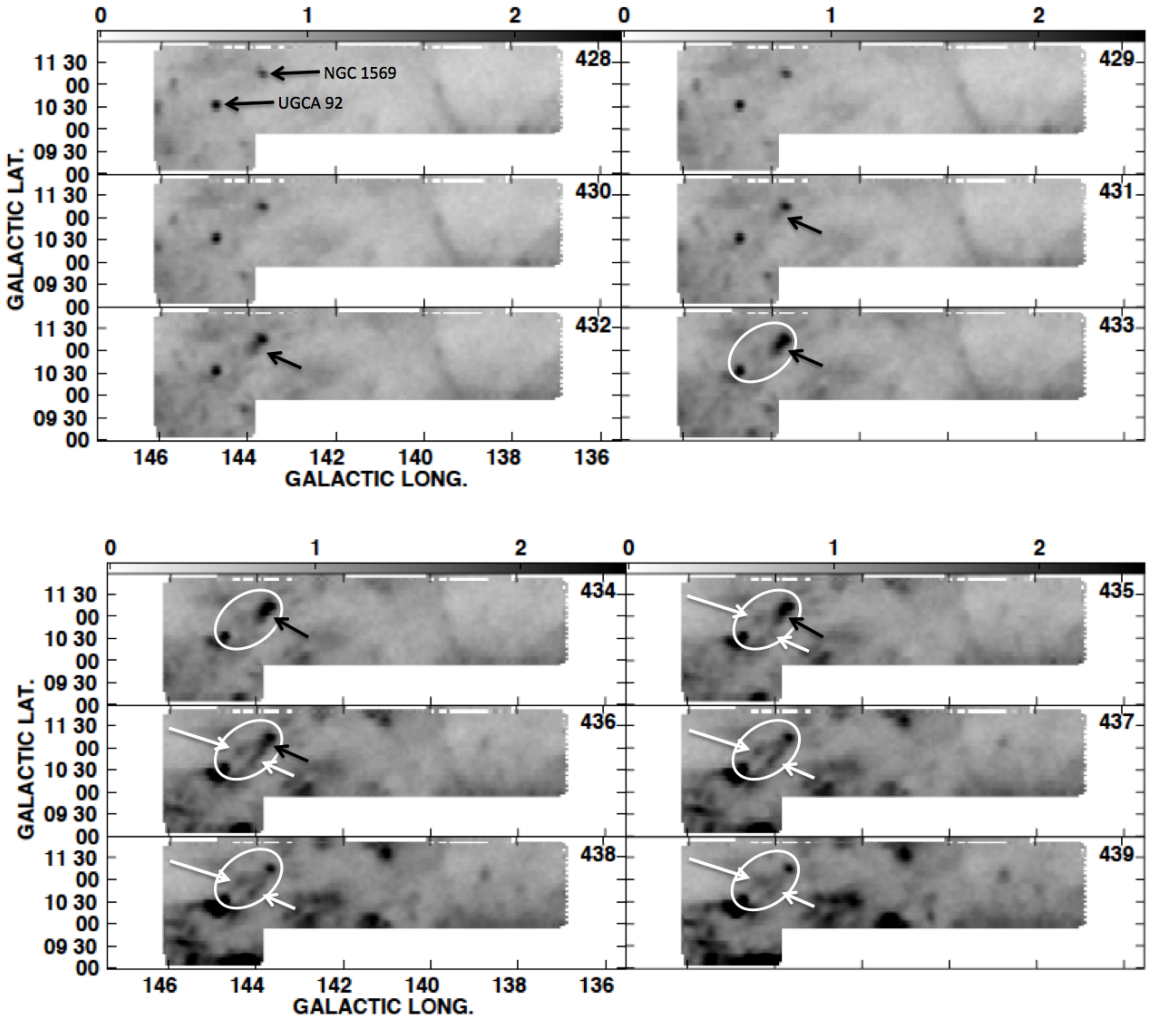

Figure 6.2 Individual channel maps showing NGC 1569 and UGCA 92, identified in channel 428. The channels are 0.805 km s^{-1} apart and range from -117.2 to -103.5 km s^{-1}. The black arrow in channels 431 – 436 indicate a 0.°5 HI cloud and tidal tail-like structures are identified by the white arrows in channels 435 – 440. The white oval in channels 433 – 445 outlines emission *not* associated with the MW or MW warp. The black arrow in channels 441 – 444 shows a knot of HI emission that my be associated with the tidal tail-like structures.

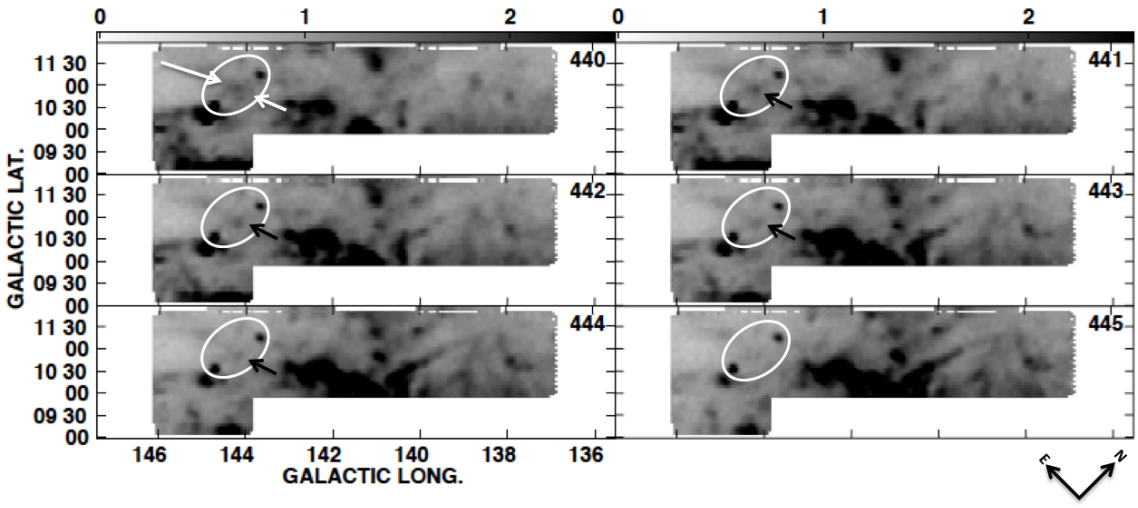

Figure 6.2 Continued

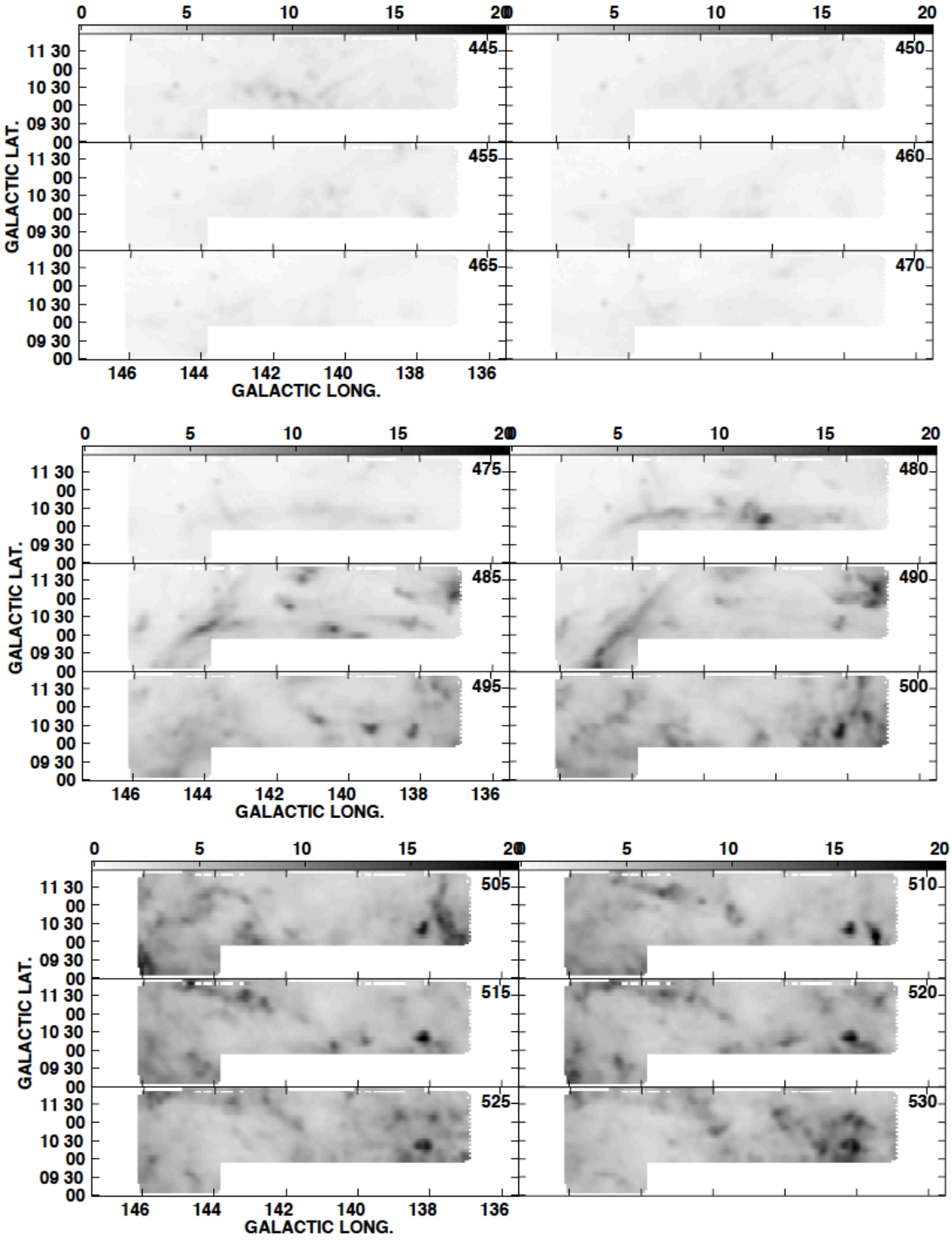

Figure 6.3 Individual channel maps showing MW emission. Each panel is about 4 km s^{-1} apart. These channels lie between the emission from NGC 1569/UGCA 92 and IC 342/UGCA 86 in velocity.

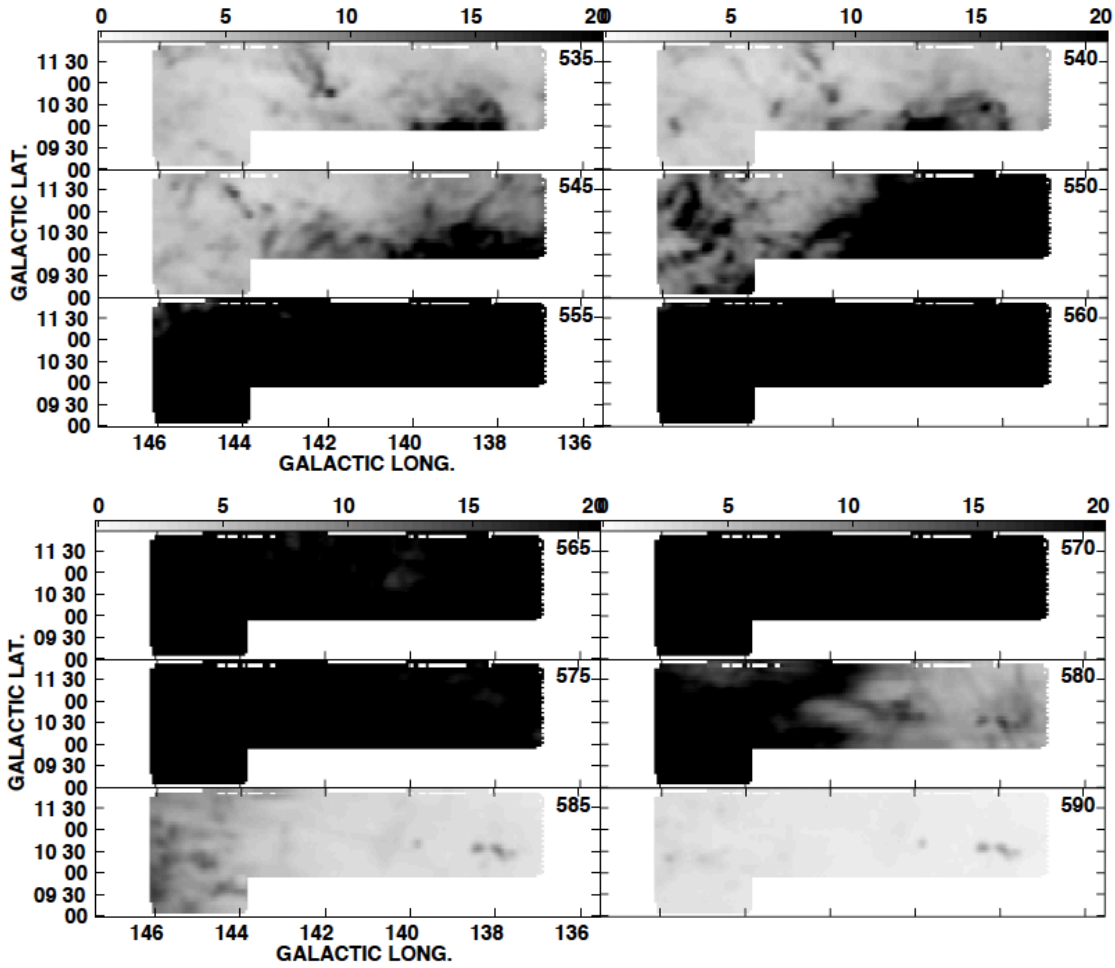

Figure 6.3 Continued

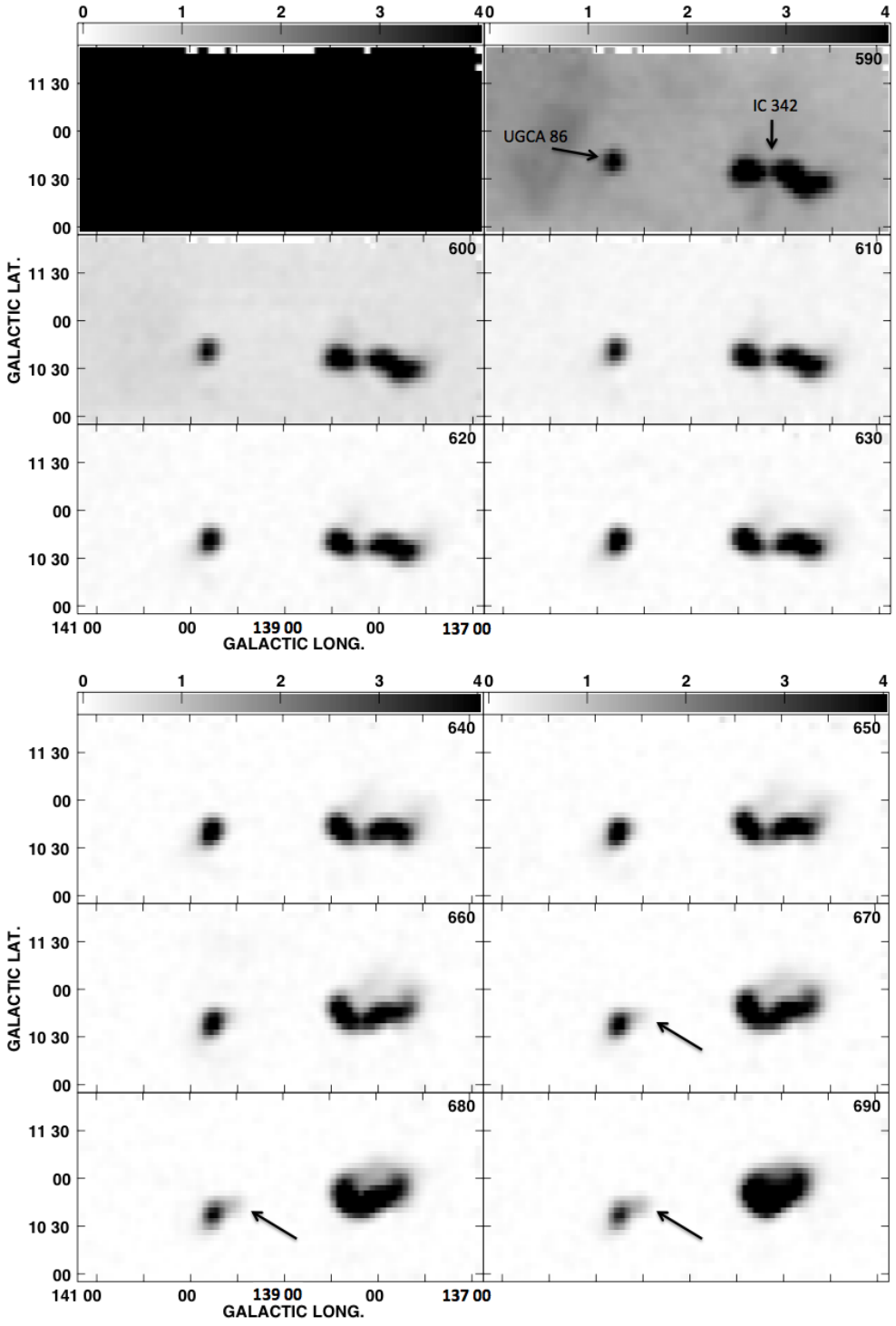

Figure 6.4 Single channel maps showing HI emission in the velocity range where flux is emitted by IC 342 and UGCA 86, which are marked for reference in channel 590. These channels are zoomed in so that detailed features can be easily seen, such as the HI spur associated with UGCA 86 identified with the black arrow in channels 670 – 770.

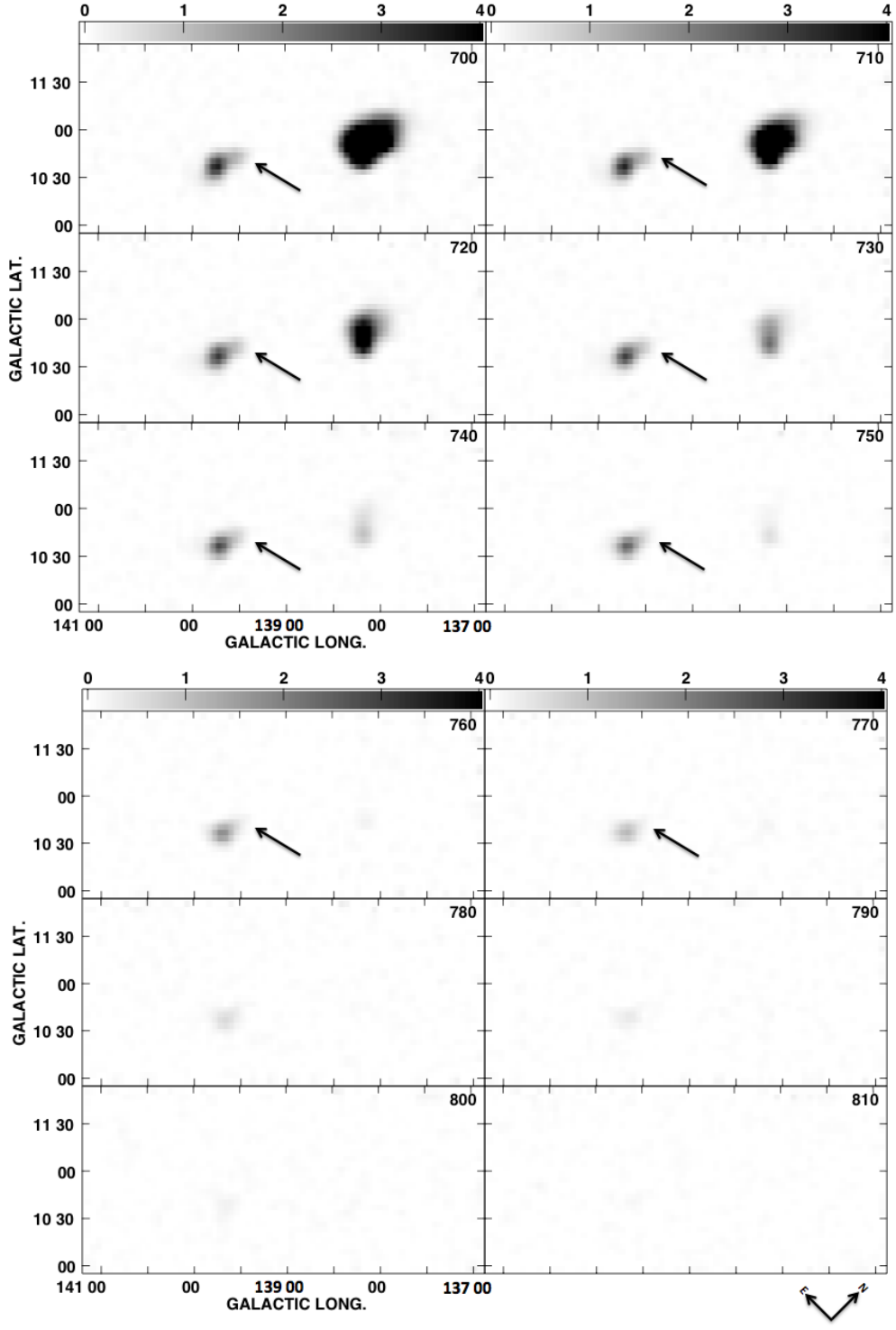

Figure 6.4 Continued

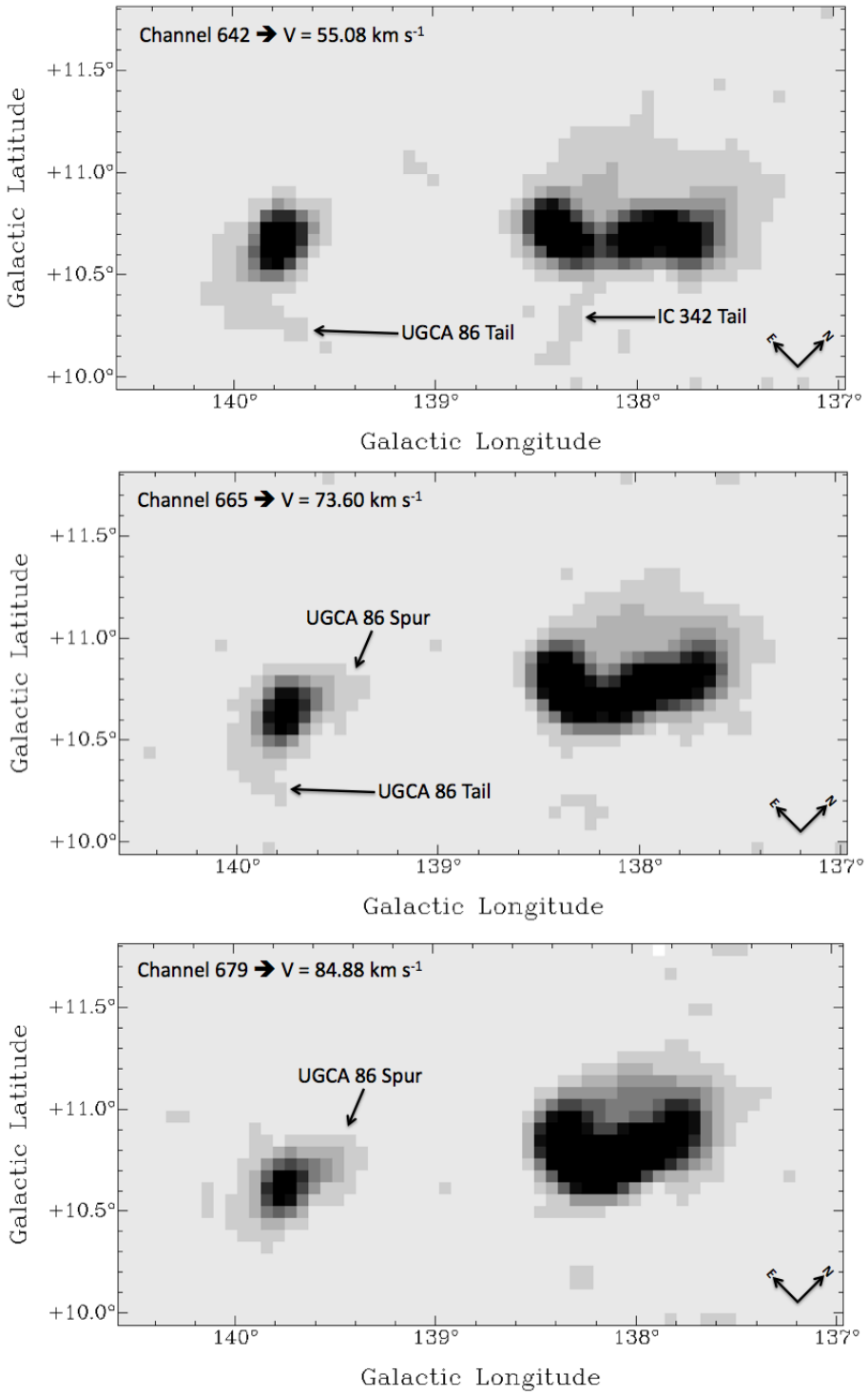

Figure 6.5 Three single channel maps showing HI tails in UGCA 86 and IC 342, respectively, as discovered with the GBT.

Table 6.2 lists average column densities and total HI masses for all the features described above. The AIPS task ISPEC was used to integrate rectangular regions of the map over consecutive channels in order to calculate the total antenna temperature $T_\star$ in degrees Kelvin of the features. These temperatures were then converted into average HI column densities and masses, see Appendix B for the derivation. The spiral galaxy IC 342 does not have a column density or HI mass because a large part of IC 342 is masked by the MW.

6.4 Analysis and Discussion

The purpose of these observations is to see if there is extended HI structures connecting NGC 1569 to members of the IC 342 galaxy group. At the sensitivity limit, no extended HI structures connecting IC 342 or UGCA 86 to NGC 1569 were detected. However, MW emission lies between NGC 1569 and IC 342/UGCA 86 in velocity, so, there could be tenuous structures connecting these objects that are masked by the MW. However, other interesting features were discovered. The data are analyzed in two parts, first NGC 1569 and UGCA 92 are discussed, and second, IC 342 and UGCA 86 are examined.

6.4.1 NGC 1569 and UGCA 92

6.4.1.1 Extended HI features

Two distinct structures were detected that appear to be connected to NGC 1569. The first is a large, $0\overset{\circ}{.}5$ HI cloud, which at the distance of NGC 1569 is about 29 kpc in diameter, sitting directly over NGC 1569. Here, "over" is defined as sharing the

same position and velocities as NGC 1569 but no assumption is made about whether the cloud is physically in front of or behind the galaxy. The cloud is elongated and extends south toward UGCA 92. It is only visible in ∼6 channels, 431 – 436 in Figure 6.2 , giving it a velocity width of only ∼4 km s^{-1}.

Figure 6.6 shows channel 433, velocity = -113.17 km s^{-1}, which shows the prominent emission of the 0.°5 HI cloud. The black contours visible in Figure 6.6 are of the high resolution VLA integrated HI map of NGC 1569 (see Figure 3.2). They are over plotted on the GBT map for identification and to show the morphology of the dIm galaxy. The VLA was able to resolve the strongest emission of the large HI cloud, as seen by the faint black contours extending to the south over the cloud (seen in yellow).

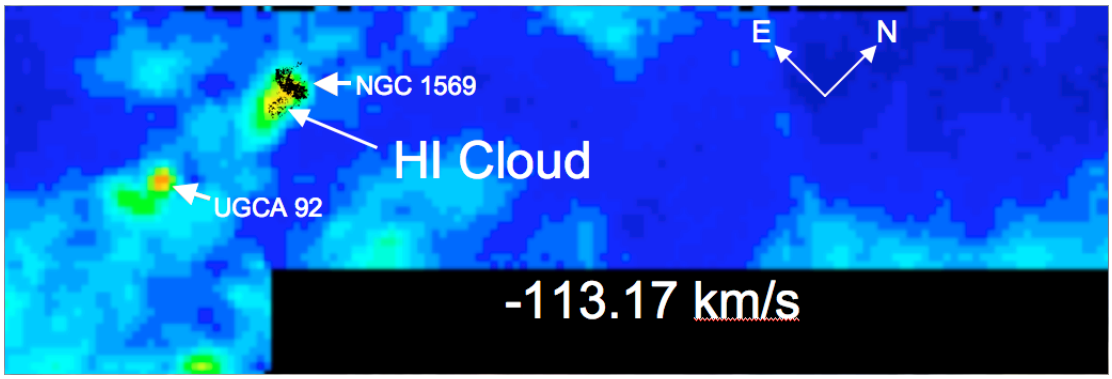

Figure 6.6 Individual GBT channel map showing the strongest emission from the large, cold HI cloud over NGC 1569 extending southeast about 0.5° toward UGCA 92. Black contours are from integrated HI map from the VLA data for NGC 1569.

From the GBT data presented here, a total HI mass for NGC 1569 of 2.2 x $10^8 M_\odot$ was derived assuming a distance of 3.36 Mpc, as shown in Table 6.2. This HI mass agrees very well with the HI mass of 2.3 x $10^8 M_\odot$ determined from VLA data from Chapter 4.3 and the HI mass of 2 x $10^8 M_\odot$ derived by Mühle et al. (2005), corrected for distance, as well as the HI mass of 3 x $10^8 M_\odot$, again, corrected for distance, determined by Stil & Israel (2002). For the 0.°5 HI cloud alone, an average column density of 5.7 x 10^{18} cm^{-2} and a mass of 2.7 x $10^7 M_\odot$ were also calculated. This mass is approximately 11% of the total HI mass in NGC 1569.

The second features discovered are two tidal tail-like structures extending out from NGC 1569 in the direction of UGCA 92. The tidal tails appear to be about 1.°5 long, stretching nearly the entire projected distance to UGCA 92. At the distance of NGC 1569, this is about 88 kpc in length projected on the sky. Figure 6.7 shows channel 436 where the tidal tail features are obvious. These tails appear at more positive (red-shifted) velocities than the 0.°5 cloud. An angle of $\sim 27^\circ$ between the two tails, projected on the sky, was measured. The tail structures are only visible in 6 channels and therefore have the same velocity width of $\sim$4 km s^{-1} as the 0.°5 HI cloud. There is a knot of HI emission that lingers at higher velocities than the tidal tail structures (in channels 441 – 444), as identified in Figure 6.2 . It is not clear if this emission is part of the tidal tails or not.

Table 6.2 shows the average column density (4.9 x 10^{18} cm^{-2}) and mass (6.2 x $10^7 M_\odot$) of the tidal tails, where the knot of HI emission in channels 441 – 444 is included. A total combined mass for both the 0.°5 HI cloud and the tidal tails is 8.5 x $10^7 M_\odot$. This mass is slightly less than what one would get by simply adding

the two masses in Table 6.2 together because of the overlapping channels, 435 and 436, between the 0.°5 HI cloud and the tidal tails. When compared to the total HI mass of NGC 1569, as determined from the GBT data, the combined mass for the two features is roughly 40% of the galaxy. NGC 1569 was separated from the 0.°5 HI cloud and tidal tail-like structures in position only, which means that there may be some emission from the 0.°5 HI cloud mixed with NGC 1569, therefore, making the mass estimate of NGC 1569 an upper limit, although the mass does agree with previous work. Then, the channels were integrated where emission from each object, the 0.°5 HI cloud, tidal tail-like structures, and galaxy, could be seen without interference from MW or MW warp, to obtain the masses.

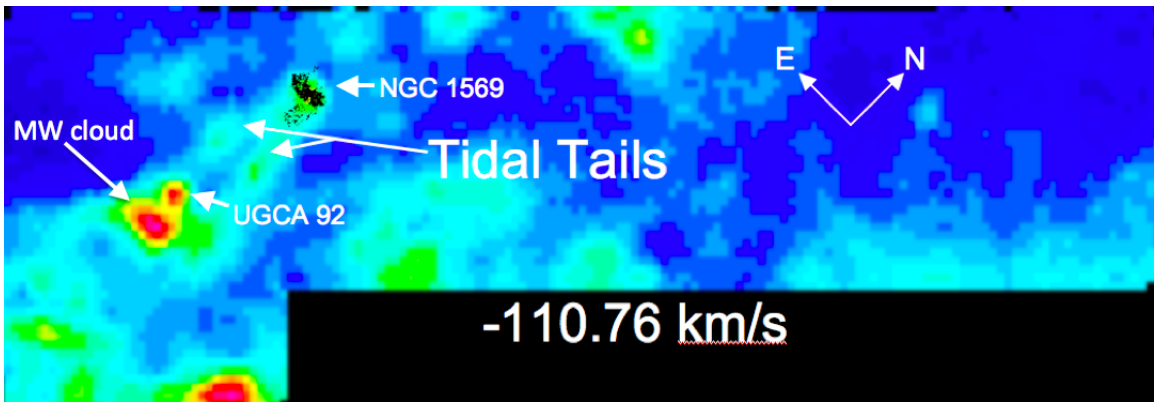

Figure 6.7 Individual GBT channel map showing the strongest emission from the HI tidal tails extending southeast from NGC 1569 toward UGCA 92. Black contours are from integrated HI flux map of VLA data for NGC 1569.

6.4.1.2 Milky Way versus Extragalactic HI Emission

It is well known that NGC 1569 shares the same HI velocities as the MW (e.g., Reakes 1980; Israel & van Driel 1990; Stil & Israel 2002; Mühle et al. 2005), specifically between -20 to +20 km s^{-1}, as seen in Figure 6.3 (channel 550 $\approx$ -19 km s^{-1} to

channel 585 ≈ 10 km s^{-1}). At velocities less than -20 km s^{-1}, the MW is still present, although not as strong (see left panel of Figure 6.8, velocities from -80 to -20 km s^{-1}). However, at velocities from -120 to -100 km s^{-1}, the MW warp is present at the position of NGC 1569 and UGCA 92 (Felix J. Lockman, private communication).

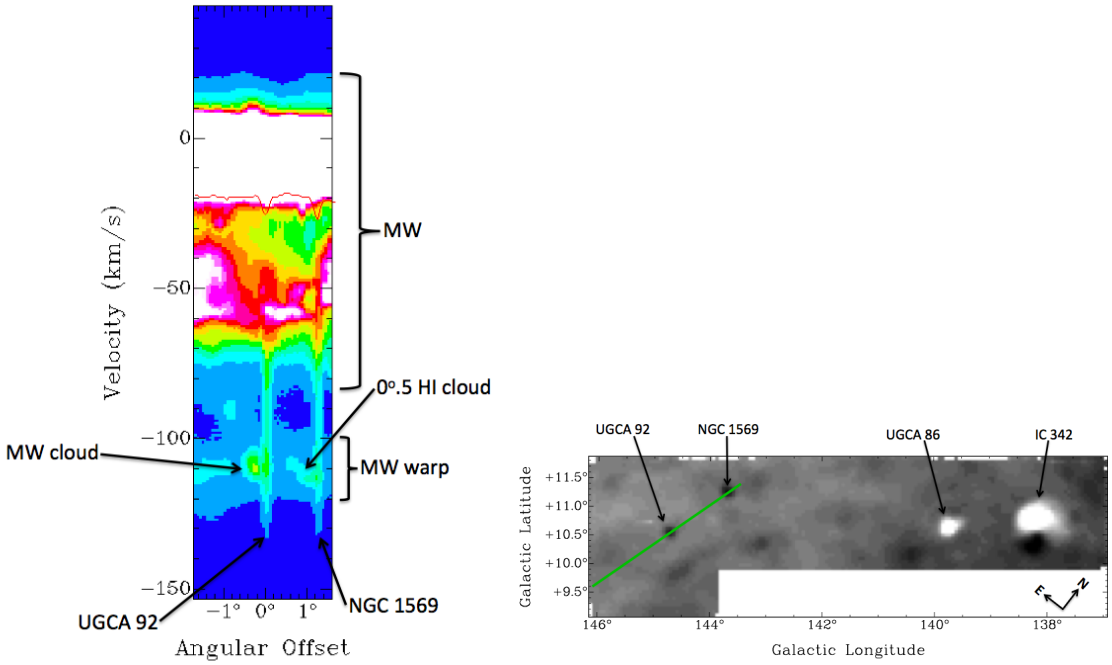

Figure 6.8 Left: P-V diagram along the green line shown in the right panel that slices through NGC 1569 and UGCA 92. The angular offset of 0° corresponds to the center of UGCA 92. Positive direction is north, toward NGC 1569 and negative direction is south. NGC 1569 and UGCA 92 are marked as well as the 0°.5 HI cloud and the MW cloud that resides to the south of UGCA 92. Right: Intensity-weighted velocity map of the entire data cube. Black implies negative velocities and white shows positive velocities. The green line corresponds to the position of the slice used to create the P-V diagram in the left panel. The four galaxies are marked for reference as well as north and east.

The left panel of Figure 6.8 shows a position-velocity (P-V) diagram sliced through the data cube along the green line shown in the full, intensity-weighted velocity map (right panel). The 0° angular offset on the x-axis in the left panel coincides with the center of UGCA 92. The 0.°5 HI cloud is marked in the diagram as well as the MW cloud, shown in Figure 6.7, that resides just south of UGCA 92. Also marked in the left panel of Figure 6.8, is the MW and MW warp velocity ranges. Both NGC 1569 and UGCA 92 have velocities that overlap with the MW and MW warp, as evidenced by the vertical light blue-green features that stretch upwards into the MW emission where the velocities become more positive. However, the MW warp at these velocities and positions is tenuous, as seen by the low flux of the MW warp region marked in Figure 6.8, and the MW is significantly offset in velocity from the 0.°5 HI cloud and tidal tail features.

The systemic velocity of UGCA 92 is -99 km s^{-1}, as shown in Table 6.1, which coincides with the upper limit of the MW warp velocity range. NGC 1569 has a systemic velocity of -85.6 km s^{-1}, which is between the peak MW and MW warp velocities, although it is likely that some form of MW emission exists at this velocity also. Since both NGC 1569 and UGCA 92 have velocities in the range of the MW and the MW warp, one would expect any extended HI features associated with either of these galaxies to also have velocities confused with the MW. So, how can one tell which features are MW and which are associated with NGC 1569 and/or UGCA 92?

One way to approach this problem is to look at the line profiles of different HI features in the area around NGC 1569 and UGCA 92. Figure 6.9 shows five line profiles at the velocities of the extended HI features in question, plotted on the same

temperature scale (y-axis). The (l, b) positions of the five line profiles are given in the upper left corner of the plots and are shown in Figure 6.9(f). The 0.°5 HI cloud shows a line profile that is narrower and has a lower intensity than the two MW clouds in Figures 6.9(b) and (c). Also, the wings of the line are broader than the MW clouds' line profiles. The MW cloud feature in Figure 6.9(b), is a Gaussian profile with a peak intensity at around 4.5 K, compared to a peak intensity of only 2.7 K for the 0.°5 HI cloud in (a). Figure 6.9(c) shows a line profile of a MW cloud located at the bottom of the GBT map. This profile shows the cloud peak intensity is 4.2 K and the line profile is much broader compared to the 0.°5 HI cloud in (a). The width of the line profiles for the three clouds can also be seen in Figure 6.2 . The 0.°5 HI cloud is observed in only 6 channels ($\Delta V \sim 4$ km s^{-1}) while the MW cloud directly below UGCA 92 and the MW cloud at the bottom of the map are seen in about 16 channels total ($\Delta V \sim 12$ km s^{-1}), including four channels beyond what is shown in Figure 6.2 .

Also, both MW cloud line profiles are slightly red-shifted compared to the 0.°5 HI cloud. This shift in velocity is also seen in Figure 6.2 . Both MW clouds have the same velocity range; they both appear in channel 434 and disappear in channel 449, which is beyond Figure 6.2 . The 0.°5 HI cloud is slightly blue-shifted compared to both of these MW clouds, as Figure 6.2 shows it first appearing in channel 431, compared to 434 for the MW clouds. Although this is only a $\sim$2.5 km s^{-1} shift, it is also seen that the peaks of the line profiles for these MW clouds in Figure 6.9 are offset by about 3 km s^{-1} from the 0.°5 HI cloud, in agreement with Figure 6.2 .

Profiles of the centers of NGC 1569 and UGCA 92 are also plotted in Figures 6.9(d) and (e), respectively. These line profiles are very broad, as expected for rotating galaxies, but NGC 1569 shows a very narrow component at the peak of the flux. This narrow peak corresponds with the peak velocity of the 0.°5 HI cloud. It appears that the 0.°5 HI cloud overlaps with NGC 1569 in both position and velocity. In the previous work, the VLA observations show high velocity HI surrounding the galaxy as well as tenuous emission to the south and north. All of this HI emission detected by the VLA, matches the velocities of the 0.°5 HI cloud in the GBT map. Perhaps the 0.°5 HI cloud is what is being detected by these high velocity HI features seen surrounding NGC 1569 in the VLA data.

The tidal tail-like features need a different analysis, as they are elongated features without a central core of concentrated HI emission. Beginning with Figure 6.2, the tidal tail features are observed in only about six channels, the same as the 0.°5 HI cloud. Also, there are no other features like these tidal tails in any of the frames in Figure 6.2 . Tenuous wisps are seen throughout Figure 6.2 but, none match the distinctive v-shape that the tidal tail features exhibit. Furthermore, the other wisps and filament-like structures seen in Figure 6.2 are displayed in more than just six channels and are much longer in length, such as the tenuous, nearly vertical wisp in channels 428 – 437 at $l \approx 139° - 140°$. Figure 6.3 shows the channels where the MW emission is strongest and again, no tidal tail features like those extending out from NGC 1569 in Figure 6.2 are observed.

As for other structures, such as high velocity clouds (HVCs) around the MW, that may be contaminating the field, the only likely candidate is HVC Complex H.

However, according to an HI map of HVC Complex H by Wakker et al. (1998), the HVC does not overlap with NGC 1569 or UGCA 92 in position or velocity. There are no other HVCs in the vicinity of NGC 1569 that match the position or velocity.

Although it is impossible to say definitively that the 0.°5 HI cloud and tidal tail-like features are not part of the MW, MW warp, or any HVC associated with the MW, the evidence (blue-shifted velocity, narrow width, and wide wings of the line-profile of the 0.°5 HI cloud compared with other nearby MW clouds, and the distinctive v-shape of the tail features) suggests that these features are extragalactic in nature. In Section 6.5, the discussion will be based on the assumption that these HI features are extragalactic and associated with NGC 1569.

6.4.2 IC 342 and UGCA 86

As previously stated, MW HI emission lies between NGC 1569/UGCA 92 and IC 342/UGCA 86 in velocity and, in fact, nearly half of IC 342's rotating disk is masked by the MW, as seen in Figures 6.3 and 6.4. Figure 6.10 shows a P-V diagram, similar to the one in Figure 6.8 but instead, slicing through the centers of UGCA 86 and IC 342. There is a double peaked emission feature through the center of IC 342 due to a lack of HI in the center of the galaxy where the gas is presumably mostly molecular gas, which is commonly observed in spiral disks (Leroy et al. 2008). This can also be seen in the channel maps in Figure 6.4 from channels 590 – 650 where the center of IC 342 shows a depression in emission.

In addition to the P-V diagram, line profiles were made through the centers of UGCA 86 and IC 342, as shown in Figure 6.11. These profiles show the extent of

the MW at velocities below 0 km s^{-1} and show that IC 342 and UGCA 86 are well separated from MW confusion above 0 km s^{-1}. Also, there are no HVCs known that match the positions and velocities of IC 342 and UGCA 86. Therefore, it is assumed that all HI emission above 0 km s^{-1} is associated with IC 342 and UGCA 86.

From these GBT data, an HI tail extending from the south to the west from UGCA 86 was detected. Stil et al. (2005) identified an HI spur to the north of the galaxy in their high resolution HI data taken with the Dominion Radio Astrophysical Observatory (DRAO) Synthesis Telescope. They argued that the spur came from an interaction with IC 342, although this was difficult to prove partly because no counter tail was observed in their data. Figure 6.5 shows three individual channel maps at low signal-to-noise for the purpose of displaying the counter tail to the HI spur in UGCA 86. This counter HI tail is very tenuous with an average column density of only 3.2 x 10^{18} cm^{-2} and a mass of only 1.5 x $10^7 M_\odot$. Also, the HI tail is observed in 51 channels total from channel 620 – 670, giving a velocity range of 37 – 78 km s^{-1}. The HI tail is about $36'$ long, which at the distance of UGCA 86, is about 31 kpc projected on the sky. The HI spur feature, identified in the middle and bottom panels of Figure 6.5 and seen in Figure 6.4, is observed in 108 channels from 656 – 763 for a velocity range of 66 – 153 km s^{-1}. The spur is about $16'$ in length, which is $\sim$14 kpc projected on the sky. It seems plausible that these features are related because of the continuity in the velocities between them. The systemic velocity of UGCA 86 is 72 km s^{-1} (see Table 6.1), and this lies between the velocities of the two features.

IC 342 also shows a surprising HI feature extending to the south. The tail-like structure connected to IC 342 seen in the top panel of Figure 6.5 is very tenuous but persists in about 59 channels over a velocity range of 37 – 84 km s^{-1}. A column density of 2.6 x 10^{18} cm^{-2} and a mass of 9.9 x $10^6 M_\odot$ was calculated for this HI tail and it extends about 0.°75 on the sky for a physical distance of approximately 40 kpc, at the distance of IC 342. The velocities of the tidal tail in IC 342 and the tail extending south and west from UGCA 86 are the same. Could these features be related?

It has been previously suggested that IC 342 and UGCA 86 are interacting (Rots 1979; Crosthwaite et al. 2000; Gray et al. 2002; Stil et al. 2005), and if the two tidal tails are related, then this would provide concrete evidence that IC 342 and UGCA 86 are indeed an interacting pair of galaxies. Although no HI bridge connecting the two HI tails of UGCA 86 and IC 342 was seen at the sensitivity limit, it is probable that they may be part of a continuous HI stream because they share the same velocities and relative position to one another. If these two tails do, in fact, comprise a continuous HI stream, then they could either be old tidal features in the process of dissipating and falling back onto their host galaxies (Hibbard 2000, and references therein) or they could be relatively new features still in the process of forming a continuous bridge (Tonnesen & Bryan 2010). The latter hypothesis seems more likely for the following reasons.

First, according to models of interacting galaxies made by Barnes & Hibbard (2009), short, compact features indicate a recent interaction while the tails having the same velocities could mean either the objects are near apocenter or the velocity

vectors of the tidal tails are perpendicular to the line of sight. UGCA 86 has a short, pronounced HI spur to the north of the disk, as discussed previously and shown in Figure 6.5, which gives credence to the interaction being recent. Second, UGCA 86 is experiencing an episode of enhanced star formation but not a global starburst (Stil, Gray & Harnett 2005). Hibbard (2000) explains that the timescales for interactions and subsequent starburst activity are quite different, as observed in systems like Arp 299 and the Antennae. The tidal tails in these galaxies, which stretch for hundreds of kpcs, formed hundreds of millions of years ago while the starburst activity occurred only tens of millions of years ago and may be episodic (Hibbard 2000).

Finally, the tidal tails of UGCA 86 and IC 342 are only a projected length of 31 and 40 kpc, respectively, which may mean that they are young features that haven't had enough time to extend fully (Tonnesen & Bryan 2010). If they were old features in the process of dissipating and falling back onto their host galaxies, then one would expect to see remnants of fine structure such as shells or loops (Hibbard 2000), assuming that the potentials in both galaxies are relaxed. Therefore, since neither UGCA 86 or IC 342 is experiencing intense starburst activity, both of their tidal tails in the south are relatively short, and UGCA 86 has a short, pronounced HI spur, it is likely that the interaction between the galaxies is recent. Hydrodynamic simulations are needed to study more concretely the true nature and timescale of the interaction between UGCA 86 and IC 342.

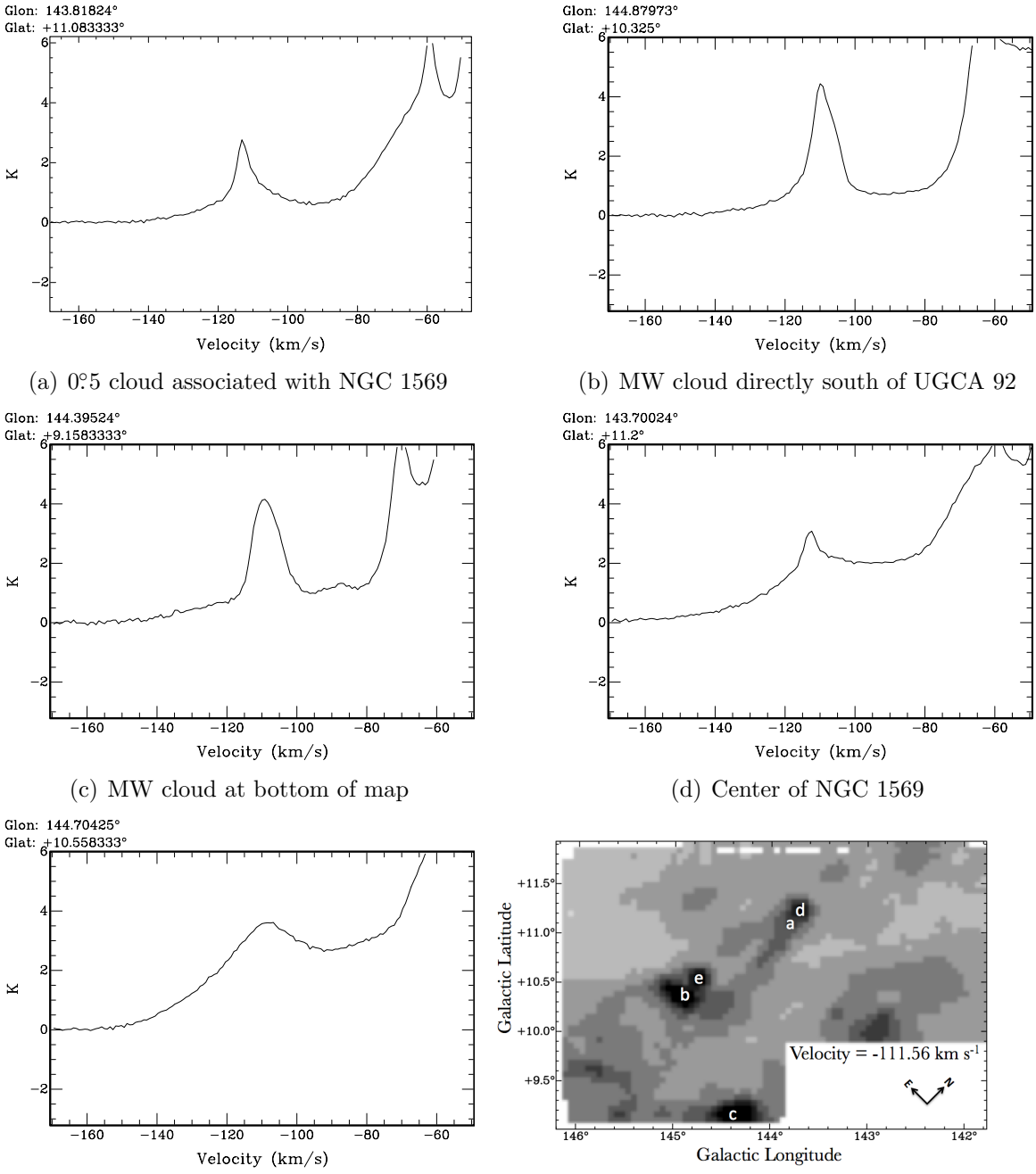

(a) 0.°5 cloud associated with NGC 1569

(b) MW cloud directly south of UGCA 92

(c) MW cloud at bottom of map

(d) Center of NGC 1569

(e) Center of UGCA 92

(f) Channel 435 showing positions of line profiles

Figure 6.9 Line profiles of NGC 1569 and UGCA 92 and three HI clouds nearby. The 0.°5 HI cloud likely associated with NGC 1569 has a line profile that is slightly blue-shifted, narrower, and has broader wings than the two MW cloud line profiles. NGC 1569 has a line profile that shows a narrow peak resembling that of the 0.°5 HI cloud. All profiles are plotted at the same scale for comparison.

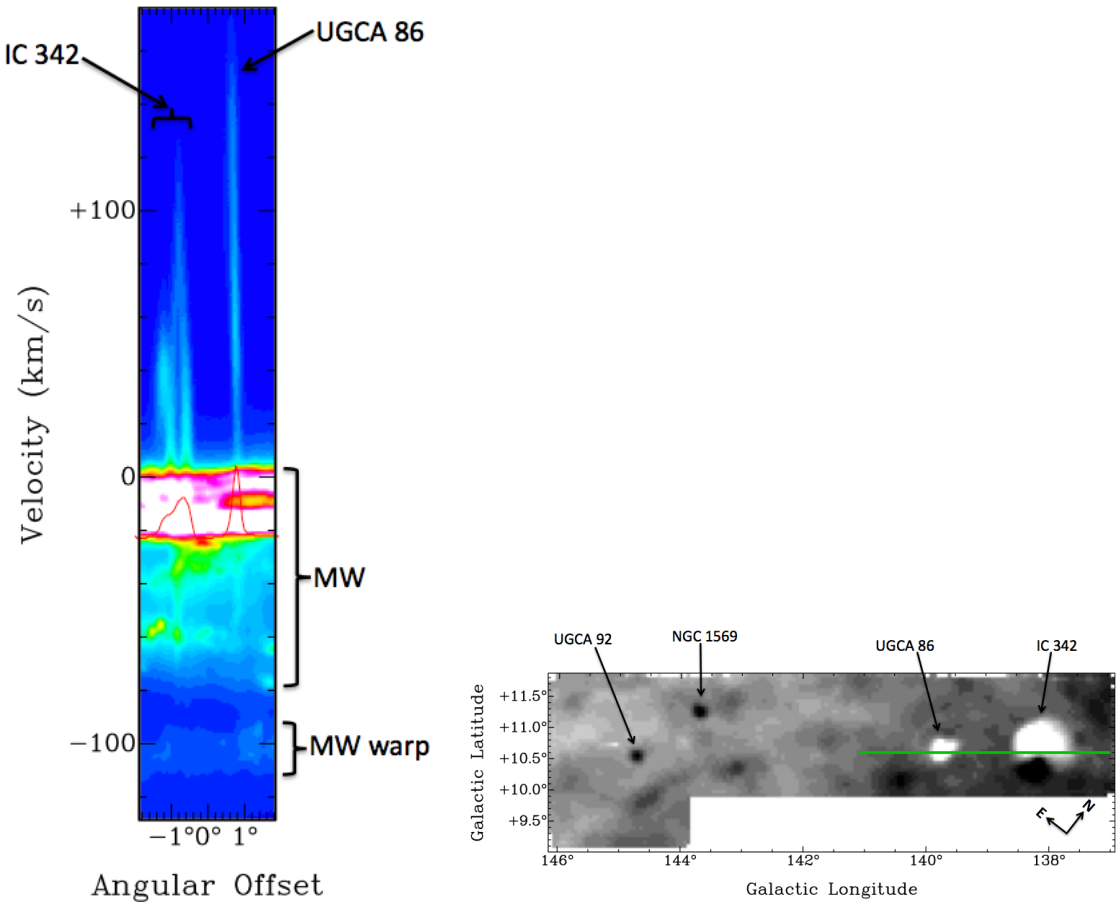

Figure 6.10 *Left*: P-V diagram along the green line shown in the right panel that slices through the centers of IC 342 and UGCA 86. The angular offset of 0° corresponds to the midway point between the two galaxies. Positive direction is southeast, toward UGCA 86 and negative direction is northwest, toward IC 342. IC 342 and UGCA 86 are marked as well as the MW and MW warp (Felix J. Lockman, private communication). *Right*: Intensity-weighted velocity map of the entire data cube. Black implies negative velocities and white shows positive velocities. The green line corresponds to the position of the slice used to create the P-V diagram in the left panel. The four galaxies are marked for reference as well as north and east.

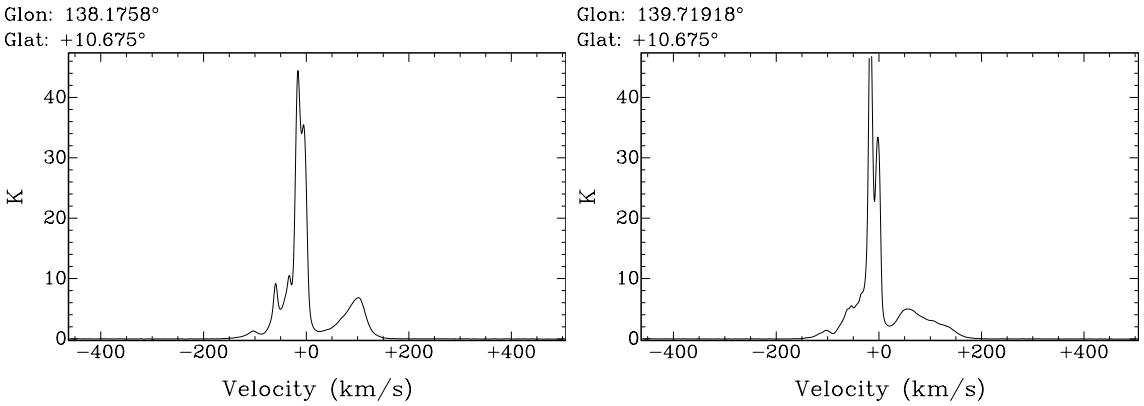

(a) Center of IC 342 (b) Center of UGCA 86

Figure 6.11 Line profiles through the centers of IC 342 and UGCA 86 showing entire spectrum. The MW emission appears at velocities less than ∼20 km s^{-1}.

6.5 A Model for NGC 1569

As described in the Introduction, NGC 1569 is a complex galaxy with complex stellar and gas kinematics. The stars display an increase, instead of a decrease, in velocity dispersion in the region of the SSCs compared to the center of the galaxy, and the stellar mass dominates the inner disk's gravitational potential. The HI data show strong non-circular motions across all of the disk, as detailed from VLA observations of the previous study. There is a strong non-circular motion HI cloud to the south of the SSCs that appears to be impacting the galaxy and could be responsible for the starburst and dense HI ridge and cloud that resides west of the SSCs. Also, there is tenuous HI emission detected with the VLA south and north of NGC 1569, and the velocities of this emission match those of the $0\overset{\circ}{.}5$ HI cloud discovered in the GBT map. The GBT data also show twin tidal tail-like features extending a projected distance of 88 kpc in the direction of another dwarf UGCA 92.

These observations paint a picture of a very disturbed dIm galaxy and prompt three possible explanations for the evolution that lead to the system seen today:

1) The extended HI features seen in the GBT map are primordial gas that is currently accreting onto NGC 1569. This gas infalls into the inner disk thereby creating the disturbed kinematics and starburst.

2) NGC 1569 is a merger remnant of two gas rich dwarf galaxies.

3) NGC 1569 is interacting with UGCA 92.

The possibility that the tidal tail-like structures and $0\overset{\circ}{.}5$ HI cloud seen in the GBT data are primordial gas is unlikely. In the early universe, primordial gas accretes onto galaxies through large-scale filamentary structures, which may be present around

the IC 342 group, including NGC 1569. However, the chances of this gas surviving in a dense galaxy group to the present time seems improbable. Background UV photoionization from AGN and nearby galaxies along with local group disturbances cause gas to dissipate and evaporate on timescales of about 1 Gyr (Holwerda et al. 2011). Therefore, a primordial origin for these structures is ruled out.

A merger is much more plausible since merger remnants of large disk galaxies have similar characteristics, particularly the twin tails and starburst activity only on larger scales. For example, the ongoing merger Arp 299 shows very long, parallel HI tidal tails that share the same velocities (Hibbard & Yun 1999), which are similar to the tidal tails detected in NGC 1569. Arp 299 is also undergoing an intense starburst, and has very disturbed kinematics in both stars and HI (Hibbard & Yun 1999). However, there are major differences between Arp 299 and NGC 1569. Arp 299 has *stellar* tidal tails and also contains two distinct nuclei (Hibbard & Yun 1999). Although a low brightness stellar population in the tidal tails of NGC 1569 has not been looked for, a double concentration left-over from the two parent galaxies is not observed.

In the merger remnant NGC 1052 there exist two HI tidal tails (van Gorkom et al. 1986) and it is undergoing a starburst as well (Pierce et al. 2005), similar to NGC 1569. However, NGC 1052 has an ionized gas disk that rotates perpendicular to the stellar disk (van Gorkom et al. 1986), and has an E4 morphology (NED). One of the striking results from the previous work on NGC 1569 is that the stars and the gas kinematically follow each other. This is not what is observed in NGC 1052, and NGC 1569 does not have an elliptical shape.

The merging scenario to explain the observed features of NGC 1569 is compelling, but still there are obvious drawbacks when compared to larger merger remnant galaxies. Large spiral disk galaxies are more complex with supermassive black holes in their centers, spiral arms, and bulges in some that all combine for a more dramatic merging event than is expected in the dwarf galaxy regime. Gas rich dwarfs do not have the sophisticated structure of their spiral galaxy counterparts nor do they contain supermassive black holes that can ignite and become active during a merging event as is the case of NGC 1052. But, no one, as yet, has modeled dwarf-dwarf galaxy mergers so understanding the morphological changes that can occur in these systems is unknown. Spiral-spiral galaxy mergers generally produce elliptical systems. Could this be the case for disky dwarf galaxies, too? If so, then perhaps the E4 galaxy NGC 1052 is at a later stage of merging than NGC 1569, which may be on its way to becoming a dE (dwarf elliptical) system.

If NGC 1569 is a merger remnant, the HI "companion" identified by Stil & Israel (1998) is possibly the gas remnant from one of the dwarfs in the merger. The velocities of this HI "companion" match the velocities of the GBT 0.°5 HI cloud, which suggests that these structures may have a similar origin. However, it is also possible that the 0.°5 HI cloud came from a recent interaction with UGCA 92, discussed below, and thus, the HI "companion" may have formed from an interaction rather than a merger.

NGC 1569 interacting with UGCA 92 is also a reasonable explanation for the observations. The tidal tails and the large HI cloud extending out toward UGCA 92 make an interaction plausible simply by the orientation of the features. NGC 4631 is an intriguing analogue for comparison to NGC 1569 because it also has two v-shaped

HI tidal tails extending out toward its nearest companion, NGC 4656 (see Figure 1 in Weliachew et al. 1978). The similarity in morphology is striking. NGC 4631, also part of a galaxy group, is experiencing a starburst.

Barnes & Hibbard (2009) state that, from their models, long and narrow tidal features associated with an interaction indicate an older passage between two interacting systems. Similarly, Hibbard (2000) explains that the timescales for a starburst and an interaction can be very different with an interaction taking place hundreds of millions of years in the past while starbursts are episodic with the most recent occurrence taking place only tens of millions of years ago. NGC 1569 has long, extended tidal tails, which are indicative of an older passage by UGCA 92, according to Barnes & Hibbard.

The timescale of the most recent starburst episode in NGC 1569 is on the order of 10 Myr and this dIm galaxy has had multiple bursts of intense star formation (Angeretti et al. 2005), consistent with Hibbard's (2000) results. If NGC 1569 and UGCA 92 are interacting, then a rough estimate can be made of how long ago the pericenter approach was by using the GBT projected distance between the objects of $\sim 2^{\circ}$, which, at a distance of 3.36 Mpc, corresponds to a physical distance of $\sim$117 kpc. If NGC 1569 is moving through space at its radial systemic velocity of -85.6 km s^{-1}, then it would take about 500 Myr for NGC 1569 to get 117 kpc away from UGCA 92, assuming NGC 1569 and UGCA 92 are moving apart at the same speed and are in the plane of the sky. The timescale of the most recent starburst and the time in which the last interaction could have occurred are roughly consistent with

Hibbard (2000). Thus, the picture of NGC 1569 is consistent with other observations and models of interacting disk galaxies.

Hydrodynamic simulations are needed in order to determine the true nature and evolutionary history of NGC 1569. With these sophisticated simulations, it is possible to distinguish between the roles of mergers and interactions by comparing them to the detailed observations. Not only will these simulations be able to replicate the morphologies observed in NGC 1569, but they can also model the star formation history, which can provide more insight into the starburst activity. Furthermore, by running the simulations forward in time, a prediction can be made of what the final fate of NGC 1569 will be. Given these scenarios, it is postulated that NGC 1569 is a transition dwarf, between a dIm and probably a dE galaxy.

6.6 Conclusions

The GBT data presented here have several exciting implications. The results are outlined below.

1) Although no HI connection between NGC 1569/UGCA 92 and IC 342/UGCA 86 was observed in the GBT map, a large, 29 kpc diameter HI cloud residing directly over NGC 1569 extending perpendicularly to the south toward UGCA 92 was discovered. This 0.°5 HI cloud has a narrower velocity profile, is slightly blue-shifted, and has broad wings compared to other foreground MW clouds in the vicinity of NGC 1569.

2) Two v-shaped tidal tail structures were also discovered extending out from NGC 1569 perpendicular to the disk. These tail structures also have narrow velocity widths, $\sim$4 km s^{-1}, and no similar features were seen in the rest of the GBT map. Therefore,

the tidal tails are likely associated with NGC 1569. The tidal tails reach about 88 kpc toward UGCA 92.

3) The cloud and tidal tails could be evidence for a recent interaction between NGC 1569 and UGCA 92, but a merger of two dwarfs is also possible.

4) In the velocity ranges of UGCA 86, a counter tidal tail was discovered on the opposite side of the disk from the HI spur identified by Stil et al. (2005). This counter tail has velocities that are more blue-shifted than the HI spur but also overlaps with the beginning velocities of the spur. This counter tail is likely associated with the HI spur, and was probably created in an interaction with IC 342.

5) IC 342 also showed a surprising HI tail-like feature extending south toward UGCA 86. This HI tail is very tenuous at the sensitivity limit of the GBT map, but appears over $\sim$47 km s^{-1} and has the same velocities as the HI tail detected in UGCA 86. The two HI tails associated with UGCA 86 and IC 342 discovered in the GBT map, may be young features and physically related from a recent interaction, although the data do not show a bridge connecting the two structures.

For future work, a plan is in place to investigate what would morphologically be expected from interactions between NGC 1569 and UGCA 92 as well as IC 342 and UGCA 86 using using hydrodynamic simulations. Furthermore, by implementing all necessary physics, including stellar feedback, the cosmological origin of NGC 1569 can be explored and its evolutionary fate determined.

– 7 –

Summary and Future Work

7.1 Summary of Results from This Work

7.1.1 Stellar Kinematics

1) A systemic velocity, $V_{\rm sys}$, of -82 ± 7 km s^{-1} was determined from averaging the heliocentric radial velocities of the stars along the minor axis.

2) NGC 1569 has a stellar kinematic major axis equal to the morphological major axis at a position angle, measured east from north, of 121° and an inclination angle of 60° as ascertained by de-projecting the intermediate position angles onto the major axis.

3) The stars and gas kinematically follow each other.

4) NGC 1569 has an average stellar velocity dispersion of $< \sigma_{\rm z} > = 21 \pm 4$ km s^{-1} and a kinematic measure, $V_{\rm max}/< \sigma_{\rm z} > = 2 \pm 2$, which is suggestive of a thick disk at a radius of ~ 0.5 kpc from the galaxy center.

5) The stellar velocity dispersion increases from 21 ± 4 km s^{-1} to 33 ± 9 km s^{-1} in the region of the SSCs, perhaps indicating a thicker stellar disk.

6) The $\sigma_{\rm z}$ – $M_{\rm B}$ relation discussed by Swaters (1999) is in perfect agreement with what is observed for NGC 1569; thus, NGC 1569 follows the observed trend in large spiral galaxies.

7) The light profile of NGC 1569 follows an exponential disk profile better than a de Vaucouleurs's R$^{1/4}$ profile. However, the profile is shallower in the outer disk than in the inner disk.

7.1.2 Ionized Gas Kinematics

1) Multiple velocity components are observed in the spectra as a result of two forms of ionized gas. One form is the high velocity ionized gas from blowout resulting from the starburst. The second form is low velocity ionized gas that is likely from nearby HII regions that formed the stars observed in the stellar spectra.

2) There are three expanding shells observed from the high velocity ionized gas seen along the major axis.

3) The integrated stellar velocities match the central velocity ionized and HI gas and is likely produced by the stars that caused the expanding shell observed on the western side of the disk.

7.1.3 HI Kinematics

1) By implementing a new multi-scale cleaning algorithm, tenuous HI emission to the south and north of NGC 1569 was imaged for the first time.

2) NGC 1569 shows a dominance of non-circular motions across the HI disk as seen in the intensity-weighted velocity field.

3) A double Gaussian decomposition method was applied to the HI data to extract a bulk velocity field, a strong noncircular motion velocity field, and a weak non-circular motion velocity field.

4) A strong non-circular motion HI cloud was observed and appears to be impacting NGC 1569 at the eastern edge of a dense HI cloud that lies west of the SSCs.

5) The strong non-circular motion HI cloud either snowplowed the gas into a dense ridge that then collapsed, creating the starburst, or, the dense ridge was already

present and the HI cloud caused the ridge collapse during its impact.

7.1.4 Mass Modeling

1) The stellar mass profile follows an exponential profile better than an $R^{1/4}$ profile.

2) A total stellar mass of 2.8 x 10^8 $M_\odot$ was determined from a new SED fit and a total gas mass, including helium and metals, of 2.34 x 10^8 $M_\odot$ was measured.

3) A dynamical mass of 1.1 x 10^9 $M_\odot$ was calculated from the $V_{\rm max} = 50$ km s^{-1} at a radius of 2 kpc.

4) The stars dominate the gravitational potential in the inner half of the HI disk.

5) The derived rotation curve from the HI kinematics compared to the modeled HI rotation from the surface mass density and the modeled stellar rotation, shows that only a small amount, 80% of the baryonic mass, is needed in dark matter. This is unlike typical spiral and elliptical galaxies.

6) When compared to an NFW profile, the rotation of the stars and gas seem to agree at a radius of $\sim$ 2 kpc. The NFW profile does over-estimate the inner 1.5 kpc radius, which is likely due to the well-known cusp-core problem.

7) The NFW model predicts a virial mass of 1.6 x 10^{11} $M_\odot$ and gives a virial radius of 22 kpc.

7.1.5 Kinematic and Morphological Comparisons

1) When the integrated stellar velocities are plotted on top of an optical *HST* image, it is seen that the disturbed kinematics correspond with the region near SSC A. It is

likely that the stars caused the HI hole from blowout and are not ionizing the leftover gas.

2) A "butterfly" shape in the HI gas morphology is observed, likely caused from blowout from the starburst.

3) NGC 1569 has the characteristics of other starburst dIm transition objects and may be a transition object itself.

7.1.6 GBT Mapping

1) Although no HI connection between NGC 1569/UGCA 92 and IC 342/UGCA 86 was observed in the GBT map, a large, 29 kpc diameter HI cloud residing directly over NGC 1569 extending perpendicularly to the south toward UGCA 92 was discovered. This 0°.5 HI cloud has a narrower velocity profile, is slightly blue-shifted, and has broad wings compared to other foreground MW clouds in the vicinity of NGC 1569.

2) Two v-shaped tidal tail structures were also discovered extending out from NGC 1569 perpendicular to the disk. These tail structures also have narrow velocity widths, $\sim$4 km s^{-1}, and no similar features were seen in the rest of the GBT map. Therefore, the tidal tails are likely associated with NGC 1569. The tidal tails reach about 88 kpc toward UGCA 92.

3) The cloud and tidal tails could be evidence for a recent interaction between NGC 1569 and UGCA 92, but a merger of two dwarfs is also possible.

4) In the velocity ranges of UGCA 86, a counter tidal tail was discovered on the opposite side of the disk from the HI spur identified by Stil, Gray, & Harnett (2005). This counter tail has velocities that are more blue-shifted than the HI spur but also

overlaps with the beginning velocities of the spur. This counter tail is likely associated with the HI spur, and was probably created in an interaction with IC 342.

5) IC 342 also showed a surprising HI tail-like feature extending south toward UGCA 86. This HI tail is very tenuous at the sensitivity limit of the GBT map, but appears over $\sim$47 km s^{-1} and has the same velocities as the HI tail detected in UGCA 86. The two HI tails associated with UGCA 86 and IC 342 discovered in the GBT map, may be young features and physically related from a recent interaction, although the data do not show a bridge connecting the two structures.

7.2 The Evolution of NGC 1569

NGC 1569 has proven to be a system that is complex. It appears to show evidence for a recent interaction or merger and is likely in transition between a dIm and dE galaxy. If NGC 1569 did evolve from a recent interaction or merger, then perhaps other dIm starburst systems evolved from similar mechanisms. Understanding how this dIm post-starburst system evolved and will continue to change is essential for our understanding of how galaxies formed in the early universe.

7.3 Future Work

In order to better understand the nature of dIm starburst systems like NGC 1569, I plan to undertake a study of five additional objects that possess characteristics similar to NGC 1569. This future work includes mapping extending areas around the five galaxies using the GBT for three northern hemisphere objects and the Parkes Radio Telescope for two southern hemisphere systems. I intend to form collaborations with experts at NRAO, Green Bank for the observations. In addition, I also plan to form

a collaboration with hydrodynamic simulation experts in order to model dwarf-dwarf galaxy mergers and interactions. The purpose of these simulations will be to identify the primary mechanism responsible for producing dIm starburst galaxies in the nearby universe. This work will provide a platform for understanding how galaxies formed in the early universe as well as predict how these systems will eventually evolve.

7.3.1 Observations

7.3.1.1 Galaxy Sample

For the observations, we will add to the growing list of starburst dIm galaxies that have been searched for extended HI by observing five more objects, described in detail in the following sections. The systems were chosen based on the following criteria: (1) dIm morphological type; (2) currently in a starburst or post-starburst phase; and (3) within a distance ≤ 5 Mpc. Table 7.1 lists some of the physical properties of the dIm galaxies in our sample.

The five chosen galaxies will be the targets for neutral hydrogen HI-line spectral observations using single-dish radio telescopes. I plan to work at NRAO, Green Bank for the observational component of this project and form collaborations with the astronomers who are experts in these kinds of observations. Together, we plan to map large areas around the dIm galaxies to search for HI structures, similar to the ones detected around NGC 1569. Detections of such structures would strengthen our hypothesis that these dIm galaxies are undergoing mergers or interactions with other galaxies.

Table 7.1. Physical characteristics of the dIm galaxies in sample

Object Name	RA (J2000)[a] HH:MM:SS	DEC (J2000)[a] ° : ′ : ″	D[b] Mpc	$V_{\rm Helio}$[c] km s^{-1}	$M_{\rm B}$[d] mag	Group[e] Association
IC 10	00:20:17.3	+59:18:14	0.820	-352.0	-15	—
NGC 4163	12:12:09.1	+36:10:09	2.96	165	-13.66	CVn I Cloud
NGC 4214	12:15:39.2	+36:19:37	2.7 ± 0.2	291	-16.93 ± 0.22	CVn I Cloud
NGC 5408	14:03:20.9	-41:22:40	4.81	506 ± 3	-16.12 ± 0.09	Cen A
IC 4662	17:47:08.8	-64:38:30	2.44	302 ± 3	-14.91 ± 0.1	—

[a]All RA and DEC taken from NED

[b]IC 10 from Wilcots & Miller (1998); NGC 4163 from Karachentsev et al. (2006); NGC 4214 from McQuinn et al. (2010); NGC 5408 and IC 4662 taken from van Eymeren et al. (2010) and references therein;

[c]IC 10 from Wilcots & Miller (1998); NGC 4163 and NGC 4214 from NED; NGC 5408 and IC 4662 from van Eymeren et al. (2010) and references therein;

[d]IC 10 from Wilcots & Miller (1998); NGC 4163 and NGC 4214 from McQuinn et al. (2010); NGC 5408 and IC 4662 from van Eymeren et al. (2010) and all references therein;

[e]NGC 4163 and NGC 4214 from Kaisin & Karachentsev (2008); NGC 5408 from Karachentsev et al. (2002).

The last column in Table 7.1 identifies NGC 4163, NGC 4214 and NGC 5408 as having known galaxy group associations. Because of the denser environment, these objects may be interacting with other members of their respective groups. They could also be merger remnants. On the other hand, IC 10 and IC 4662 have no detectable galaxy group associations, as discussed previously. Even so, according to van Eymeren et al. (2010), IC 4662 has a very distorted HI velocity field and they suggest that this system is the merger remnant of two independent dwarf galaxies. In all cases, if interactions are responsible for the recent starbursts, then HI structures should still be present and detectable with single-dish radio telescopes.

7.3.1.2 Green Bank Telescope

For the northern hemisphere objects, IC 10, NGC 4163 and NGC 4214, we will use the GBT to create deep HI maps around these galaxies. The GBT has a diameter of 100 meters and is the world's largest fully steerable radio telescope. The GBT also has an unblocked aperture due to its off-axis feed-arm that supports both the primary and secondary optics (Jewell & Prestage 2004). This results in reduced side-lobes and thus the maps made with this telescope are less confused by extraneous radiation. GBT has a half-power-beam-width (HPBW) of about $9'$ at 21 cm and enables very high velocity resolution ($<$ 1 km/s) due to its large bandpass capabilities and high sensitivity. The GBT is the premier instrument for obtaining HI spectral data for our proposed northern hemisphere objects.

We aim to achieve similar sensitivity as our previous data on NGC 1569 of N_{HI} $\sim$ 5 x 10^{16} cm^{-2} in a 1 km s^{-1} channel. Thus, we scale by the $\sim$80 hours it took to achieve this sensitivity in our HI map of NGC 1569 to determine the integration times of our proposed five objects. We calculate that we will need 120 hours for IC 10 to cover the proposed area of 30 square degrees, while for NGC 4163/4214, we will need 50 hours to cover 15 square degrees. This amount of observing time on the GBT is reasonable to acquire over a three year timeframe. A GBT observing proposal to map NGC 4163/4214 has been submitted.

IC 10: We select a 5° x 6° region around IC 10 to search for extended HI structure. We arrive at this area by scaling the $\sim$1.5° tidal tail features present in the NGC 1569 map to the distance of IC 10. These tidal tail features, shown in Figure 6.7,

correspond to a physical length of 88 kpc at the 3.36 Mpc distance (Grocholski et al. 2008) of NGC 1569. Therefore, since IC 10 is only at a distance of 820 kpc (Wilson et al. 1996), we need a map that has dimensions of at least 6° to encompass tidal tail features the size of those seen in NGC 1569. Furthermore, we position the area such that IC 10 is offset to the north from the center of the rectangular map because Wilcots & Miller (1998) show that there is extended gas to the south of the host galaxy disk.

NGC 4163/4214: For these two dIm starburst galaxies, we select a 5° x 3° area that includes NGC 4163, NGC 4214 and six of the nearest Canes Venatici Cloud I galaxy group members. Since both of these objects are part of a known galaxy group, we select a reasonable region within which interactions are likely. According to Simpson & Gottesman (2000), NGC 4163 shows tenuous emission surrounding the host disk galaxy, as determined from high-resolution HI data, and it has a chaotic velocity field.

7.3.1.3 Parkes Radio Telescope

For the southern hemisphere objects, NGC 5408 and IC 4662, we propose to use the Parkes Radio Telescope, located just outside Parkes, Australia. This telescope is fully steerable and has a dish diameter of 64 meters. We propose to use on-the-fly-mapping with the L-band multi-beam receiver, which has a HPBW of 14°.4, to map the regions outlined in Figure 7.2. With the $\sim 14'$ resolution, structures similar to those detected in NGC 1569 will be resolved to physical scales of 14 kpc, at the 3.36 Mpc distance

of NGC 1569, which is high enough resolution to resolve HI features that may be around NGC 5408 and IC 4662.

Again, if we scale by the integration time that we used for NGC 1569, to obtain similar sensitivity (taking into account the difference in dish size), we will need about 200 hours for NGC 5408 to cover the proposed area of 24 square degrees, while for IC 4662, we will need 40 hours to cover 4 square degrees. This amount of time is also reasonable to acquire over a three year timeframe.

NGC 5408: We select an 8° x 3° region that encompasses NGC 5408 and four of the nearest Centaurus A galaxy group members. See the upper left filled black circle in the red box in the top panel of Figure 7.2. We choose this region because it contains four of the nearest group members and therefore, we believe extended HI structures will most likely be seen in the direction of neighboring objects, if they exist. Furthermore, van Eymeren et al. (2010) show high-resolution HI data from the Australia Telescope Compact Array of the HI disk in NGC 5408 and the results indicate faint emission to the west and south of the host galaxy. Therefore, a region that extends out in the direction of the faint emission as well as connecting to group members, seems like the most plausible area to search.

IC 4662: We select the 2° x 2° region outlined in the bottom panel of Figure 7.2 because, according to van Eymeren et al. (2010), extended HI emission in the disk of IC 4662 is stretching out toward the east and to the south. Therefore, we offset IC 4662 to the northwest from the center of the of the square area. We assume, once again, that if extended features are detected like they were for NGC 1569, then they will probably follow the distorted HI seen in the disk of the host galaxy.

7.3.2 Hydrodynamic Simulations

The primary objective of the simulation component of this future research is to develop a family of simulations that together are capable of capturing the essential physics of ISM and star formation, and to model the observed dIm galaxies faithfully. With this family of simulations, we can understand the formation, evolution, and future fate of dIm starburst galaxies. These theoretical simulations, combined with observations, will together resolve the true nature of these objects and provide valuable constraints on the greater cosmological history of our universe.

We will use the adaptive refinement tree (ART) code developed by Andrey Kravtsov, Douglas Rudd, Anatoly Klypin, and Nick Gnedin (Rudd et al. 2008; Kravtsov et al. 2002). This ART code begins in a large domain with a grid of uniform cells of a given size. Then, as the simulation advances, both baryonic and dark matter within a single cell can be resolved further through the use of mesh refinement. The subsequent cell will have half the size of the previous cell but the original grid of the initial cell will be applied to the new one, thus increasing the resolution. As the simulation progresses, more resolution can be achieved by repeating the mesh refinement process. This mesh refinement algorithm is perfect for the context of isolating dwarf-dwarf galaxy mergers and obtaining high mass resolution of $\sim$1.3 x 10^6 $M_\odot$ in dark matter and $\sim 10^3$ $M_\odot$ in baryonic matter (Kravtsov 2003). This mass resolution is capable of duplicating all observed HI structures, such as the large, $0\farcs5$ HI cloud in Figure 6.6 that has a mass of $\sim$2.7 x 10^7 $M_\odot$. Furthermore, these simulations will be able to resolve individual star clusters and stars, thereby resolving the starbursts themselves.

In addition to the high mass resolution, the ART code is capable of following the formation and destruction of molecular hydrogen, taking into account catalyzing and shielding effects of dust and H_2 dissociation by local ultraviolet sources (Gnedin & Kravtsov 2011). Star formation based on molecular hydrogen cloud formation can lead to significantly different star formation properties in low metallicity objects such as the dIm galaxies in our sample (Gnedin & Kravtsov 2010; Krumholz et al. 2009). Therefore, the sophisticated method of incorporating molecular cloud formation that ART encompasses permits accurate modeling of star formation and, thus, enables us to replicate the starburst nature of our proposed objects. These innovative simulations also include all the physics necessary to reproduce dwarf galaxy constituents such as stellar feedback, dust, the enrichment of heavy elements, and stellar mass loss. One of the most fundamental components of the ART simulations to the proposed research is the robust treatment of gas dynamics. The ART code employs a Eulerian shock-capturing Godunov hydrodynamics solver in conjunction with Adaptive Mesh Refinement (Robertson et al. 2010).

This code will be used to create a series of simulations that explore the formation and evolution of different dwarf gas disks. To get a firm baseline of what results one would get without interactions or mergers, we plan to start with simulations of isolated galaxies and vary different prescriptions for ISM physics, star formation, and feedback to see if we can match our observed sample. Then, we will compare these simulations of isolated galaxies with simulations in which the modeled gas disks undergo tidal interactions and mergers. This way we can assess the true role of interactions and

mergers. By running the simulations forward in time, we can determine what these starburst dwarfs will become.

We plan to vary the parameter space of the merger and tidal interaction simulations so that we can understand the following: (a) the mass ratio between two merging dwarf galaxies that produces a starburst dIm system; (b) the type of collision that causes the systems to merge (e.g., head-on collision vs. an angled collision); (c) the speed at which two dwarf galaxies merge together; and, for interacting systems, (d) how close do the dIm objects have to get to their neighbor(s) in order to create the observed characteristics; and (e) are there detectable differences between mergers and interactions. During the course of these studies, there are likely to be other parameters that will be tested as these simulations evolve.

There are two other codes, Gadget, written by Volker Springel, and RAMSES, written by Romain Teyssier, that are currently being used by simulation experts. These two simulation codes have been used for isolated galaxy simulations and merger simulations. One goal of the simulation aspect for this research will be to compare the results of these codes with those of the ART. This way, we can minimize and flush out systematic effects of the respective simulations.

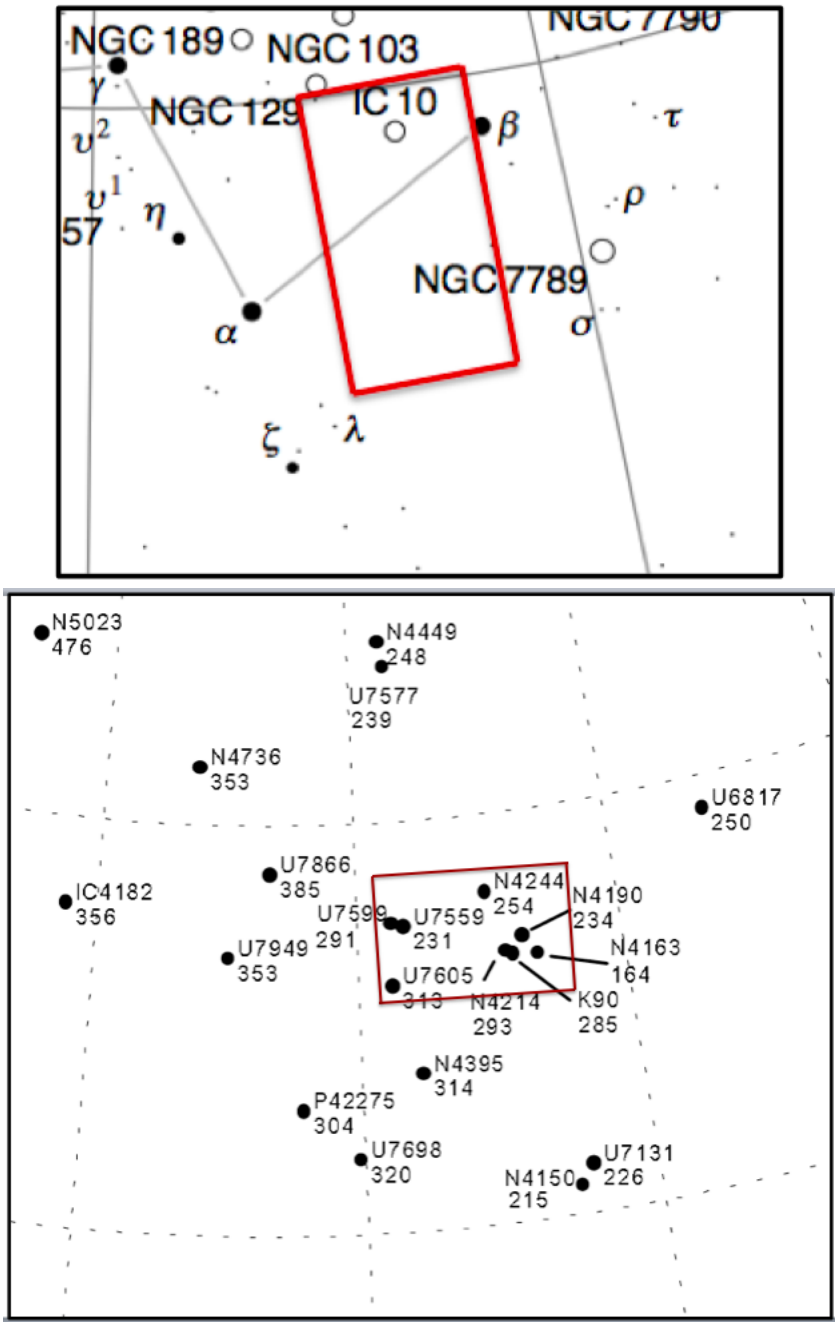

Figure 7.1 Top: Regions to map with the GBT, marked in red, for dIm galaxy IC 10. Bottom: Regions to map for NGC 4163 & NGC 4214. The region around IC 10 represents a 5° x 6° (RA x DEC) rectangular map, while the region around NGC 4163 and NGC 4214 represents a 5° x 3° (RA x DEC) rectangular map. *Note: Finding chart for IC 10, top, taken from http://commons.wikimedia.org/wiki/File:Cassiopeia_charta.png. Finding chart for NGC 4163/4214, bottom, taken from Figure 1, Makarova et al. (1998).*

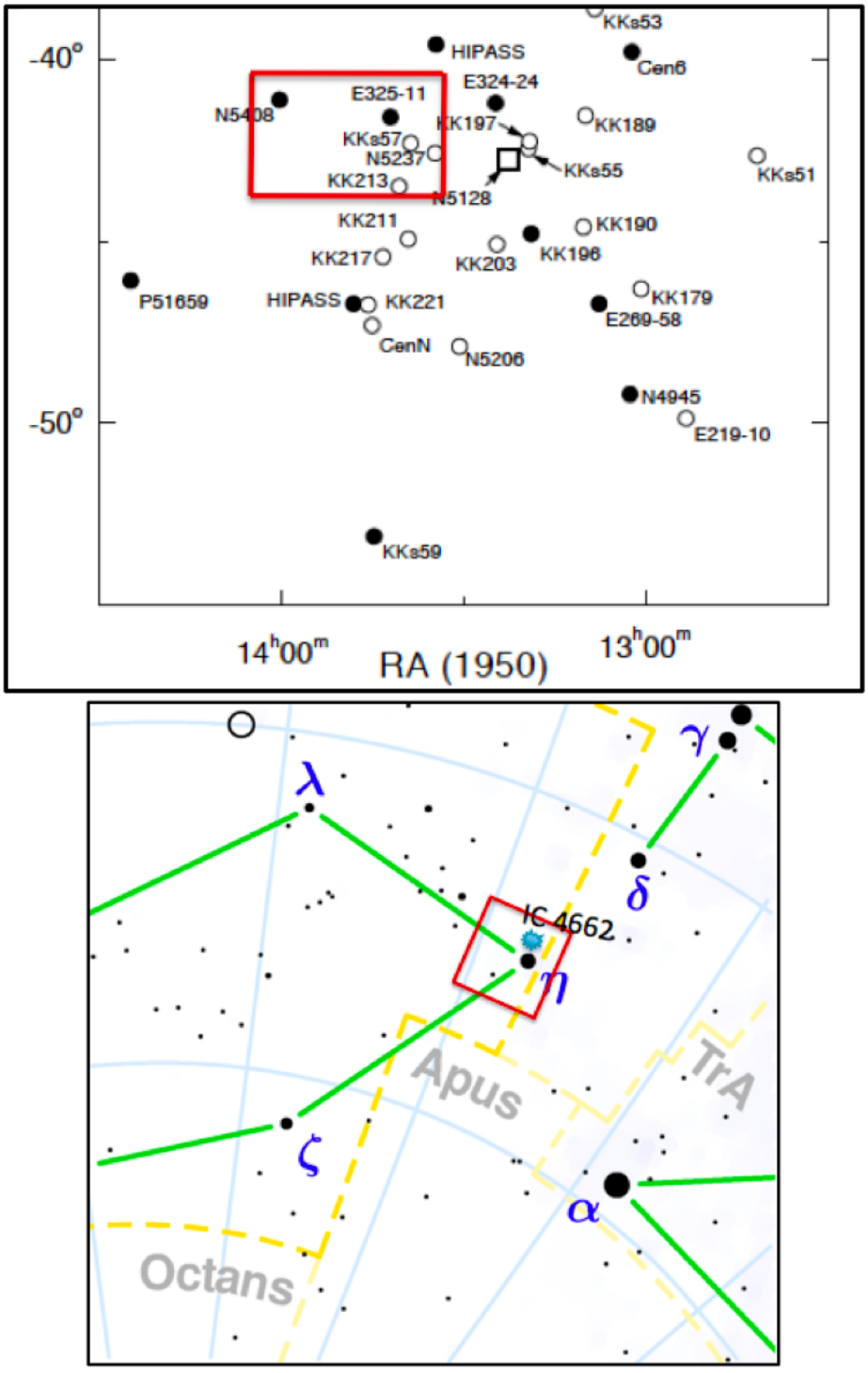

Figure 7.2 Top: Regions to map with the Parkes Radio Telescope, marked in red, for dIm galaxy, NGC 5408. Bottom: Regions to map for IC 4662. *Note: Finding chart for NGC 5408, left, taken from Figure 7.1 in Karachentsev et al. (2002). Finding chart for IC 4662 taken from http://upload.wikimedia.org/wikipedia/commons/c/cb/Pavo_constellation_map.png.*

REFERENCES

[1] Aloisi, A., Clampin, M., Diolaiti, E., Greggio, L., Leitherer, C., Nota, A., Origlia, L., Parmeggiani, G., & Tosi, M. 2001, AJ, 121, 1425

[2] Angeretti, L., Tosi, M., Greggio, L., Sabbi, E., Aloisi, A., & Leitherer, C. 2005, AJ, 129, 2203

[3] Barazza, F. D., Wolf, C., Gray, M. E., Jogee, S., Balogh, M., McIntosh, D. H., Bacon, D., Barden, M., Bell, E. F., Böhm, A., Caldwell, J. A. R., Häussler, B., Heiderman, A., Heymans, C., Jahnke, K., van Kampen, E., Lane, K., Marinova, I., Meisenheimer, K., Peng, C. Y., Sanchez, S. F., Taylor, A., Wisotzki, L., & Zheng, X. 2009, A&A, 508, 665

[4] Barnes, J. E., & Hibbard, J. E. 2009, AJ, 137, 3071

[5] Begeman, K. G. 1989, A&A, 223, 47

[6] Bell, E. F., & de Jong, R. S. 2001, ApJ, 550, 212

[7] Bell, E. F., Baugh, C. M., Cole, S., Frenk, C. S., & Lacey, C. G. 2003, MNRAS, 343, 367

[8] Binney, J., & Tremaine, S. 1987, Galactic Dynamics (Princeton: Princeton University Press)

[9] Blanton, M. R., Lupton, R. H., Schlegel, D. J., Strauss, M. A., Brinkmann, J., Fukugita, M., & Loveday, J. 2005, ApJ, 631, 208

[10] Bosma, A. 1981, AJ, 86, 1825

[11] Bottema, R. 1993, A&A, 275, 16-36

[12] Boylan-Kolchin, M., Springel, V., White, S. D. M., Jenkins, A., & Lemson, G. 2009, MNRAS, 398, 1150

[13] Brosch, N., Almoznino, E., & Heller, A. B. 2004, MNRAS, 349, 357

[14] Bruzual, G., & Charlot, S. 2003, MNRAS, 344, 1000

[15] Bullock, J. S., Kolatt, T. S., Sigad, Y., Somerville, R. S., Kravtsov, A. V., Klypin, A. A., Primack, J. R., & Dekel, A. 2001, MNRAS, 321, 559

[16] Bureau, M., & Carignan, C. 2002, AJ, 123, 1316

[17] Burkert, A. 1997, ApJ, 474, 99

[18] Burstein, D., & Heiles, C. 1982, AJ, 87, 1165

[19] Buta, R. J., & McCall, M. L. 1999, ApJS, 124, 33

[20] Cardelli, J. A., Clayton, G. C., & Mathis, J. S. 1989, ApJ, 345, 245

[21] Chabrier, G. 2003, PASP, 115, 763

[22] Charlot, S., & Fall, S. M. 2000, ApJ, 539, 718

[23] Chilingarian, I. V., Prugniel, P., Sil'Chenko, O. K., & Afanasiev, V. L. 2007, MNRAS, 376, 1033

[24] Cole, S., Lacey, C. G., Baugh, C. M., & Frenk, C. S. 2000, MNRAS, 319, 168

[25] Conroy, C., & Wechsler, R. H. 2009, ApJ, 696, 620

[26] Conselice, C. J., Gallagher, J. S., III, & Wyse, R. F. G. 2001, ApJ, 559, 791

[27] Cornwell, T. J. 2008, ISTSP, 2, 793

[28] Crosthwaite, L. P., Turner, J. L., & Ho, P. T. P. 2000, AJ, 119, 1720

[29] de Blok, W. J. G., Walter, F., Brinks, E., Trachternach, C., Oh, S.-H., & Kennicutt, R. C. 2008, AJ, 136, 2648

[30] de Blok, W. J. G. 2010, Advances in Astronomy, 2010, 0910.3538

[31] de Lapparent, V., Arnouts, S., Galaz, G., & Bardelli, S. 2004, A&A, 422, 841

[32] de Rijcke, S., Michielsen, D., Dejonghe, H., Zeilinger, W. W., & Hau, G. K. T. 2005, A&A, 438, 491D

[33] de Vaucouleurs, G., de Vaucouleurs, A., Corwin, H. G., Jr., Buta, R. J., Paturel, G., & Fouqué, P. 1991 Third Reference Catalogue of Bright Galaxies (New York: Springer-Verlag)

[34] Dellenbusch, K. E., Gallagher, J. S. III, Knezek, P. M., & Noble, A. G. 2008, AJ, 135, 326

[35] Dunn, J. M. 2007, PhD Dissertation, Texas Christian University

[36] Dunn, J. M. 2010, MNRAS, 408, 392

[37] Erwin, P., Beckman, J. E., & Pohlen, M. 2005, ApJ, 626, 81

[38] Fingerhut, R. L., Lee, H., McCall, M. L., & Richer, M. G. 2007, ApJ, 655, 814

[39] Forbes, D. A., & Bridges, T. 2010, MNRAS, 404, 1203

[40] Geha, M., van der Marel, R. P., Guhathakurta, P., Gilbert, K. M., Kalirai, J., & Kirby, E. N. 2010, ApJ, 711, 361G

[41] Gerssen, J., Kuijken, K., & Merrifield, M. R. 1997, MNRAS, 288, 618

[42] Gnedin, N. Y., & Kravtsov, A. V. 2010, ApJ, 714, 287

[43] Gnedin, N. Y., & Kravtsov, A. V. 2011, ApJ, 728, 88

[44] Götz, M. 1990, PhD Dissertation, University Bonn

[45] Gray, A. D., Harnett, J. I., & Beck, R. 2002, ASPC, 276, 410

[46] Greisen, E. W., Spekkens, K., & van Moorsel, G. A. 2009, AJ, 137, 4718

[47] Greve, A., Becker, R., Johansson, L. E. B., & McKeith, C. D. 1996, A&A, 312, 391

[48] Grocholski, A. J., Aloisi, A., van der Marel, R. P., Mack, J., Annibali, F., Angeretti, L., Greggio, L., Held, E. V., Romano, D., Sirianni, M., & Tosi, M. 2008, ApJ, 686, L79

[49] Grützbauch, R., Annibali, F., Rampazzo, R., Bressan, A., & Zeilinger, W. W. 2010, in *Proceedings of the JENAM 2010, Symposium 2 "Environment and the Formation of Galaxies: 30 years later", Lisbon, Portugal, 2010*, [arXiv:1011.4852v1]

[50] Gu, Qiusheng, Zhao, Yinghe, Shi, Lei, Peng, Zhixin, & Luo, Xinlian 2006, AJ, 131, 806

[51] Guo, Q., & White, S. D. M. 2009, MNRAS, 396, 39

[52] Herrmann, K., & Ciardullo, R. 2009, ApJ, 705, 1686

[53] Hibbard, J. E. 2000, ASPC, 197, 285

[54] Hibbard, J. E., & Yun, M. S. 1999, AJ, 118, 162

[55] Holwerda, B. W., Pirzkal, N., Cox, T. J., de Blok, W. J. G., Weniger, J., Bouchard, A., Blyth, S.-L., & van der Heyden, K. S. 2011, MNRAS, 416, 2426

[56] Hunter, D. A., & Elmegreen, B. 2004, AJ, 128, 2170

[57] Hunter, D. A., & Elmegreen, B. 2006, ApJS, 162, 49

[58] Hunter, D. A., Hawley, W. N., & Gallagher, J. S., III 1993, AJ, 106, 1797

[59] Hunter, D. A., O'Connell, R. W., Gallagher, J. S., & Smecker-Hane, T. A. 2000, AJ, 120, 2383

[60] Hunter, D. A., Rubin, V. C., Swaters, R. A., Sparke, L. S., & Levine, S. E. 2002, ApJ, 580, 194

[61] Israel, F. P. 1988, A&A, 194, 24

[62] Israel, F. P., & van Driel, W. 1990, A&A, 236, 323

[63] Jewell, P. R., & Prestage, R. M. 2004, SPIE, 5489, 312

[64] Kaisin, S. S., & Karachentsev, I. D. 2008, A&A, 479, 603

[65] Kalirai, J. S., Beaton, R. L., Geha, M. C., Gilbert, K. M., Guhathakurta, P., Kirby, E. N., Majewski, S. R., Ostheimer, J. C., Patterson, R. J., & Wolf, J. 2010, ApJ, 711, 671

[66] Karachentsev, I. D., Sharina, M. E., Dolphin, A. E., Grebel, E. K., Geisler, D., Guhathakurta, P., Hodge, P. W., Karachentsev, V. E., Sarajedini, A., & Seitzer, P. 2002, A&A, 385, 21

[67] Karachentsev, I. D. 2005, AJ, 129, 178

[68] Karachentsev, I. D., Dolphin, A., Tully, R. B., Sharina, M., Makarova, L., Makarov, D.,Karachentseva, V., Sakai, S., Shaya, E. J. 2006, AJ, 131, 1361

[69] Kravtsov, A. V., Klypin, A., & Hoffman, Y. 2002, ApJ, 571, 563

[70] Kravtsov, A. V. 2003, ApJ, 590, L1

[71] Kravtsov, A. V., Berlind, A. A., Wechsler, R. H., Klypin, A. A., Gottlöber, S., Allgood, B., & Primack, J. R. 2004, ApJ, 609, 35

[72] Kravtsov, A. 2010, Advances in Astronomy, Article ID 281913, 1-21

[73] Krumholz, M. R., McKee, C. F., Tumlinson, J. 2009, AJ, 699, 850

[74] Larsen, S. S., Origlia, L., Brodie, J., & Gallagher, J. S. 2008, MNRAS, 383, 263

[75] Leaman, R., Cole, A. A., Venn, K. A., Tolstoy, E., Irwin, M. J., Szeifert, T., Skillman, E. D., & McConnachie, A. W. 2009, ApJ, 699, 1

[76] Leroy, A., Walter, F., Brinks, E., Bigiel, F., de Blok, W. J. G., Madore, B., & Thornley, M. D. 2008, AJ,136, 2782

[77] Lisker, T., Janz, J., Hensler, G., Kim, S., Rey, S.-C., Weinmann, S., Mastropietro, C., Hielscher, O., Paudel, S., & Kotulla, R. 2009, ApJ, 706, L124

[78] Makarova, L., Karachentsev, I., Takalo, L. O., Heinaemaeki, P., & Valtonen, M. 1998, A&ASS, 128, 459

[79] Marigo, P., & Girardi, L. 2007, A&A, 469, 239

[80] Martin, C. L., Kobulnicky, H. A., & Heckman, T. M. 2002, ApJ, 574, 663

[81] Mateo, M. 1998, ARA&A, 36, 435

[82] McQuinn, K. B., Skillman, E. D., Cannon, J. M., Dalcanton, J., Dolphin, A., Hidalgo-Rodríguez, S., Holtzman, J., Stark, D., Weisz, D., & Williams, B. 2010, AJ, 721, 297

[83] Mori, M., Yoshii, Y., Tsujimoto, T., & Nomoto, K. 1997, ApJ, 478, L21

[84] Mühle, S., Klein, U., Wilcots, E. M., & Hüttemeister, S. 2005, AJ, 130, 524

[85] Navarro, J. F., Frenk, C. S., & White, S. D. M. 1995, MNRAS, 275, 720N

[86] Navarro, J. F., Frenk, C. S., & White, S. D. M. 1997, ApJ, 490, 493

[87] Obreschkow, D., & Rawlings, S. 2009, MNRAS, 394, 1857

[88] Oh, S.-H. 2009, PhD Dissertation, The Australian National University

[89] Oh, S.-H., de Blok, W. J. G., Brinks, E., Walter, F., & Kennicutt, R. C., Jr. 2011, AJ, 141, 193

[90] Oh, S.-H., de Blok, W. J. G., Walter, F., Brinks, E., & Kennicutt, R. C. 2008, AJ, 136, 2761

[91] Paudel, S., Lisker, T., & Janz, J. 2010a, ApJ, 724, L64

[92] Paudel, S., Lisker, T., Kuntschner, H., Grebel, E. K., & Glatt, K. 2010b, MNRAS, 405, 800

[93] Pedraz, S., Gorgas, J., Cardiel, N., Sánchez-Blázquez, P., & Guzmán, R. 2002, MNRAS, 332, 59

[94] Pierce, M., Brodie, J. P., Forbes, D. A., Beasley, M. A., Proctor, R., & Strader, J. 2005, MNRAS, 358, 419

[95] Prada, F., Klypin, A. A., Cuesta, A. J., Betancort-Rijo, J. E., & Primack, J. 2011, ArXiv e-prints, 1104.5130

[96] Reakes, M. 1980, MNRAS, 192, 297

[97] Rich, J. W., de Blok, W. J. G., Cornwell, T. J., Brinks, E., Walter, F., Bagetakos, I., & Kennicutt, R. C. 2008, AJ, 136, 2897

[98] Robertson, B., Bullock, J. S., Cox, T. J., Di Matteo, T., Hernquist, L., Springel, V., & Yoshida, N. 2006, ApJ, 645, 986

[99] Robertson, B., Kravtsov, A. V., Gnedin, N. Y., Abel, T., & Rudd, D. H. 2010, MNRAS, 401, 2463

[100] Rots, A. H. 1979, A&A, 80, 255

[101] Rubin, V., & Ford, K. 1970, ApJ, 159, 379R

[102] Rubin, V. C., Thonnard, N., & Ford, W. K., Jr. 1978, ApJ, 225, L107

[103] Rudd, D. H., Zentner, A. R., & Kravtsov, A. V. 2008, ApJ, 672, 19

[104] Sánchez-Janssen, R., Aguerri, J. Alfonso L., & Muñoz-Tuñón, C. 2008, ApJ, 679, 77

[105] Sarajedini, A., Grebel, E. K., Dolphin, A. E., Seitzer, P., Geisler, D., Guhathakurta, P., Hodge, P. W., Karachentsev, I. D., Karachentsev, V. E., & Sharina, M. E. 2002, ApJ, 567, 915

[106] Sawala, T., Scannapieco, C., Maio, U., & White, S. 2010, MNRAS, 402,1599

[107] Sawala, T., Guo, Q., Scannapieco, C., Jenkins, A., & White, S. 2011, MNRAS, 413, 659

[108] Schlegel, D. J., Finkbeiner, D. P., & Davis, M. 1998, ApJ, 500, 525

[109] Schneider, S. E., Thuan, T. X., Mangum, J. G., & Miller, J. 1992, ApJS, 81, 5

[110] Simpson, C., & Gottesman, S. T. 2000, AJ, 120, 2975

[111] Steinmetz, M., & Navarro, J. 2002, New Astronomy, 7, 155

[112] Stil, J. M., & Israel, F. P. 1998, A&A, 337, 64

[113] Stil, J. M., & Israel, F. P. 2002, A&A, 392, 473

[114] Stil, J. M., Gray, A. D., & Harnett, J. I. 2005, ApJ, 625, 130

[115] Swaters, R. A. 1999, Ph. D. Dissertation, University of Groningen

[116] Taylor, C. L., Hüttemeister, S., Klein, U., & Greve, A. 1999, A&A, 349, 424

[117] Tollerud, E. J., Boylan-Kolchin, M., Barton, E. J., Bullock, J. S., & Trinh, C. Q. 2011a, ArXiv e-prints, 1103.1875

[118] Tollerud, E. J., Bullock, J. S., Graves, G. J., & Wolf, J. 2011b, ApJ, 726, 108

[119] Tomita, A., Ohta, K., & Saito, M. 1994, PASJ, 46, 335

[120] Tonnesen, S., & Bryan, G. L. 2010, ApJ, 709, 1203

[121] Tossi, M. 2003, Ap&SS, 284, 651

[122] United States Nautical Almanac Office 2008, Astronomical Almanac (Washington, DC: US Gov. Printing Office)

[123] Vale, A., & Ostriker, J. P. 2004, MNRAS, 353, 189

[124] van der Kruit, P. C., & Searle, L. 1981, A&A, 95, 105

[125] van Eymeren, J., Koribalski, B. S., López-Sánchez, Á., Dettmar, R.-J., & Bomans, D. J. 2010, MNRAS, 407, 113

[126] van Gorkom, J. H., Knapp, G. R., Raimond, E., Faber, S. M., & Gallagher, J. S. 1986, AJ, 91, 791

[127] van Zee, L., Skillman, E. D., & Haynes, M. P. 2004, AJ, 128, 121

[128] Vega Beltrán, J. C. 1999, PhD Dissertation, Universidad de La Laguna, Instituto de Astrofísica de Canarias

[129] Vega Beltrán, J. C., Pizzella, A., Corsini, E. M., Funes, J. G., Zeilinger, W. W., Beckman, J. E., & Bertola, F. 2001, A&A, 374, 394

[130] Walker, M. G., Mateo, M., Olszewski, E. W., Gnedin, O. Y., Wang, X., Sen, B., & Woodroofe, M. 2007, ApJ, 667, L53

[131] Walker, M. G., Mateo, M., Olszewski, E. W., Penarrubia, J., Wyn Evans, N., & Gilmore, G. 2009, ApJ, 704, 1274

[132] Wakker, B., van Woerden, H., de Boer, K. S., & Kalberla, P. 1998, ApJ, 493, 762

[133] Waller, W. H. 1991, ApJ, 370, 144

[134] Walter, F., Brinks, E., de Blok, W. J. G., Bigiel, F., Kennicutt, R. C., & Thornley, M. 2008, AJ, 136, 2563

[135] Welieachew, L., Sancisi, R., & Guélin, M. 1978, A&A, 65, 37

[136] Wilcots, E., & Miller, B. 1998, AJ, 116, 2363

[137] Wilson, C. D., Welch, D. L., Reid, I. N., Saha, A., & Hoessel, J. 1996, AJ, 111, 1106

[138] Young, J. S., Gallagher, J. S., & Hunter, D. A. 1984, ApJ, 276, 476

[139] Zhang, H.-X., Gao, Y., & Kong, X. 2010, MNRAS, 401, 1839

[140] Zhang, H,-X., ... 2011, AJ, submitted

Appendices

– A –

Multi-Scale Cleaning in AIPS

Standard cleaning reproduces structure as the sum of point sources. The final cube is the sum of point sources in the "clean" beam and residuals with the "dirty" beam. Thus, one can produce two cubes: one with correct flux but over-estimated noise, and, one with correct noise but flux that is over-estimated by a factor of 'ϵ' that is the ratio of the dirty beam to the clean beam size, as described in Walter et al. (2008). This ϵ factor creates a pedestal, in a sense, upon which the cleaned flux is imaged, thus over-estimating the true flux.

The multi-scale cleaning algorithm implemented by the LITTLE THINGS team images the data differently by convolving, iteratively, the dirty cube simultaneously to four flux resolution scales (135″, 45″, 15″, and 0″), thereby creating four cubes. This algorithm has the ability to image faint, extended emission because of the smoothed, low resolution convolutions of 135″, 45″, and 15″. These convolved cubes permit detection of peak fluxes that would otherwise be undetectable. The LITTLE THINGS team chose the four resolution scales after careful testing so that the cleaned cubes are robust in imaging tenuous emission while maximizing efficiency. Once the multi-scale imaging process is complete, the final cube contains cleaned images that have both accurate flux and noise, and also possesses extended emission, if any exists. For a comprehensive description of the multi-scale cleaning method and a comparison to the standard cleaning method, see Cornwell (2008), Rich et al. (2008), and Ficut-Vicas et al. (in preparation).

Figure A.1 shows the THINGS integrated flux map of NGC 1569 (*top*), imaged with standard cleaning methods, while the bottom panel shows the LITTLE THINGS integrated flux map imaged with MSCLEAN. It is clear in the top panel of Figure A.1 that the standard cleaning method shows a more "fuzzy" picture of the HI flux, which is due to the pedestal, mentioned above, of the standard cleaning procedure. Also, the bottom panel of Figure A.1 shows tenuous emission to the south and northeast of the galaxy that was imaged for the first time due to the multi-scale cleaning algorithm. Furthermore, the bottom panel shows more concentrated HI clouds than the left panel in the outskirts of the galaxy.

Figure A.2 shows the THINGS intensity-weighted velocity map of NGC 1569, (*top*), and the intensity-weighted velocity map from LITTLE THINGS, (*bottom*). Although both panels show strong non-circular motions across all of the HI disk in NGC 1569, the LITTLE THINGS velocity map has more distinct velocity clouds than the THINGS map. Also, the bottom panel shows the velocities of the tenuous emission to the south and north of the galaxy which match the velocities of the $0^{\circ}.5$ HI cloud detected in the GBT data.

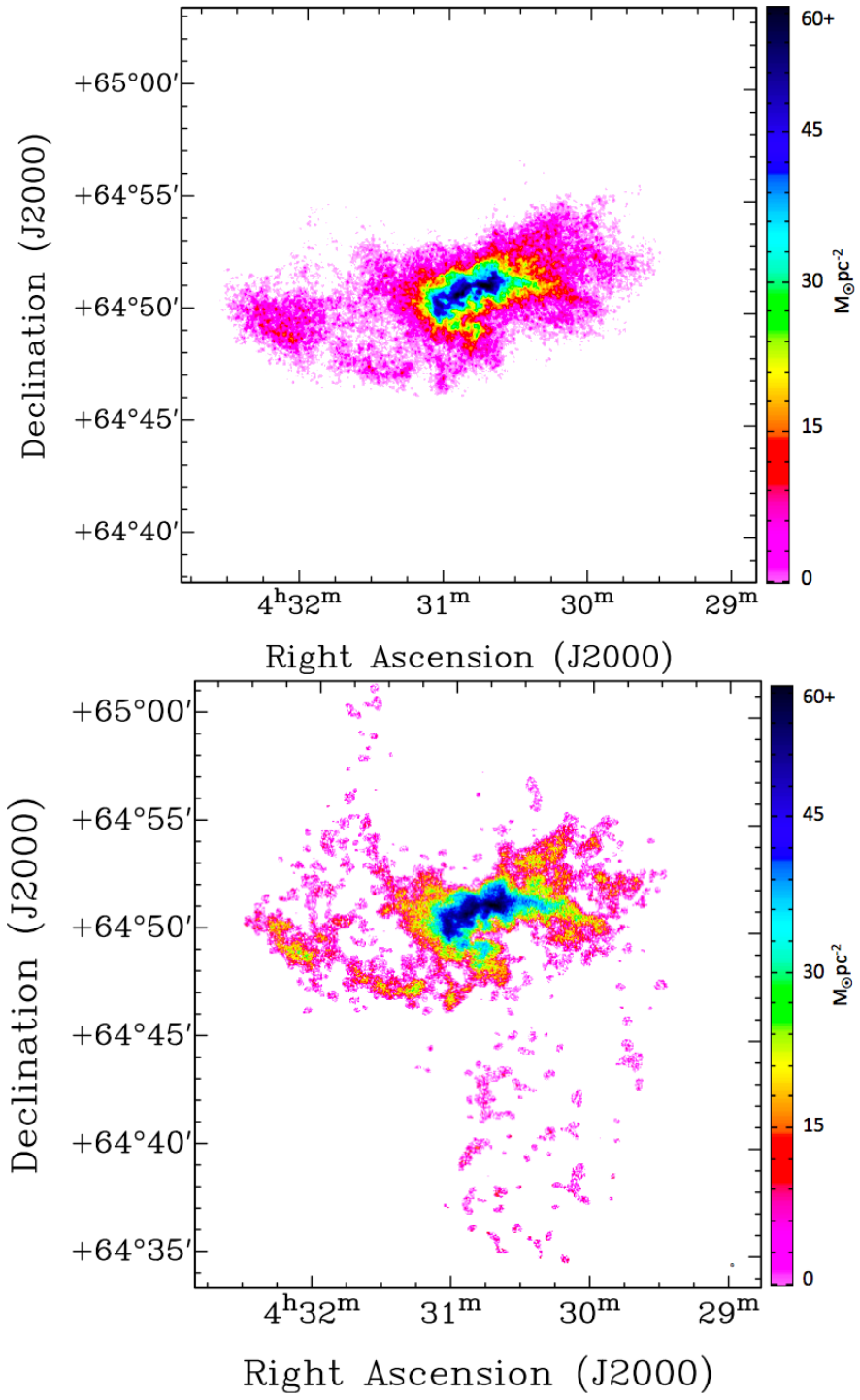

Figure A.1 Top: Integrated HI flux of NGC 1569 from THINGS, imaged with standard cleaning. Bottom: Integrated HI flux of NGC 1569 from LITTLE THINGS, imaged with the multi-scale cleaning algorithm. The MSCLEAN implemented by LITTLE THINGS was able to image tenuous emission to the south and northeast for the first time.

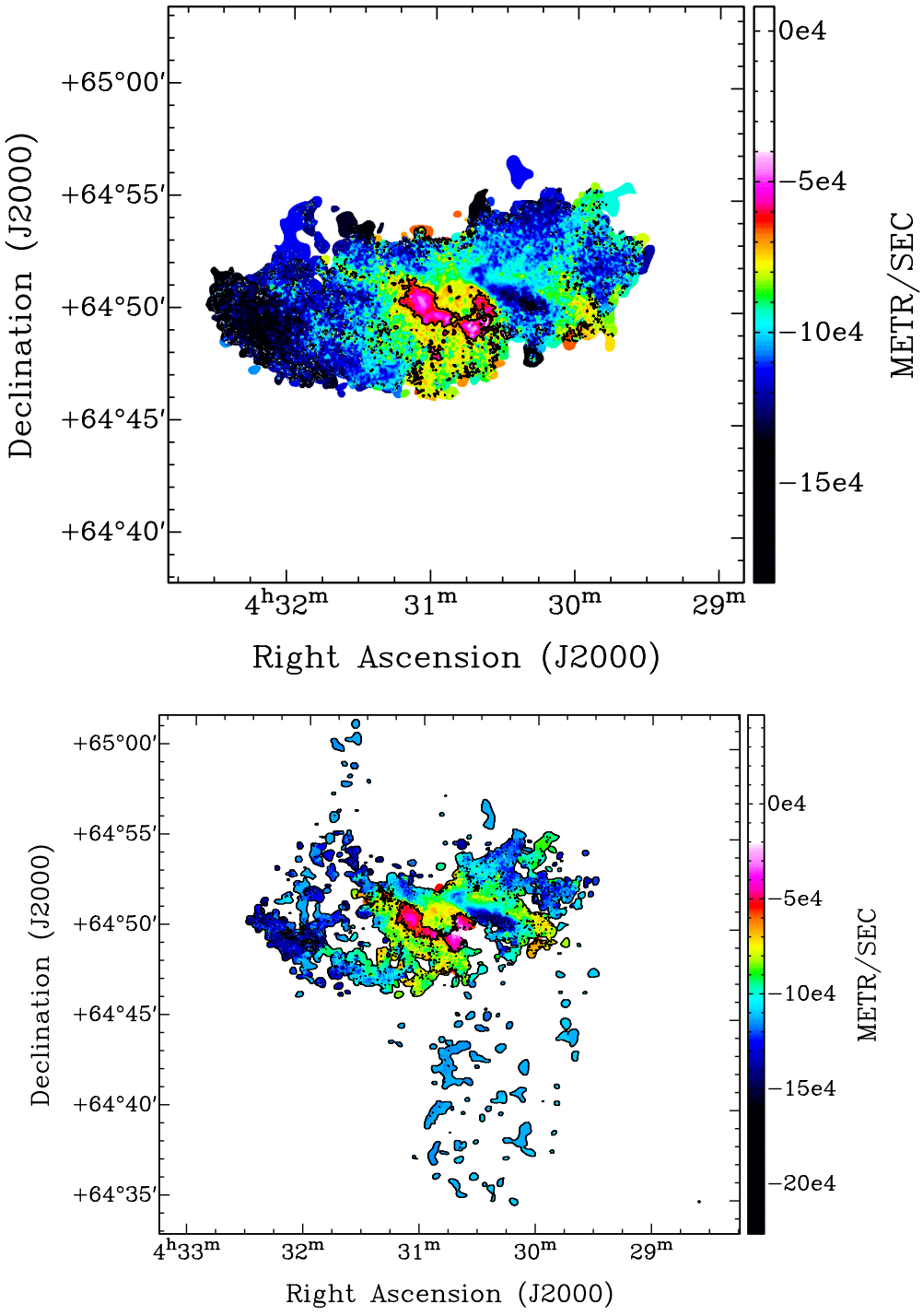

Figure A.2 Top: Intensity weighted velocity field from THINGS. Bottom: Intensity-weighted HI velocity field of NGC 1569.

– B –

HI Flux to Total HI Mass and Mass Surface Density Transformation

B.1 VLA

B.1.1 Total HI Mass

After all data reductions have been completed, the HI data from the VLA are in a three dimensional data cube with position in RA and DEC along the x- and y-axes, respectively, and velocity along the z-axis. In order to create the integrated maps shown in Figures 3.2 and A.1, the intensities at each position in the data cube, which have units of mJy beam^{-1}, are integrated using the AIPS task XMOM over all channels i, which have a velocity separation, $\Delta V = 2.6$ km s^{-1}. The following equation from Walter et al. (2008) is used to create the integrated HI map:

$$I_{HI} = \sum_i S_i \Delta V \tag{B.1}$$

The two dimensional, integrated flux map created by XMOM has units of mJy beam^{-1} km s^{-1}. It is desirable to transform the fluxes in this map into more useful units. In order to obtain the total HI mass of NGC 1569 in units of $M_\odot$, the following steps were taken:

1) The AIPS task ISPEC was used to sum the fluxes in the integrated flux map over a desired rectangle of user defined coordinates. The output produced a total flux, $\sum_i S_i \Delta V$, in units of mJy beam^{-1} km s^{-1} pixel^{-1}.

2) This output was multiplied by a factor of beam pixel^{-1}, which is given by the following equation:

$$\frac{(\Delta x'' \ \Delta y'')/\text{pixel}}{(1.13 \ \Delta\alpha \ \Delta\delta)/\text{beam}} \tag{B.2}$$

where $\Delta x''$ and $\Delta y''$ are the pixel sizes in arcsec for RA and DEC, respectively, and $\Delta\alpha$ and $\Delta\delta$ are the beam sizes in arcsec for RA and DEC, respectively. For the VLA maps, $\Delta x'' = \Delta y'' = 1\farcs5$ and $\Delta\alpha = 7\farcs71$ and $\Delta\delta = 7\farcs04$. Therefore, the total flux produced by ISPEC was multiplied by 0.037 beam pixel^{-1}, and produced $\sum_i S_i \Delta V = 88,800$ mJy km s^{-1}.

3) This sum was then placed into the following equation from Walter et al. (2008), which produces the total HI mass, $M_{\rm HI}$, in units of $M_\odot$:

$$M_{\rm HI} = 235.6\ D^2\ \sum_i S_i \Delta V \tag{B.3}$$

Here, D is the distance in Mpc and $\sum_i S_i \Delta V$ is the amount given in step 2 above. The total HI mass for NGC 1569 determined from the VLA data is, thus, 2.3 x 10^8 $M_\odot$.

B.1.2 HI Column Density and Mass Surface Density

It is also useful to determine the column density, $N_{\rm HI}$ (units = atoms cm^{-2}), which can then be used to determine the mass surface density as a function of radius. Again, the two dimensional, integrated flux map is used and the following steps were taken to derive the average column density in NGC 1569:

1) The total flux from ISPEC from Step 1 in the previous section (Section B.1.1), can be used in the following equation to derive the total brightness temperature, $\sum_i T_{B,i}\ \Delta V$ in units of K km s^{-1}:

$$\sum_i T_{B,i}\ \Delta V = \frac{\sum_i S_i \Delta V}{1.65 \text{ x } 10^{-3}\ \Delta\alpha\Delta\delta} \tag{B.4}$$

where $\Delta\alpha$ and $\Delta\delta$ are the beam sizes in arcsec for RA and DEC, respectively. The subscript i is included here because the integrated map is the flux that has been summed over all velocity channels, i. ΔV is equal to 2.6 km s^{-1}, which is the velocity resolution. This equation is from private communications with Elias Brinks and produced a total brightness temperature, $\sum_i T_{B,i}\ \Delta V = 2.7$ x 10^7 K km s^{-1}.

2) To determine an average column density, the brightness temperature, $\sum_i T_{B,i}\ \Delta V$, must be divided by the total number of pixels that contained emission and were used in the summation. Then, the following equation from Walter et al. (2008) can be used to derive $N_{\rm HI}$ in units of atoms cm^{-2}:

$$N_{\rm HI} = 1.823\ \text{x}10^{18}\ \frac{\sum_i T_{B,i}\ \Delta V}{\#\ \text{pixels}} \tag{B.5}$$

For NGC 1569, the average column density over the entire galaxy was 2.8 x 10^{19} cm^{-2}.

3) $N_{\rm HI}$ can be converted to units of M$_\odot$ pc^{-2} following this relationship:

$$1\ \text{M}_\odot\ \text{pc}^{-2} = 1.248\ \text{x}\ 10^{20}\ \text{atom cm}^{-2} \tag{B.6}$$

To derive the mass surface density scale shown in Figures 3.2 and A.1, the color greyscale, which had units of mJy beam^{-1} km s^{-1} when it was created, was converted to M$_\odot$ pc^{-2} following steps 1, 2 and 3 above.

B.2 GBT HI Column Density and Mass

AIPS was also used to determine the masses and column densities for the objects in the GBT map. The task ISPEC was implemented, again, to integrate over the areas outlining the features and galaxies. However, for the GBT data, the entire data cube

in units of K beam^{-1} was used as input for ISPEC, thus, the integration occurred in three dimensions, i.e., position in RA and DEC, and velocity. The output from ISPEC produced a sum of the flux over channels i, $\sum_i T^{\star}_{\mathrm{a,i}}$, in units of K beam^{-1} pixel^{-1}. These data then had to be multiplied by a factor of beam pixel^{-1} using equation B.2 in order to obtain the total antenna temperature, $\sum T^{\star}_{\mathrm{a}}$. For the GBT data, the beam pixel^{-1} factor is 210/527.

Once the total antenna temperature was obtained, the following equation was used to determine the column density in units of atoms cm^{-2}:

$$N_{\mathrm{HI}} = 1.823 \text{ x } 10^{18} \ \frac{\sum T^{\star}_{a} \ \Delta V}{\eta} \tag{B.7}$$

where $\eta = 0.937$ is the telescope efficiency and $\Delta V = 0.805$ km s^{-1} is the channel separation. The average column densities for each object identified in the GBT map were determined. Then, the average column densities, N_{HI} in units of atoms cm^{-2}, were used to derive the masses of the various galaxies and features using this equation:

$$M/M_{\odot} = 6.795 \text{ x } 10^{-16} * N_{\mathrm{HI}} * D * A \tag{B.8}$$

where D is the distance in Mpc and A is the area of the object in arcmin^2. Table 6.2 summarizes the HI column densities and masses of the selected galaxies and features in the GBT map.

– C –

Bulk Motion Extraction from MSCLEAN Cube

There are three inputs required for the bulk motion extraction program: a model velocity field, a single Gaussian fit to the raw LITTLE THINGS HI data cube, and the raw LITTLE THINGS HI data cube itself. Therefore, in order to apply this double Gaussian decomposition technique, the model velocity field must first be created. This is done using the intensity weighted velocity map, Figure 3.3. The Groningen Image Processing SYstem (GIPSY) task ROTCUR is used. This task employs the tilted ring model as described by Begeman (1989). The radial velocity at a given sky position, $V(x, y)$, is described by the following equation:

$$V(x, y) = V_{\rm sys} + V_{\rm rot}(R)\ \sin(i)\ \cos(\theta). \tag{C.1}$$

Here, $V_{\rm sys}$ represents the systemic velocity, i is the inclination of the disk, θ is the azimuthal angle in the plane of the galaxy, and $V_{\rm rot}$ is the circular rotational velocity at radius R (Begeman 1989). The angle θ is related to the inclination (i), PA of the major axis (PA), and kinematic center of the galaxy ($X_{\rm pos}, Y_{\rm pos}$) by the following two equations (Begeman 1989):

$$\cos(\theta) = \frac{-(x - X_{pos})\ \sin(PA) + (y - Y_{pos})\ \cos(PA)}{R} \tag{C.2a}$$

and

$$\sin(\theta) = \frac{-(x - X_{pos})\ \cos(PA) - (y - Y_{pos})\ \sin(PA)}{R\ \cos(i)}. \tag{C.2b}$$

The ROTCUR task is used to find circular velocities, $V_{\rm rot}$, for predetermined radii. In the case of NGC 1569, an initial ring radius of 8″ is used, which is roughly equal to one beam width, and a distance between rings, as measured along the major axis in the plane of the sky, of 8″. The final ring radius to 200″ is set since beyond this radius the signal-to-noise of the HI in the galaxy drops off drastically.

To begin the fitting procedure, the program is run by fixing only the parameter X_{pos}, using the morphological center information from the V-band image shown in Figure 2.1 as a first approximation, and let the other parameters vary freely. After this initial run, the weighted average of Y_{pos} is calculated and fixed for a second run. ROTCUR is run several more times allowing only one parameter to vary at a time, while always keeping $V_{\rm rot}$ a free parameter. This enables us to hone in on convergent values for $X_{\rm pos}$, $Y_{\rm pos}$, $V_{\rm sys}$, i, and PA. Once all five of these parameters converge, the initial rotation curve from the $V_{\rm rot}$ values for the model velocity field is obtained. The results are recorded and put into the GIPSY task VELFI. This task creates the model velocity field that will be used in the bulk motion extraction program. Figure C.1 shows the model velocity field derived from VELFI.

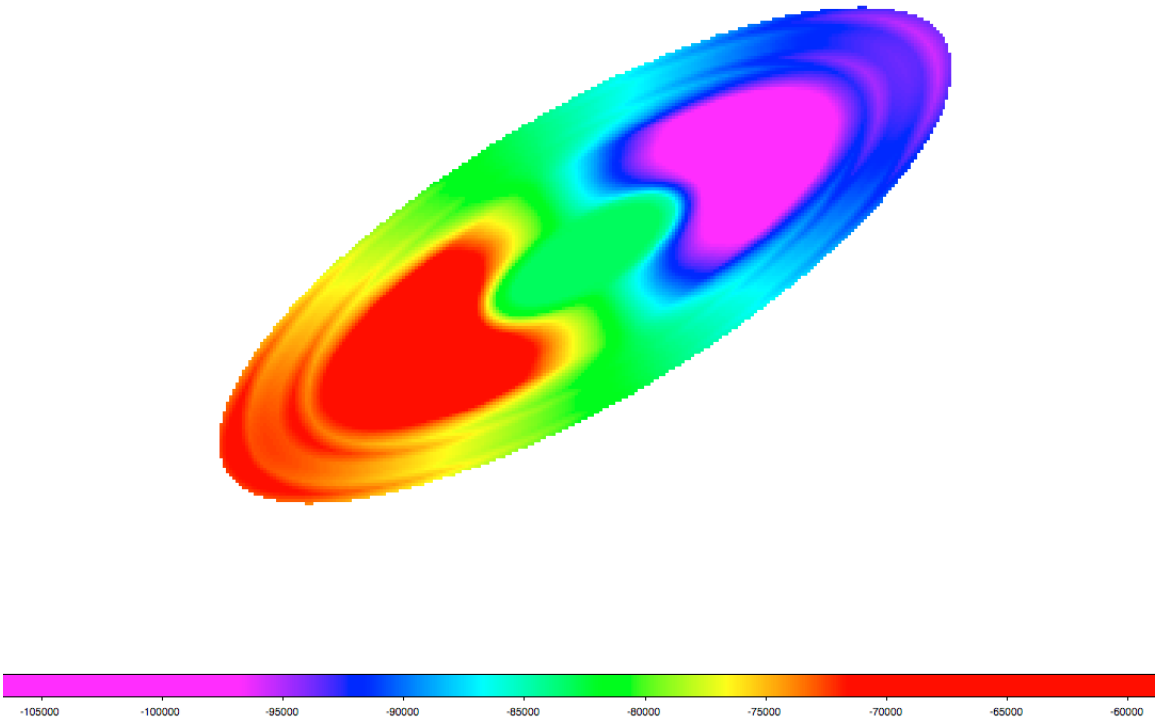

Figure C.1 Model velocity field from GIPSY task 'VELFI' for NGC 1569. The color bar at the bottom of the image shows the velocities in m s^{-1}. This is the model velocity field used in the double Gaussian decomposition procedure.

The second input, a single Gaussian fit to the raw LITTLE THINGS HI data cube, was determined using the GIPSY task 'GAUFIT'. This task takes the HI data cube and fits a single Gaussian distribution function to each spatial point in the cube. The only inputs needed for this fitting procedure are the HI data cube and the RMS noise of the cube.

Now, all three inputs are put into the bulk extraction procedure and the program produces a bulk velocity map, a strong non-circular velocity map, and a weak non-circular velocity map by the method described above. The entire procedure is repeated using the new bulk motion velocity field until the solution converges.